THE SPECTRAL MODEL OF GRAIN BOUNDARY SOLUTE SEGREGATION

BY

MALIK MAMOON ABDELHALIM WAGIH

B.Sc. Mechanical Engineering
The British University in Egypt, 2013

S.M. Nuclear Science and Engineering
Massachusetts Institute of Technology, 2018

SUBMITTED TO THE DEPARTMENT OF NUCLEAR SCIENCE AND ENGINEERING
IN PARTIAL FULFILMENT OF THE REQUIREMENTS FOR THE DEGREE OF

DOCTOR OF PHILOSOPHY IN NUCLEAR SCIENCE AND ENGINEERING

AT THE
MASSACHUSETTS INSTITUTE OF TECHNOLOGY

SEPTEMBER 2021

Author_____

Malik M. Wagih
Department of Nuclear Science and Engineering
August 17, 2021

Certified by_____

Christopher A. Schuh
Danae and Vasilis Salapatas Professor of Metallurgy
Thesis Supervisor

Certified by_____

Ju Li
Battelle Energy Alliance Professor of Nuclear Science and Engineering
Professor of Materials Science and Engineering
Thesis Reader

Accepted by_____

Ju Li
Battelle Energy Alliance Professor of Nuclear Science and Engineering
Professor of Materials Science and Engineering
Chair, Department Committee on Graduate Theses

THE SPECTRAL MODEL OF GRAIN BOUNDARY SOLUTE SEGREGATION

BY

MALIK M. WAGIH

Submitted to the Department of Nuclear Science and Engineering
on August 17, 2021, in partial fulfillment of the requirements for the degree of
Doctor of Philosophy in Nuclear Science and Engineering

ABSTRACT

The segregation of solute atoms at grain boundaries (GBs) can profoundly impact the structural properties of metallic alloys, and induce effects that range from strengthening to embrittlement. And, as such, the control of solute segregation is emerging as an alloy design tool, uses of which include the stabilization of nanocrystalline alloys. To date, the standard approach to predict the extent of solute segregation at GBs uses a simplified representation that treats the GB network as a single entity, and thus, uses a single "average" segregation energy to characterize solute GB segregation in an alloy. This simplification, however, fails to capture the highly disordered and anisotropic nature of GBs in polycrystals, which results in a spectrum of solute segregation tendencies (energies). In this thesis, we aim to address and remove this simplification; the thesis has five major contributions. First, we elucidate computationally the nature of this spectrum for an Mg solute in an Al polycrystal; the distribution is found to be captured accurately with a skew-normal function. Second, we outline a thermodynamic segregation isotherm that incorporates this spectrum, and employ it to study the effect of such a spectrum on predictions of the equilibrium GB segregation state. Third, we develop a machine learning framework that can accurately predict the segregation tendency of solute atoms at GB sites in polycrystals, based solely on the undecorated (pre-segregation) local atomic environment of such sites. We proceed to use the learning framework to scan across the alloy space, and build an extensive database of segregation energy spectra for more than 250 metal-based binary alloys. Fourth, we outline more formally correct thermodynamic criteria to screen for thermodynamic stability of polycrystalline structures,

accounting for the spectral nature of GBs. And, we proceed to apply the developed criteria to screen over 200 alloy combinations. Among its benefits, this spectral approach enables strict enforcement of the third law of thermodynamics, where an average segregation energy does not. Fifth, we take the first step to extend the developed framework to handle solute segregation beyond the dilute limit, by outlining a thermodynamic segregation isotherm that accounts for both the spectrality of grain boundary sites, and solute-solute interactions; we also develop a computational framework to extract, and delineate both effects. Finally, we hope that the developed spectral thermodynamic framework, machine learning models, and solute segregation database in this thesis would help unlock the full potential of GB segregation as an alloy design tool, and enable the design of microstructures that maximize the useful impacts of segregation.

Thesis Supervisor: Christopher A. Schuh

Title: Danae and Vasilis Salapatas Professor of Metallurgy

Thesis Reader: Ju Li

Title: Battelle Energy Alliance Professor of Nuclear Science and Engineering

Professor of Materials Science and Engineering

ACKNOWLEDGEMENTS

First, I would like to thank my advisor Prof. Christopher Schuh for his unlimited support and guidance throughout this thesis. Prof. Schuh had an indescribable impact on my development as a scientist. I have benefited immensely from his mentorship, and will be forever indebted to him. Thank you.

I would also like to thank the thesis and defense committee members for their time, insightful feedback, and support: Prof. Ju Li, Prof. Boris Kozinsky, Prof. Koroush Shirvan, and Prof. Mingda Li. I am particularly grateful to Prof. Ju Li for being my thesis reader.

Many thanks to all the Schuh group members, from whom I learned a lot across the years. Special thanks go to Arvind Kalidindi, and Peter M. Larsen for their guidance when I started on this project, and to Yannick Naunheim, Nutth Tuchinda, and Thomas Matson for the lively science discussions over the last two years.

My time here in Boston has been enjoyable because of all the great friendships: (in alphabetical order) Artyom Kossolapov, Aya Amer, Karim Raafat, Mahmoud Ayman, Mohamed Radwan, Mostafa Bedewy, Mostafa Ordu, Mostafa Youssef, Omar AbouZid, Sally Elhenawy, Samuel McAlpine, Stephen Lam, and Tudor Padurariu. Also, many thanks to my friends from Egypt for their constant support: (in alphabetical order) Khaled Hussein, Mohamed Ezz, Mohamed Gamal, Mohamed Helal, Mohamed Refat, and Omar Zayed. A special thank you goes to my undergraduate advisor Prof. Tarek Hatem for his support and friendship.

I would also like to thank all the students, faculty, and administrative staff of NSE. All my interactions over the years were only positive. Special thanks go to Brandy Baker, and Marina Dang for their support.

Finally, I would like to thank my family for their never-ending love and support throughout the years: my siblings, Malak, Safinaz, and Samaa, and Anas, and my parents, Golostan and Mamoon, to whom I dedicate this work. And, last but not least, my wife Amira, whom meeting and marrying will always remain my best accomplishment at MIT. Thank you all for everything.

CONTENT

1. INTRODUCTION 14
   1.1. Research Objectives and Outline of Thesis 17
2. SPECTRUM OF GRAIN BOUNDARY SEGREGATION ENERGIES IN A POLYCRYSTAL 20
   2.1. Thermodynamic model for GB segregation with multiple site-types 20
   2.2. Simulation Methodology 22
   2.3. The spectrum of segregation energies 25
      2.3.1. Properties of the spectrum 25
      2.3.2. Approximations of the spectrum 30
      2.3.3. Comparison with McLean-type models 32
      2.3.4. Implications for experimental results 33
   2.4. Conclusion 34
3. LEARNING GRAIN BOUNDARY SEGREGATION ENERGY SPECTRA IN POLYCRYSTALS 36
   3.1. High-Fidelity ML model for GB Segregation 37
   3.2. Accelerated ML Model for GB segregation 42
   3.3. Spectral Segregation Database 45
   3.4. Computational Methods 49
      3.4.1. GB segregation enthalpies 49
      3.4.2. Machine Learning 50
      3.4.3. Data and Code Availability 50
   3.5. Conclusion 51
4. THERMODYNAMICS AND DESIGN OF NANOCRYSTALLINE ALLOYS USING GRAIN BOUNDARY SEGREGATION SPECTRA 52
   4.1. Spectral Enthalpic Stability Criteria for Nanocrystalline Alloys 53
      4.1.1. Stability of a polycrystal with respect to a solid solution 53
      4.1.2. Stability of a polycrystal with respect to competing ground state phases 55
      4.1.3. Functional form of the grain boundary segregation energy 58
   4.2. Atomistic Computational Methods 58
   4.3. Nanocrystalline alloys vs. enthalpic ground states 62
   4.4. Screening nanocrystalline alloys stable against solid solution formation 65
   4.5. Spectral Improvements over the Classic “Averaged” Approach to Nanocrystalline Stability 68
   4.6. Conclusion 71
5. GRAIN BOUNDARY SEGREGATION BEYOND THE DILUTE LIMIT 73

5.1. Thermodynamics of grain boundary segregation 74
5.1.1. The classical “average” approach 74
5.1.2. The spectral approach 75
5.1.3. Finite Grain Sizes 76
5.1.4. Interpretation of Energies 78
5.2. Atomistic Computational Methods 78
5.2.1. The Spectrum of Segregation Energies 79
5.2.2. GB Segregation States 80
5.3. Contributions of Site Spectrality and Solute-Solute Interactions 83
5.3.1. Site Spectrality 84
5.3.2. Solute-Solute Interactions 85
5.4. Limitations of the Classical Approach are Remedied by the Spectral Approach 86
5.5. Nonlinearity of Solute-Solute Interactions 89
5.6. Conclusion 93
6. FUTURE WORK DIRECTIONS 94
APPENDIX A : SPECTRAL SEGREGATION DATABASE 97
A.1. Segregation Spectra 97
A.1.1. Ag-based alloys 98
A.1.2. Al-based alloys 99
A.1.3. Au-based alloys 100
A.1.4. Co-based alloys 101
A.1.5. Cr-based alloys 102
A.1.6. Cu-based alloys 103
A.1.7. Fe-based alloys 104
A.1.8. Mg-based alloys 105
A.1.9. Mo-based alloys 106
A.1.10. Nb-based alloys 107
A.1.11. Ni-based alloys 108
A.1.12. Pd-based alloys 109
A.1.13. Pt-based alloys 110
A.1.14. Re-based alloys 111
A.1.15. Ta-based alloys 112
A.1.16. Ti-based alloys 113
A.1.17. V-based alloys 114
A.1.18. W-based alloys 115
A.1.19. Zr-based alloys 116

A.2. Segregation Data Analysis 117
A.3. Identifiers for Interatomic Potentials 119
APPENDIX B : DERIVATION OF NANOCRYSTALLINE ENTHALPIC STABILITY CRITERIA 122
B.1. Enthalpies for different alloy states 122
B.1.1. Phase-separated state 122
B.1.2. Solid solution 122
B.1.3. Ordered compound 123
B.1.4. Nanocrystalline grain boundary solute-segregated state 123
B.2. Spectral Enthalpic Stability Criteria for Nanocrystalline Alloys 124
B.2.1. Stability against solid solutions 124
B.2.2. Stability against phase separation 125
B.2.3. Stability against compound formation 126
REFERENCES 128

LIST OF FIGURES

Figure 1: An illustration of the "averaged" McLean's approach to GB solute segregation. In this treatment, a solute atom can only occupy two site-types (or local atomic environments), the bulk and the GB. And thus, this simplification ignores the variety of site-types that should exist at the GB, as a result of its disordered nature. 15

Figure 2: An illustration of experimentally observed variation of solute segregation across the GB space in polycrystals. (a-d) Scanning transmission electron microscopy and energy-dispersive x-ray spectroscopy mapping of Au solute segregation in Pt thin films [45]. Panels (a-d) adapted with permission from reference [45]; copyright 2019 Elsevier. 16

Figure 3: The proposed spectral framework to treat GB solute segregation in polycrystals. In contrast to the "averaged" approach outlined in Figure 1, this treatment incorporates the spectrum of local atomic environments, or site-types at the GB network. 17

Figure 4: The thermally annealed $(36\ \text{nm})^3$ aluminum polycrystal; (a) 72 distinct grains and (b) 414,538 GB atoms used for computing the distribution of segregation energies in the polycrystal. 24

Figure 5: Disorientation distribution of the 488 GBs in the annealed $(36\ \text{nm})^3$ Al polycrystal, represented in sections of constant misorientation angle where each section is the standard stereographic triangle of the 432 cubic group [76]; points that apparently lie outside the fundamental zone arise due to the binning in disorientation angle amongst sections. 24

Figure 6: The distribution of 414,538 GB dilute -limit segregation energies for an Mg solute in a $(36\ \text{nm})^3$ polycrystalline Al sample. 26

Figure 7: Plot of all favorable GB segregation sites in the polycrystal from -75 to 0 kJ/mol divided over three equal intervals. The most favorable sites are well spread over the GB network with no apparent clustering at a single GB. 27

Figure 8: Two-point correlation function for five intervals (percentile of the spectrum) of the most favorable segregation sites. $\xi(x)$ approaches zero around 3 nm, which signifies that, at this separation distance, the spread of favorable sites over the GB network is indistinguishable from a random one. 27

Figure 9: The cumulative fraction of segregation energies for the four different polycrystalline samples listed in Table 1, and the residual (ε) of the three smaller samples against the reference $(36\ \text{nm})^3$ sample. 29

Figure 10: (a) The equilibrium segregation state in the $(36\ \text{nm})^3$ Al polycrystal with a solute addition of $X_{Mg}^{tot} = 5\%$ at T = 300, 500, 700 K. The discrete model Eq. (9), skew-normal model Eq. (17) and the Monte Carlo simulation at T=700 K, are given by the solid lines, dashed lines, and hatched area, respectively; predictions of all three methods match closely. (b)(c) Equilibrium X^{gb} and ΔE_{seg}^{eff} as a function of X_{Mg}^{tot} and T, using the full discrete spectrum and best-fit skew-normal approximation. 30

Figure 11: Comparison of X^{gb} predictions of the thermodynamic model using the full spectrum and approximated distributions versus using a single averaged ΔE_{seg}^{eff} in Mclean's model. 32

Figure 12: Fitting a normal distribution of segregation energies to experimental measurements of X^{gb} versus X^{c} for the Ni-W system, which are obtained from Detor et al. [81]: (a) predicted distribution of segregated solute atoms at $X^{c} = 9.9\%$ and (b) predicted X^{gb} as a function X^{c}. . 34

Figure 13: High-fidelity ML model to learn Mg solute [67] segregation at GBs in an Al polycrystal. For the (a) 20x20x20 nm^3 thermally annealed Al polycrystal with 16 grains (colored by the centro-symmetry parameter [92]), (b) the LAE of every identified GB atom is transformed into a feature vector, using the SOAP method [91] with r_{cutoff}=6Å, to construct a feature matrix for the full GB network (N^{GB} atoms x F^{SOAP} features), which is used as the input to the (c) learning algorithm (linear regression) to learn Mg GB segregation energies, using a 50/50 training/testing split. (d) predictive performance – mean absolute error (MAE) – of the trained ML model across the full GB network. 38

Figure 14: The mean absolute error of the high-fidelity model for the Al(Mg) system as a function of number of training datapoints per SOAP features (N x F^{SOAP}). The shaded region is the standard deviation for 50 repetitions of the 50/50 train/test holdout method used to train the high-fidelity model. The plot validates the 10 points per predictor rule of thumb, as it shows the learning model to converge to a low variance and low bias model with 10xF^{SOAP} datapoints. 39

Figure 15: Validation of the high-fidelity ML framework across the alloy space. The predictive performance – mean absolute error (MAE) –of trained ML models, as outlined in Figure 13, for solute segregation in six 20x20x20 nm^3 polycrystalline alloys: a-f Ag(Ni) [98], Cu(Zr) [99], Fe(Al) [100], Ni(Cu) [101], Pt(Au) [49], and Zr(Ni) [102]. 40

Figure 16: Accelerated ML model for GB segregation. For the Al(Mg) alloy, shown in Figure 13, (a) Principal component analysis is used to reduce the dimensionality of the feature matrix by projecting the F^{SOAP} features into P=10 components that capture >99% of the variance. (b) *k*-means clustering is then used to divide the 10-d transformed feature space into Px10=100 similar clusters; the closest GB sites to the cluster centers (shortest Euclidean distance) are used as training data-points for the learning algorithm (linear regression). (c) Predictive performance – mean absolute error (MAE) – of the accelerated model across the full Al GB network. 42

Figure 17: An overview of the accelerated model, outlined in Figure 16, for the Al(Mg) alloy. (a) *k*-means centers plotted over a density-plot of the GB population in PCA space, and (b) a hexbin plot of the MAE across the PCA space. 44

Figure 18: GB segregation spectra in Ni-based alloys. Using the accelerated ML model outlined in Figure 16, we compute GB segregation energy spectra for 18 solutes [98,101,102,111–119] in a 20x20x20 nm^3 Ni polycrystal of grain size 10 nm; the anti-segregation region ($\Delta E_i^{seg} > 0$) is shaded. The spectra are fitted to the skew-normal function Eq. (19)(solid line), and the value of the characteristic energy μ (kJ/mol), width σ (kJ/mol), and shape α of the function are listed. Also, the spectra are compared to the "average" segregation energy (dashed vertical line) used to charecterize these alloys in the database of Murdoch and Schuh [120]. 45

Figure 19: Predictions of the equilibrium segregation state. Predictions of equilibrium X^{gb} using the true, and predicted (from both high-fidelity and accelerated ML models) segregation spectra for seven polycrystalline alloys with an average grain size of 15nm at T= 600 K. 48

Figure 20: Visual summary of the predicted segregation tendency across the alloy space. The value of the first quartile of the segregation spectra (i.e. 25% of GB sites have lower segregation energies) as predicted using the accelerated model for 225 alloys (we removed columns with empty entries for compact viewing); the elements are arranged by their order on the Pettifor chemical scale [124]. For alloys with multiple interatomic potentials (see Supplementary Fig. 1), we report the least segregating spectra as a conservative choice (see Supplementary Fig. 25 for an alternative version of the figure with the most segregating spectra). 49

Figure 21: An illustration of the effect of changing the reference state for the solute (i.e. in a solid solution versus the ground state at T=0K) on the (calculated) energetics of solute segregation at GBs, and subsequently, the enthalpic favorability for the different GB site-types. 57

Figure 22: (a) The ground state stability score Φ^S and (b) metastability score Φ^M for the surveyed 210 alloys. Entries marked with (X) in (a) are for alloys, where the available interatomic potential gives an incorrect value of $\Delta E^{solute}_{ref=sln} > 0$ in Eq. (32). 61

Figure 23: An illustration of the two-stage procedure developed in Ref [146] to show the impact of solute interactions on the equilibrium segregation state for Ni solutes in a Pt polycrystal [114], for a total solute concertation, $X^{tot} = 10\%$, and T=300 K. The repulsive solute interactions at the GB reduce the solute concentration at the GB from $X^{gb} = 48\%$ to 27%. The shaded red and blue regions show the occupied GB sites (by solute atoms) before, and after taking into account solute interactions, respectively..... 64

Figure 24: The metastability scores for alloys in Table 3 versus the maximum experimentally observed homologous temperature (calculated relative to the alloy solidus) for nanocrystalline stability. We highlight three pairs of alloys (of the same base metal) where a higher metastability score translates into observed nanocrystalline stability at higher temperatures. 67

Figure 25: A comparison of the "averaged" metastability score Φ^M_{avg}, Eq. (37) with the spectral Φ^M, Eq. (28). 69

Figure 26: A comparison of the (a) "averaged" and (b) spectral approach to screening Fe(Mg) for nanocrystalline stability. As the "averaged" approach assumes a dilute value for ΔE^{seg} for the whole GB network, the classic stability map in (a) predicts the system to be stable. However, by examining the spectrum of segregation energies (probability density function (PDF)) in (b), we realize that only a small fraction of GB sites has comparable (favorable) segregation energies to ΔE^{seg} (green shaded area bounded by Φ^S), which is not enough to stabilize the whole GB network. Instead, the spectral approach predicts the system to be metastable, as a large fraction of GB sites (yellow shaded region in (b)) is accessible to Φ^M. 71

Figure 27: (a) The thermally annealed 15x15x15 nm^3 Al polycrystal with 8-grains of an average size of 8 nm; the 37,515 GB sites are only shown after deleting all FCC atoms identified using the adaptive common neighbor analysis method. (b) the calculated distribution of dilute-limit segregation energies of an Mg solute at all GB sites, and a best-fit of the skew-normal function, Eq. (19), with $\alpha = -1.1$, $\mu = 4$ kJ/mol, $\sigma = 19$ kJ/mol. 80

Figure 28: (a) We obtain the equilibrium segregation state for $X^{tot} = 10\%$ in two stages: First, we run an MC simulation using dilute-limit segregation energies (no-interactions); this state (shaded in red) matches the predictions of the spectral model (red dashed line, Eq. (51)) with no interactions ($\omega = 0$). Second, we run hybrid MC/MS for 1000 swaps/solute atoms (a total of

$\sim 2 \times 10^7$ swap attempts for $X^{tot} = 10\%$) to correct for solute-solute interactions, and obtain the final equilibrium segregation state (shaded in blue). The equilibrated structures for both stages are shown in (b) and (c), respectively, with solute atoms colored..... 81

Figure 29: Comparison of the predictions of the McLean (Eq. (48), $\Delta E^{seg} = -29\ kJ/mol$), Fowler-Guggenheim (Eq. (50) $\Delta E^{seg} = -29$, $\omega = 99$ kJ/mol), spectral without interactions (Eq. (51) with $\omega = 0$) and spectral with interactions (Eq. (53) with $\omega = 37$ kJ/mol) models against MC/MS simulations at 450K; the contribution of spectrality to the concentration dependence of segregation is of a comparable magnitude to solute-solute interactions..... 85

Figure 30: The predicted equilibrium segregation state, obtained using the spectral-with-interactions (Eq. (53), $\omega = 37$ kJ/mol) model, and the true state from hybrid MC/MS simulations for $X^{tot} = 2$, 4, and 10%, at 450K. 86

Figure 31: The predictions of the spectral model ($\omega = 37$ kJ/mol) against MC/MS simulations at three different temperatures (300, 450, and 600 K); the shaded areas are the upper and lower bound of the Fowler-Guggenheim model, Eq. (50), using the three sets of best-fit parameters in Table 4, obtained by fitting each temperature independently. 88

Figure 32: The maximum error in predictions of X^{gb} of the spectral and classic approaches with/without interaction, as compared to MC/MS simulations at 300, 450, and 600 K. For the classical approach (McLean and Fowler-Guggenheim), the plotted error is the maximum error using the three different sets of best-fit (ΔE^{seg} and ω) listed in Table 4. The spectral model parameters are the same for any temperature: (α=-1.1, μ=-4 kJ/mol, σ=19 kJ/mol) for the distribution, ω = 37 kJ/mol for linear interactions. The Spectral (piecewise linear) is discussed in section 5.5. 89

Figure 33: We fit Eq. (53) to hybrid MC/MS simulations of each X^{tot} independently, and obtain the magnitude of interaction energy required for the spectral model to have an absolute error of 1% in X^{gb}; the piecewise linear function (solid line), Eq. (57), is fitted to all data points, with ω=62 kJ/mol, and X_0=10%. 90

Figure 34: (a) The distribution of the distance to first nearest neighbors for solute atoms segregated at the GB for $X^{tot} = 1\%$ ($X^{gb} = 5\%$) at 450K, compared to a random solute distribution with the same X^{gb}. (b) The average distance to N^{th} nearest neighbors for the same sample; beyond ~5 Å, the Mg-Mg interactions are negligible for the embedded atom potential [67]. 92

LIST OF TABLES

Table 1: Comparison of three smaller polycrystalline samples with the $(36nm)^3$ Al polycrystal; ΔE_{seg}^{eff} is for X_{Mg}^{tot}=1% at T = 300K. 28

Table 2: Predictive performance of the high-fidelity model using a) 50/50 training/testing split and b) 5-fold cross validation. The reported errors for the two methods are comparable, which indicates that a simple 50/50 split is sufficient for the model. Also, the low standard deviation (stdv) of error across the 5 folds shows the ability of high-fidelity model to extrapolate well across the GB population. 41

Table 3: Calculated Φ^S and Φ^M scores, and the maximum homologous temperature (relative to the alloy solidus) for stability for several alloys with experimentally observed nanocrystalline stability/metastability. 66

Table 4: Best-fit parameters for the Fowler-Guggenheim model. For each temperature, we fit Eq. (50) to MC/MS simulations to obtain representative ΔE^{seg} and ω. 87

1. INTRODUCTION

In polycrystalline metal alloys, solute segregation often occurs at grain boundaries (GBs), where the disorder in the local atomic environment provides solute atoms with an array of favorable sites over the host solvent lattice. GB segregation has a multitude of effects on alloy properties, as it induces structural effects [1,2] that include strengthening [3–5], embrittlement [6,7], corrosion resistance [8,9], and GB phase transitions [10,11]. And as such, controlling GB segregation is a handle for alloy design and optimization, and an essential tool for many engineering applications [12]. A prominent example of its utility is the use of segregants at the GB to kinetically [13–17] and thermodynamically [18–29] stabilize nano-grained alloys against grain growth. However, quantitative design of alloys with GB segregation in mind requires the ability to correctly predict the magnitude of such segregation in a given alloy system.

The first isotherm to predict the equilibrium solute segregation at GBs was proposed by McLean in 1957 [30]. In this model, the polycrystal is partitioned into two site-types, bulk (intra-grain) and GB sites. The extent of segregation of solute atoms is calculated using the following relationship:

$$\frac{X^{gb}}{1-X^{gb}} = \frac{X^{c}}{1-X^{c}} \exp\left[-\frac{\Delta H^{seg}}{kT}\right] \tag{1}$$

where X^c, X^{gb} are the atomic solute concentrations at the bulk and GB regions, respectively, k is Boltzmann's constant, T is temperature and ΔH^{seg} is the GB segregation enthalpy, which is defined as the enthalpy difference between a solute atom occupying a GB site (H^{gb}_{solute}) versus a bulk site (H^{c}_{solute}):

$$\Delta H^{seg} = H^{gb}_{solute} - H^{c}_{solute} \tag{2}$$

In Mclean's treatment, three tacit assumptions are made about the segregation enthalpy, namely that it can be used to characterize all GBs regardless of their specific crystallographic character, at any temperature and for any solute-solute interaction condition at the GB. Following McLean's isotherm, several other segregation isotherms have been proposed using different assumptions for solid solution behavior and different analytical relationships to calculate ΔE^{seg}. Prominent examples include those of Fowler-Guggenheim [31], Guttmann [32], and Wynblatt and Chatain [33]; for a detailed review of these and other models, we refer the reader to Refs. [1,2,33].

Nevertheless, all these thermodynamic models carry one critical assumption that we address in more detail in this thesis, namely that only one site-type exists at the GB, and consequently all GB sites have the same value of ΔH^{seg}.

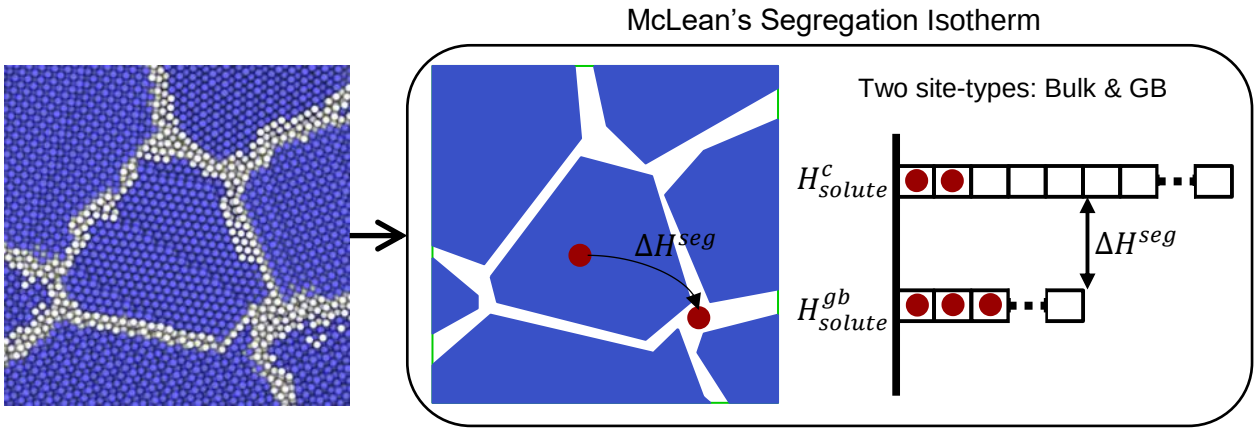

Figure 1: An illustration of the "averaged" McLean's approach to GB solute segregation. In this treatment, a solute atom can only occupy two site-types (or local atomic environments), the bulk and the GB. And thus, this simplification ignores the variety of site-types that should exist at the GB, as a result of its disordered nature.

The assumption of a single value of ΔH^{seg} for all GB sites is rather a significant simplification and is invalid for even the simplest types of GBs [34,35], as it takes into account neither the variety of types of GBs in a polycrystal, nor the variation of sites within each individual GB. In a polycrystal, the GB network has a variety of site-types that can either promote or inhibit segregation to different degrees, depending on their unique local atomic environments. This spectral nature is experimentally validated through observed variation of solute segregation across the GB network, as shown in **Figure 2**, for example, for Fe(c), and Pt(Au). The nature of the site spectrum will determine the equilibrium solute concentration at individual GBs and the overall average concentration across all GBs [35,36]. It can be handled by introducing a density of sites as proposed by White and Stein [37] and Kirchheim [38,39], with $F_i^{gb}\left(\Delta H_i^{seg}\right)$ the distribution function of GB segregation enthalpies over all site-types (i). The average global solute concentration across all GBs, $\bar{X}^{gb}$, can then be obtained by integrating solute concentration over all possible site-types [40]:

$$\bar{X}^{gb} = \int_{-\infty}^{\infty} X_i^{gb}\left(\Delta H_i^{seg}\right) \cdot F_i^{gb}\left(\Delta H_i^{seg}\right) \, \mathrm{d}\Delta H_i^{seg} \tag{3}$$

where $X_i^{gb}\left(\Delta H_i^{seg}\right)$ is the concentration of segregants at site-type (i).

A key component to this multiple site-type treatment is the nature of this spectrum $F_i^{gb}\left(\Delta H_i^{seg}\right)$, studies of which fall into three categories. First, analytical modeling of the GB has been conducted by Ashby et al. [41] using a polyhedral model, and by White and Coghlan [42] using a dislocation model. Second, model fitting to experimental data; this includes using an assumed Gaussian distribution of segregation energies at the GB to explain experimental data, as done by White and Stein [37], Kirchheim [38,39] and Suzuki [40]. Finally, atomistic simulations, which have been used extensively to typically study individual coincidence site lattice (CSL) GBs, such as the work by Udler and Seidman [43]; we refer the reader to Lejček et al. [44] for an extensive compilation of such atomistic calculations.

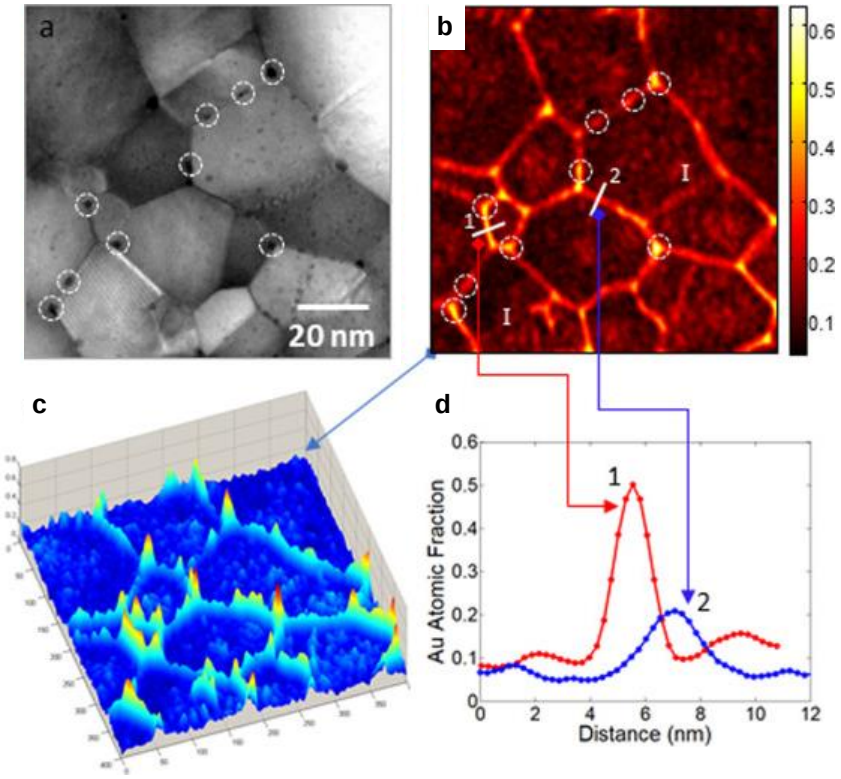

Figure 2: An illustration of experimentally observed variation of solute segregation across the GB space in polycrystals. (a-d) Scanning transmission electron microscopy and energy-dispersive x-ray spectroscopy mapping of Au solute segregation in Pt thin films [45]. Panels (a-d) adapted with permission from reference [45]; copyright 2019 Elsevier.

Nevertheless, a general shortcoming of these multiple-site studies is that its findings are typically limited to the specific systems analyzed, whether it is a single CSL GB or experimental data of averaged solute concentrations at the GB. These models are difficult to generalize to other polycrystalline systems, which is what is generally required for alloy design purposes. Certainly one could approach the problem by sampling a large set of boundaries and analyzing its collective distribution and behavior [46,47]. However, this approach is still hindered by the limitation of just using simplified structural representations or CSL GBs, which may not be generally reflective of the GB energies and populations in a full polycrystal [48]. Another approach is to study segregation in a representative polycrystal, prior implementations of which have only focused on exploring the equilibrium segregation state, without elucidating the GB segregation spectrum [49–55].

1.1. Research Objectives and Outline of Thesis

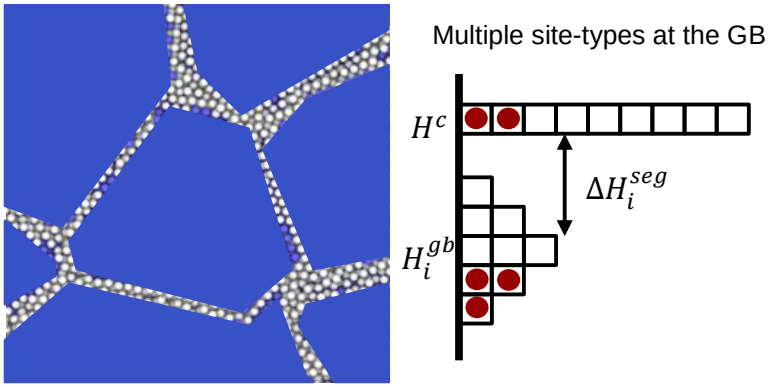

Figure 3: The proposed spectral framework to treat GB solute segregation in polycrystals. In contrast to the "averaged" approach outlined in **Figure 1**, this treatment incorporates the spectrum of local atomic environments, or site-types at the GB network.

To reiterate, most thermodynamics models for GB segregation use the simple assumption of a single type of GB site having a constant enthalpy of segregation ΔH^{seg}. As a result, these models use a regular solution model where the solutes are distributed randomly with no site preference. This assumption is invalid, even for the simplest type of grain boundary [34]. The impact of this simplification should be investigated and quantified. Solute ordering or site preference should be expected and is observed experimentally [12,26,56]. And thus, a proper model should be able to handle the expected spectrum of segregation energies in a polycrystals, as shown in **Figure 3**. In addition to the limitation imposed by the current thermodynamic models, there is a very limited

understanding of the spectral nature of GB segregation in polycrystals [57] – though most technically relevant alloys are used in a polycrystalline form – and a general lack of databases of segregation information relevant to them. In this thesis, we aim to address this gap in the GB segregation literature, by developing a thermodynamic and computational framework to handle, and elucidate the variation of solute segregation tendencies across the multidimensional GB space in polycrystals. We aim to answer the following questions:

- What is the nature of site distribution at GBs in a polycrystal? Could it be simplified and approximated for general systems?
- What is the impact of this distribution on the predictions of equilibrium solute segregation at GBs, in comparison to the classical "averaged" models?
- What are the implications of the distribution, and the expected solute ordering at GBs to alloy design?
- What is the effect of solute-solute interactions beyond the dilute-limit at the GB? How to account for it?

The thesis will use a combination of analytical methods and computational tools to answer these questions, and is structured as follows:

CHAPTER 2

We first begin by outlining the proper thermodynamic and computational framework for GB segregation in a polycrystalline binary alloy, and then explore the nature of the site-type spectrum at the GB in detail. We also provide useful simplifications and approximations that should facilitate generalization to many other alloy systems.

CHAPTER 3

We develop a machine learning framework that can accurately predict the segregation tendency, as quantified by the segregation enthalpy spectrum, for solute atoms at GB sites in polycrystals, based solely on the undecorated (pre-segregation) local atomic environment of such sites. We proceed to use the learning framework to scan across the alloy space, and build an extensive database of segregation energy spectra for more than 250 metal-based binary alloys.

CHAPTER 4

To highlight the implications of the findings of Chapters 2 and 3 to alloy design, we apply the acquired knowledge (and data) to the problem of designing and screening for nanocrystalline stability. We outline a more formally correct thermodynamic criteria to screen for thermodynamic stability of polycrystalline structures, accounting for the spectral nature of GBs. And, we proceed to apply the developed criteria to screen over 200 alloy combinations based on the computed segregation spectra from Chapter 3.

CHAPTER 5

In Chapters 1-4, the developed models and analysis assumed a dilute-limit solute regime. And thus, an important future direction for improvement is to extend the current models to handle solute concentrations beyond the dilute limit, where the extent of solute GB segregation is known to be concentration dependent. In this chapter, we take the first step in that direction, and decouple the two contributions to this composition dependence: (i) spectrality of atomic environments at the boundary and (ii) solute-solute interactions. Although only contribution (ii) is typically considered in the literature, we argue that both contributions are equally important to understand concentration dependence and correctly quantify GB solute segregation in a binary alloy.

CHAPTER 6

We discuss opportunities for future work to further improve our understanding of GB solute segregation, and help unlock its full potential as an alloy design tool.

2. SPECTRUM OF GRAIN BOUNDARY SEGREGATION ENERGIES IN A POLYCRYSTAL

As elaborated in Chapter 1, to predict the equilibrium segregation state in a given alloy, most thermodynamic models treat the full network of GBs as a single "entity", and thus use an "effective" segregation energy to describe it. This simplification ignores the spectral nature of available GB segregation energies in a polycrystal. In this chapter, we elucidate the nature of this spectrum computationally for a Mg solute in an Al polycrystal. We also outline a thermodynamic segregation isotherm that incorporates this spectrum, and employ the isotherm to study the effect of such a spectrum on predictions of the equilibrium GB segregation state.

2.1. THERMODYNAMIC MODEL FOR GB SEGREGATION WITH MULTIPLE SITE-TYPES

A polycrystalline system can be divided into two atomic site fractions, the crystalline (f^c) and GB (f^{gb}) fractions, where:

$$f^c + f^{gb} = 1 \tag{4}$$

In a closed system, for a prescribed global solute concentration X^{tot}, the following relationship must be obeyed:

$$X^{tot} = (1 - f^{gb})X^c + f^{gb}\bar{X}^{gb} \tag{5}$$

Whereas it is a reasonable assumption to have only a single site-type in the crystalline regions, the GB has a spectrum of site-types (i), which each occupies an atomic site fraction F_i^{gb} of the GB, thus:

$$\sum_i F_i^{gb} = 1 \tag{6}$$

The average GB solute concentration is then a weighted summation of the solute concentration at each site-type(i):

$$\bar{X}^{gb} = \sum_i F_i^{gb} X_i^{gb} \tag{7}$$

The solute concentration at each site-type X_i^{gb} is derived by White and Stein [37] as:

$$X_i^{gb} = \left[1 + \frac{1 - X^c}{X^c} \exp\left(\frac{\Delta E_i^{seg}}{kT}\right)\right]^{-1} \tag{8}$$

which is the same form as McLean's relationship Eq. (1), but in terms of site-type (*i*). Combining Eqs. (8), (7) and (5), we obtain:

$$X^{tot} = (1 - f^{gb})X^c + f^{gb} \sum_i F_i^{gb} \left[1 + \frac{1 - X^c}{X^c} \exp\left(\frac{\Delta E_i^{seg}}{kT}\right)\right]^{-1} \tag{9}$$

Eq. (9) provides the thermodynamic framework for a closed system that has multiple site-types at the GB. For a given set of inputs – F_i^{gb}, X^{tot}, f^{gb} and T– we can solve for the value of X^c that satisfies Eq. (9). Consequently, we obtain all the information about the system; solute concentration at each site-type and overall GB concentration can be obtained from Eqs. (8) and (7), respectively. This framework is valid for all solutes in the dilute limit, and beyond for weakly-interacting solutes; at higher solute concentrations, we expect solute-solute interactions at the GB to alter the nature of the spectrum, and consequently affect the equilibrium segregation state.

We note that although Eq. (9) is conceptually straightforward to derive, it has apparently been neither stated nor used previously in the literature. Instead, only Eqs. (7) and (8) are usually solved, which amounts to employing the assumption that $X^c = X^{tot}$. In most cases this is an invalid assumption, which is only valid in the limit of very large grain sizes:

$$X^c = \lim_{f^{gb} \to 0} X^{tot} \tag{10}$$

Therefore, Eq. (9) is the proper, generalized framework to solve, as it explicitly accounts for the fact that $X^c \neq X^{tot}$ in a closed polycrystalline system.

Finally, we note that Eq. (9) is closely analogous to Kirchheim's model – though derived differently – for multiple site-types at the GB [38,39], which he expressed in terms of a Fermi-level energy (E^F):

$$X^{tot} = (1 - f^{gb})\left[1 + \exp\left(\frac{-E^F}{kT}\right)\right]^{-1} + f^{gb} \sum_i F_i^{gb} \left[1 + \exp\left(\frac{\Delta E_i^{seg} - E^F}{kT}\right)\right]^{-1} \tag{11}$$

To arrive at Eq. (11), Kirchheim [38,39] directly applied Fermi-Dirac statistics [58,59] to solve for solute distribution at the GB, since the partitioning of solute atoms between different energy levels with a maximum of one solute atom occupying a given site should result in a Fermi-like

distribution [58–60]. Indeed, Mclean's model, Eq. (1), and White and Stein's model, Eq. (8), are both degenerate of Fermi-Dirac statistics [61–65]. This similarity means that we can recover Eq. (9) from Eq. (11) by setting:

$$E^F = kT \ln\left(\frac{X^c}{1 - X^c}\right) \tag{12}$$

Therefore, Eq. (9) provides a general thermodynamic framework for GB segregation that obeys Fermi-Dirac statistics, where we directly solve numerically for X^c instead of Kirchheim's "Fermi energy" (E^F), which lacks a simple interpretable physical meaning in this context.

To map back results from this framework into Mclean's relationship, Eq. (1), the concept of an effective average segregation energy $\Delta\bar{E}_{seg}^{eff}$ is introduced, which is useful for comparison with Mclean's isotherm, and to understand experimental measurements of GB segregation in which typically only segregation averages can be measured. The effective McLean segregation energy was derived by Steigerwald and Wynblatt [46] as:

$$\Delta\bar{E}_{seg}^{eff} = \frac{1}{\bar{X}^{gb}(1 - \bar{X}^{gb})} \sum_i F_i^{gb} \Delta E_i^{seg} X_i^{gb} \left(1 - X_i^{gb}\right) \tag{13}$$

Now that the thermodynamic framework is established, a key component is the spectrum of segregation energies in the GB, $F_i^{gb}(\Delta E_i^{seg})$. To elucidate its nature, we use molecular dynamics and statics simulations to directly compute such a distribution in a polycrystal.

2.2. Simulation Methodology

The molecular dynamics simulator LAMMPS [66] is used for all molecular dynamics and statics simulations, with the choice of a model binary system being guided by the quality of available interatomic potentials. We choose Al-Mg, as its embedded atom method potential – developed by Mendelev et al. [67] – gave GB segregation energies comparable to those from density functional theory simulations [68]. Nevertheless, the computational framework detailed here is extensible to any binary alloy system for which interatomic potentials are available. To obtain a representative polycrystal, we start by filling a cube with 36 nm edge length with 96 randomly oriented grains, constructed using Voronoi tessellations, using the toolkit Atomsk [69]; the initial simulation cell has 2,818,993 atoms. The polycrystal is then structurally relaxed using conjugate gradient energy minimization, followed by thermal annealing under an isothermal-

isobaric ensemble with a Nose-Hoover thermostat/barostat set at 700 K ($\sim 0.7\, T_{melt}$) and zero pressure. The sample is thermally annealed for 500 ps, using an integration time step of 1 fs. It is then slowly cooled with a cooling rate of 3 K/ps down to 0 K, which is finally followed by a conjugate gradient energy minimization.

To identify the number of distinct grains in the thermally annealed sample from atomic positions, we use a grain identification algorithm similar to that in Refs. [70,71]. We start by calculating the per-atom orientation using the polyhedral template matching method [72]. A new grain is initiated with a random unassigned seed atom, then nearest neighbor atoms are assigned to the grain if the misorientation is less than 1°; this loop is repeated until there are no more neighbor atoms to add. If a grain is less the 200 atoms, the grain is removed and its atoms are marked as unassigned again. The aggregation process is repeated until all possible grains in the system are identified. This procedure provides a good estimate of the number of distinct grains in the sample without being computationally prohibitive, and is executed using the open visualization tool OVITO [73] python scripting capabilities. Structural identification and visualization of atomic configurations are also carried out using OVITO throughout the chapter. To identify GB sites, we use the adaptive-common neighbor analysis method [74] to identify non-FCC regions, which are all assumed to be GB sites. We use the per-atom orientation, obtained using the polyhedral template matching, to calculate grain orientations, GB disorientations and to perform texture analysis with the toolbox MTEX [75]. Finally, the thermally annealed polycrystal has 72 grains with an average grain size of ~11 nm, a near-random texture index of 1.53, 488 GBs, and 414,538 GB atoms, which corresponds to an atomic site fraction of 14.7%.

Figure 4(a) and (b) show the polycrystal's unique grains and GB atoms, respectively, and Figure 5 shows the disorientation distribution for its 488 GBs. Between the near random crystallographic orientations and near-uniform sampling of GB disorientation space, this single sample is considered a good model for a general polycrystalline sample without strong selection biases in the GB distribution; this is a base case for understanding the GB segregation energy spectrum in its full breadth.

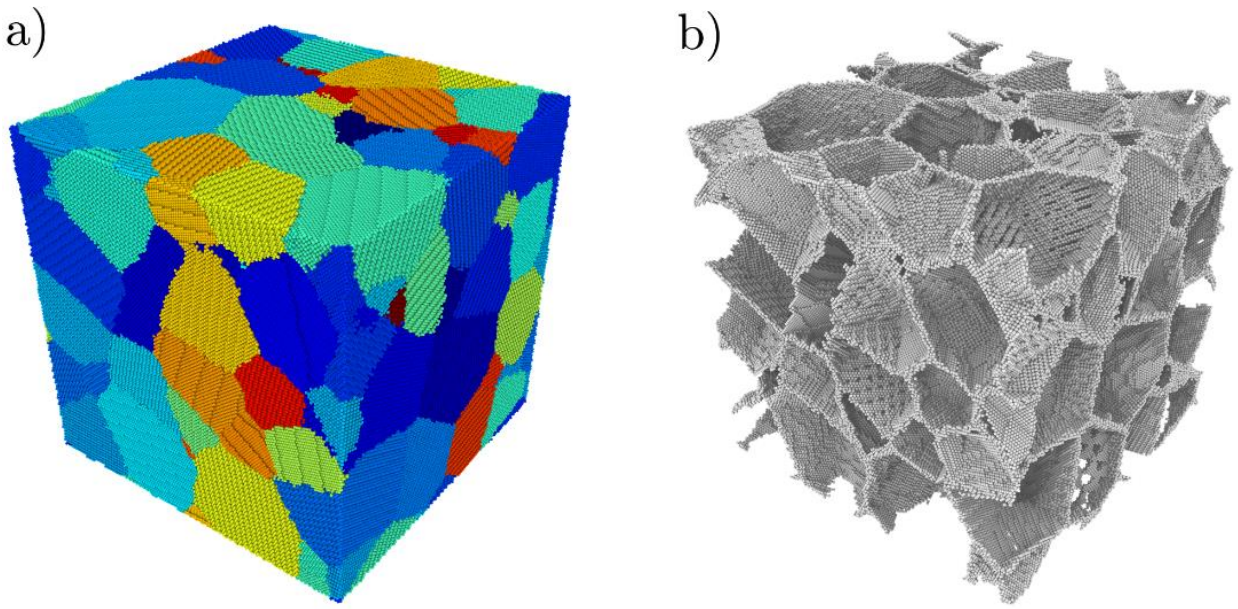

Figure 4: The thermally annealed $(36\ nm)^3$ aluminum polycrystal; (a) 72 distinct grains and (b) 414,538 GB atoms used for computing the distribution of segregation energies in the polycrystal.

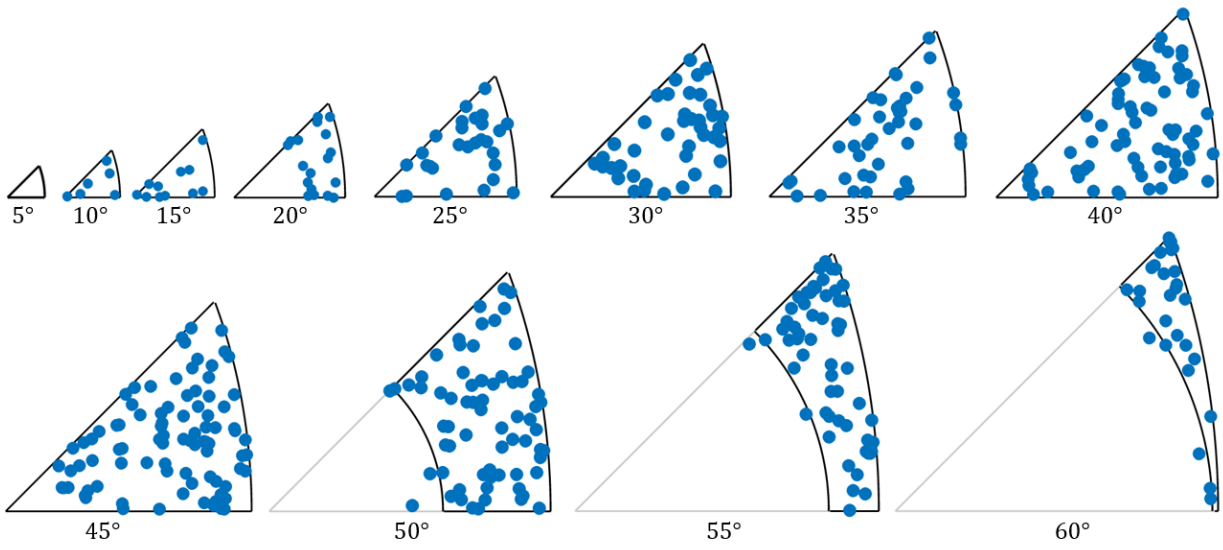

Figure 5: Disorientation distribution of the 488 GBs in the annealed $(36\ nm)^3$ Al polycrystal, represented in sections of constant misorientation angle where each section is the standard stereographic triangle of the 432 cubic group [76]; points that apparently lie outside the fundamental zone arise due to the binning in disorientation angle amongst sections.

We calculate the dilute-limit segregation energy at each GB site (i) using molecular statics at 0 K, as follows:

$$\Delta \mathrm{E}_{\mathrm{i}}^{\mathrm{seg}} = \mathrm{E}_{gb,\mathrm{i}}^{\mathrm{solute}} - \mathrm{E}_{\mathrm{c}}^{\mathrm{solute}} \tag{14}$$

where $\mathrm{E}_{gb,\mathrm{i}}^{\mathrm{solute}}$ is the total energy of the system with a solute atom – Mg – at site (i) and $\mathrm{E}_{\mathrm{c}}^{\mathrm{solute}}$ is the total energy of the system with a solute at a reference bulk site, which is chosen such that it is at the center of a 6 nm sphere of FCC atoms, in order to avoid elastic interaction effects with the GBs. Both energies are obtained after structurally relaxing the system using conjugate gradient energy minimization with an energy tolerance of 10^{-25} eV and a force tolerance of 10^{-25} eV/$\dot{A}$. We only consider substitutional GB segregation in this chapter, for which Eq. (14) is valid, and the convention chosen here is that segregation will occur if $\Delta \mathrm{E}_{\mathrm{i}}^{\mathrm{seg}}$ is negative i.e. the solute will be at a lower energy state at the GB; note that this convention is opposite of that sometimes used in the GB segregation literature in which positive energies denote segregation preference. The calculation in Eq. (14) is performed for all 414,538 GB sites in the polycrystal.

It is important to point out that ideally, it is the free energy of segregation ΔG^{seg} that should be computed. However, it can be approximated by the internal energy ΔE_{seg} to a good extent. To elaborate, ΔG_{seg} in a closed system with fixed E, P, T and N, is expressed as [46]:

$$\Delta G_{seg} = \Delta E_{seg} - P\Delta V - T\Delta S_{seg}^{xs} \tag{15}$$

where P is the pressure, ΔV is the change in volume and ΔS_{seg}^{xs} is the excess entropy of segregation. As we still maintain Mclean's assumption of a regular solution model, the excess entropy is assumed to vanish [46]. The term $P\Delta V$ is negligible [77] in solids and thus can also be ignored. Therefore, we can approximate $\Delta G_{seg} \approx \Delta E_{seg}$, which can be easily computed at 0 K using molecular statics.

2.3. THE SPECTRUM OF SEGREGATION ENERGIES

2.3.1. Properties of the spectrum

The calculated spectrum of dilute-limit segregation energies of a Mg solute at all 414,538 GB atoms in the $(36\ \mathrm{nm})^3$ Al polycrystal is shown in Figure 6. The distribution is normal-like and has a slightly negative median of -6.6 kJ/mol and a standard deviation of 15.2 kJ/mol, which suggests

that on average GB sites are favorable for Mg solutes in Al, with a most favorable segregation energy of −73 kJ/mol. Indeed, roughly two-thirds of the sites in this sample exhibit a GB segregation preference and one-third are energetically unfavorable with respect to bulk dissolution. In comparison, Huber et al. [78] reported a distribution mean of 6.8 kJ/mol and a standard deviation of 19.3 kJ/mol for a set of 38 low and high symmetry GBs, and thus approximately only 40% of GB sites were predicted to be favorable for segregation, which signifies that the chosen set of GBs are not necessarily representative of a full polycrystal.

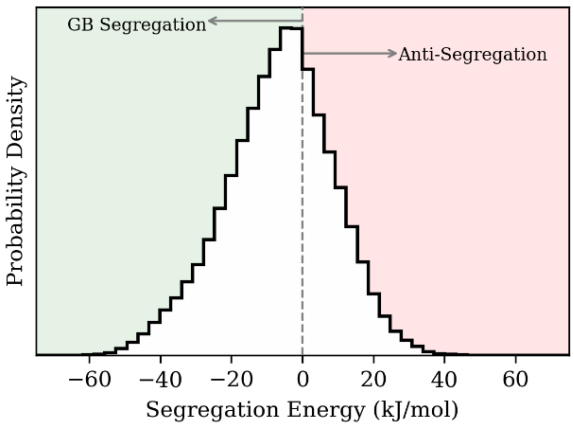

Figure 6: The distribution of 414,538 GB dilute -limit segregation energies for an Mg solute in a $(36\ nm)^3$ polycrystalline Al sample.

It is the extreme left tail of the distribution in Figure 6 that will be the primary target of segregation, so it is important to examine whether these sites are confined to a specific region in the polycrystal or are widely spread among different GBs; clustering of those sites might indicate one or a few unique GBs that dominate the problem. We plot the favorable segregation sites from -75 to 0 kJ/mol over three equally spaced intervals in

Figure 7: Plot of all favorable GB segregation sites in the polycrystal from -75 to 0 kJ/mol divided over three equal intervals. The most favorable sites are well spread over the GB network with no apparent clustering at a single GB.

. We also plot the two-point correlation function, Figure 8, for different energy intervals – up to the 10^{th} percentile – using the Landy-Szalay estimator [79], which traces the extent of clustering by quantifying the excess probability $\xi(x)$ relative to a random distribution of solute atoms at the GB. It is clear both qualitatively in Figure 7 and quantitatively in Figure 8 that the favorable sites

for GB segregation are not clustered, but are rather well spread over all boundaries of the polycrystal. Even for the most extreme selections of the energy spectrum (the most extreme 2%), the two-point correlations in the system are essentially random ($\xi < 0.1$) for distances greater than a few nanometers. Thus, any solute additions will also be well spread over the polycrystal GB network. Importantly, this signifies that at dilute concentrations, solutes will be able to occupy the most favorable sites with no significant solute-solute interaction at the GB.

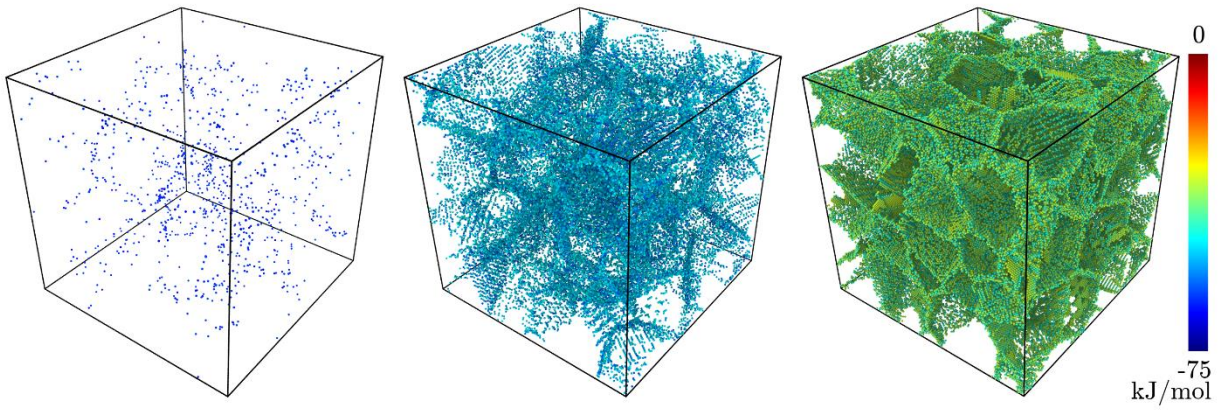

Figure 7: Plot of all favorable GB segregation sites in the polycrystal from -75 to 0 kJ/mol divided over three equal intervals. The most favorable sites are well spread over the GB network with no apparent clustering at a single GB.

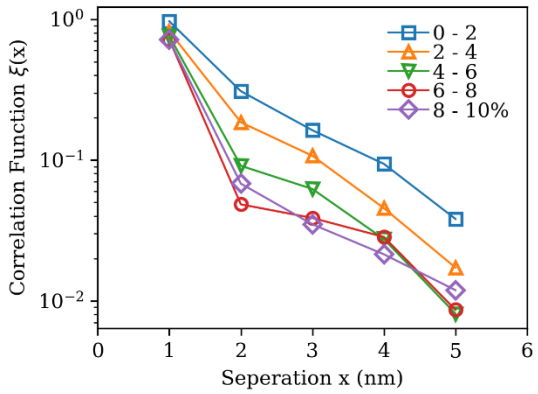

Figure 8: Two-point correlation function for five intervals (percentile of the spectrum) of the most favorable segregation sites. ξ(x) approaches zero around 3 nm, which signifies that, at this separation distance, the spread of favorable sites over the GB network is indistinguishable from a random one.

To further test whether this spectrum is unique to this specific sample or more generally representative of polycrystals, we have repeated this computation numerous times for additional structures. Some typical results for three smaller, thermally annealed, polycrystalline samples –

listed in Table 1 – are shown in Figure 9. Here we plot the segregation energy distribution in a cumulative fashion to avoid any bias from binning, and highlight possible differences amongst the samples, which are also revealed by the differences between these distributions plotted above the figure; these never exceed 0.02 and are mostly well below 1%. The near perfect overlap of the distributions suggests a universality of the segregation spectrum, with any one sample being representative of all of them. Using any of these distributions will result in robust model predictions for the equilibrium segregation. As an example, use of Eq. (13) to render an "effective" GB segregation energy for these four spectra gives values of -8.8, -8.5, -8.3 and -8.3 kJ/mol, in ascending order of sample size, for $X_{Mg}^{tot} = 1\%$ at T = 300 K. Therefore, we suggest that as long as a polycrystal has a statistically significant number of GB atoms, it is reasonable to use a single distribution function F_i^{gb}. Moving forward, we use the computed distribution of the (36 nm)^3 sample – the largest – as the representative spectrum for an Al-Mg alloy.

Table 1: Comparison of three smaller polycrystalline samples with the (36nm)^3 Al polycrystal; $\Delta\bar{E}_{seg}^{eff}$ is for X_{Mg}^{tot}=1% at T = 300K.

Size	Grains	d^{gb}	GB atoms	$\Delta\bar{E}_{seg}^{eff}$
(15 nm)3	8	9 nm	37,515	-8.8
(20 nm)3	8	12 nm	60,444	-8.5
(25 nm)3	20	11 nm	134,518	-8.3
(36 nm)3	72	11 nm	414,538	-8.3

Next, we apply the thermodynamic model given by Eq. (9) and examine its impact on our understanding of the equilibrium segregation state. The Fermi-Dirac distribution of Eq. (9) is the thermal equilibrium expected in such a system, and should exactly match the outcome of a Monte Carlo sampling directly on the computational ensemble. We have validated this expectation by assigning an energy of zero for all bulk lattice sites and the computed ΔE_i^{seg} for GB site (i), and carrying out a standard Monte Carlo process at a given solute concentration, with an acceptance probability that is the minimum of [1, $exp(-\Delta E/kT)$]; a similar process is described in, e.g. Ref. [80], and we find that 10,000 swaps per atom achieve an equilibrated configuration here.

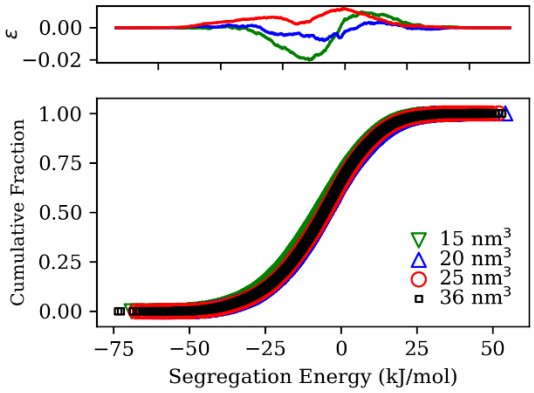

Figure 9: The cumulative fraction of segregation energies for the four different polycrystalline samples listed in Table 1, and the residual (ε) of the three smaller samples against the reference $(36\ \text{nm})^3$ sample.

Either direct use of Eq. (9) or the Monte Carlo sampling are found to both give the same equilibrium, which can be visually verified in Figure 10(a), which shows the occupation of GB segregation states for both of these approaches for just one example state of many that we have considered: $X_{Mg}^{tot} = 5\%$ alloy at T = 700 K. The figure also shows how temperature affects the equilibrium, spreading the solute distribution to higher energy states up beyond the nominally favorable segregation sites to values as high as 10 kJ/mol (unfavorable) at 700 K, and decreasing the overall $\bar{X}^{gb}$. The net effect of temperature is shown for a variety of compositions in Figure 10(b), and the magnitude (absolute value) of the effective segregation energy that matches is plotted in Figure 10(c). Two interesting effects can be observed here. First, the impact of the temperature; at fixed global composition X^{tot}, increasing T will cause segregants to entropically redistribute to other less favorable sites in the boundary, as well as to partially desegregate from the GB into the bulk, which causes $\bar{X}^{gb}$ to decrease. The effect on $\left|\Delta\bar{E}_{seg}^{eff}\right|$, which increases with increasing T, is less intuitive; it is the result of $\bar{X}^{gb}$ being less sensitive to T than Mclean's model predictions [42]. Therefore, using $\left|\Delta\bar{E}_{seg}^{eff}\right|$ obtained from a lower temperature will underestimate $\bar{X}^{gb}$ at higher temperatures, and thus to compensate for this error, $\left|\Delta\bar{E}_{seg}^{eff}\right|$ increases with increasing temperature. Second, the impact of global composition X^{tot}; at fixed T, increasing X^{tot} will cause $\left|\Delta\bar{E}_{seg}^{eff}\right|$ to decrease, while $\bar{X}^{gb}$ increases as expected. At low X^{tot}, the solute atoms will occupy the most favorable GB sites and thus have a high value for $\left|\Delta\bar{E}_{seg}^{eff}\right|$, and as X^{tot}

increases, segregated atoms begin to occupy less favorable GB sites, which causes the overall $\left|\Delta\bar{E}_{seg}^{eff}\right|$ to decrease.

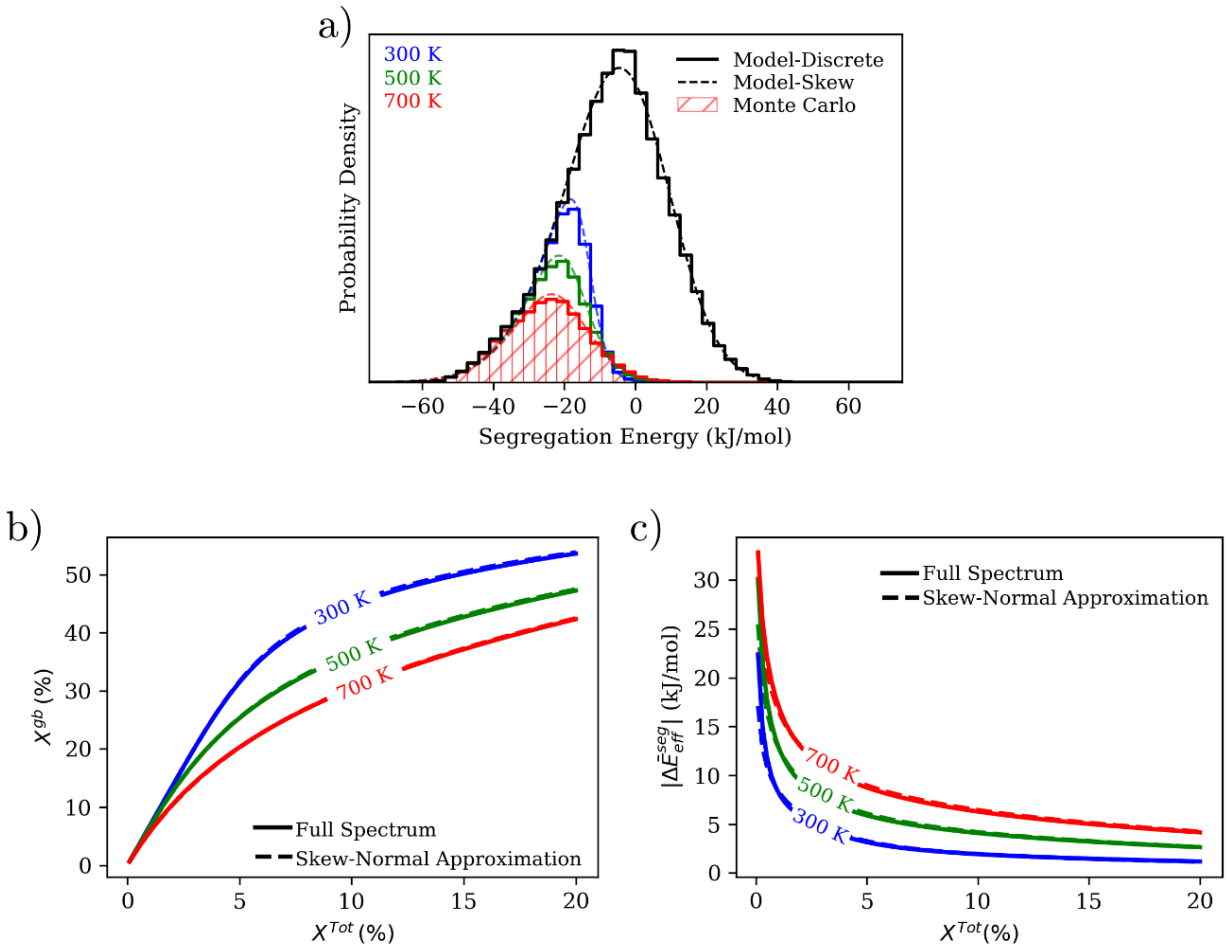

Figure 10: (a) The equilibrium segregation state in the (36 nm)^3 Al polycrystal with a solute addition of $X_{Mg}^{tot} = 5\%$ at T = 300, 500, 700 K. The discrete model Eq. (9), skew-normal model Eq. (17) and the Monte Carlo simulation at T=700 K, are given by the solid lines, dashed lines, and hatched area, respectively; predictions of all three methods match closely. (b)(c) Equilibrium $\bar{X}^{gb}$ and $\left|\Delta\bar{E}_{seg}^{eff}\right|$ as a function of X_{Mg}^{tot} and T, using the full discrete spectrum and best-fit skew-normal approximation.

2.3.2. Approximations of the spectrum

While we have been using the full spectrum of computed segregation energies thus far, it would be very useful to generalize this distribution in a simple analytical manner reasonably approximating the full discrete distribution. We can restate the model in a continuous representation with Eqs. (7), (9) and (13) expressed, respectively as:

$$\bar{X}^{gb} = \int_{-\infty}^{\infty} X_i^{gb} F_i^{gb} \; d\Delta E_i^{seg} \tag{16}$$

$$X^{tot} = (1 - f^{gb})X^c + f^{gb} \int_{-\infty}^{\infty} F_i^{gb} \left[1 + \frac{1 - X^c}{X^c} \exp\left(\frac{\Delta E_i^{seg}}{kT}\right)\right]^{-1} d\Delta E_i^{seg} \tag{17}$$

$$\Delta \bar{E}_{seg}^{eff} = \frac{1}{\bar{X}^{gb}(1 - \bar{X}^{gb})} \int_{-\infty}^{\infty} F_i^{gb} \, \Delta E_i^{seg} \, X_i^{gb}\left(1 - X_i^{gb}\right) \, d\Delta E_i^{seg} \tag{18}$$

where F_i^{gb}, X_i^{gb} are now continuous functions of ΔE_i^{seg}.

We had earlier noted the similarity of the distribution in Figure 6 with a normal distribution, and for the sake of generalization we adopt a more flexible skew-normal distribution, F_i^{gb} with which to fit it:

$$\mathrm{F_i^{gb}} = \frac{1}{\sqrt{2\pi}\,\sigma} \exp\left[-\frac{\left(\Delta E_i^{seg} - \mu\right)^2}{2\sigma^2}\right] \mathrm{erfc}\left[-\frac{\alpha\left(\Delta E_i^{seg} - \mu\right)}{\sqrt{2}\,\sigma}\right] \tag{19}$$

where μ, σ and α are the fitted location, scale and shape of the distribution, respectively. A best fit for the distribution Figure 6 gives $\mu = 6.11$ kJ/mol, $\sigma = 19.82$ kJ/mol and $\alpha = -1.35$, shown in Figure 10(a). The low magnitude of the skew parameter α supports the observation that the distribution is relatively near normal in the present case.

As shown in Figure 10, the skew-normal approximation captures most all of the fine details of the solute occupation fractions at different GB site-types. Furthermore, over a wide range of X^{tot} and T, the analytical approximation captures the segregation state as shown in Figure 10(b) and (c) – dashed line; there is at most a negligible error in $\bar{X}^{gb}$ of less than 1% at 700 K. This provides a powerful tool to characterize the population of segregation energies for arbitrary binary alloys in a simple manner, as only three parameters are needed to describe the whole population, and we have reasons to expect this to be generally applicable across polycrystals based on Figure 9. This simplification allows us to easily and accurately solve for the equilibrium segregation states – using just a single equation and three computed parameters – for different d^{gb}, T and X^{tot}. For

even further simplification, the normal approximation can be used, which reduces the number of fitted parameters to two, albeit with a slight increase in error – in this case, less than 3% error in $\bar{X}^{gb}$ at 700 K (not shown).

2.3.3. Comparison with McLean-type models

So far, we have shown a thermodynamic model that can be used to solve for the equilibrium solute segregation state in a polycrystal; the model explicitly accounts for multiple site-types across many GBs and can be used in conjunction with a simple skew-normal approximation of the distribution. At this point, we would like to elaborate such a spectral approach is necessary, and provides more physical outputs as compared with typical isotherms that use Mclean's single site-type formalism. For this purpose, we compare the predictions of equilibrium $\bar{X}^{gb}$ as a function X^{tot}, with our proposed thermodynamic model – using the full discrete distribution, skew-normal and normal approximations – versus just using a single averaged $\Delta\bar{E}_{seg}^{eff}$ = -5, -10, -20 kJ/mol; this is shown in Figure 11.

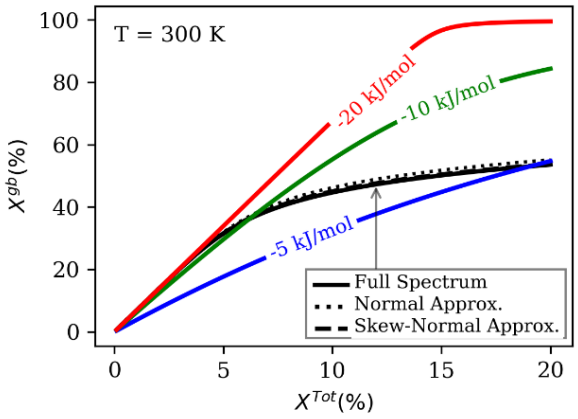

Figure 11: Comparison of $\bar{X}^{gb}$ predictions of the thermodynamic model using the full spectrum and approximated distributions versus using a single averaged $\Delta\bar{E}_{seg}^{eff}$ in Mclean's model.

It is clear from this presentation that a using a McLean type average can never correctly capture the physics of GB solute segregation over any significant range of X^{tot}; a single value will only correctly predict the segregation extent for a narrow composition range, such as using $\Delta\bar{E}_{seg}^{eff}$ = -10 kJ/mol for X^{tot} = 0-5%. This observation is reasonable – it can be deduced simply by looking at

Figure 10(c), which shows the variation of $\left|\Delta\bar{E}_{seg}^{eff}\right|$with composition; the dependency is non-linear and cannot be simply replaced with an average value. Importantly, this nonlinearity has nothing to do with solute-solute interactions in the grain boundary, which are frequently attributed with decreasing segregation energies at higher concentrations in the Fowler-type view [31]. Rather, the nonlinearity in Figure 10(c) and Figure 11 is entirely due to the spectral nature of GB segregation, with higher concentrations forcing the occupation of ever-less-energetically favorable sites.

2.3.4. Implications for experimental results

Figure 11 highlights the predicament of fitting experimental segregation measurements to McLean's model – something frequently done in the literature – in order to obtain a single segregation energy to describe the system; If a measurement of $\bar{X}^{gb}$is done at a high X^{tot}, the calculated $\Delta\bar{E}_{seg}^{eff}$ will underestimate the segregation extent at lower X^{tot}; conversely, fitting $\Delta\bar{E}_{seg}^{eff}$ at low X^{tot} will overestimate the segregation extent at higher X^{tot}. Therefore, a more accurate approach would be to fit experimental data directly to an approximation of the full distribution $F_i^{gb}\left(\Delta E_i^{seg}\right)$, using Eq. (16), which correlates the measured $\bar{X}^{gb}$ and X^c. For simplicity, we can assume a normal distribution (i.e., take $\alpha = 0$ in Eq. (19)), which requires fitting only two parameters (μ and σ). To do the fitting, we need a minimum of two experimental measurements of $\bar{X}^{gb}$ versus X^c, which can be obtained from measurements conducted at different X^{tot} and a fixed temperature, or different temperatures and a fixed X^{tot}.

As an example, we have performed this procedure for the weakly segregating Ni-W system in its as-electrodeposited condition, for which experimental measurements of $\bar{X}^{gb}$ versus X^c are obtained from Detor et al. [81]. The fitted normal distribution for Ni-W gives $\mu = 3.6$ kJ/mol and $\sigma = 9.4$ kJ/mol. For comparison, we plot the predicted distribution of segregated W atoms among available GB sites for one of the experimental measurements in Figure 12(a), for which the model correctly predicts the measured $\bar{X}^{gb} = 17.3\%$ at $X^c = 9.9\%$; Figure 12(b) shows the predicted $\bar{X}^{gb}$ over a wide range of X^c. The simplicity of this procedure provides experimentalists a powerful tool to compute the spectrum of GB segregation energies for any given binary alloy.

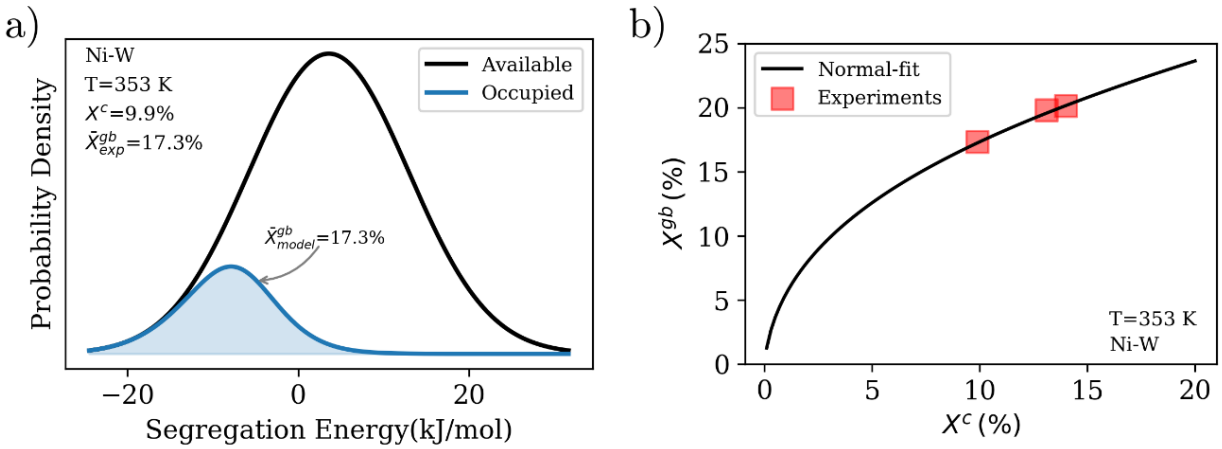

Figure 12: Fitting a normal distribution of segregation energies to experimental measurements of $\bar{X}^{gb}$ versus X^c for the Ni-W system, which are obtained from Detor et al. [81]: (a) predicted distribution of segregated solute atoms at $X^c = 9.9\%$ and (b) predicted $\bar{X}^{gb}$ as a function X^c.

2.4. Conclusion

In summary, while GB segregation has long been understood to be a Fermi-Dirac-type situation in which favorable sites at GBs are filled with solute in increasing energetic order, almost all work on GB segregation has proceeded by ignoring the spectrum of various GB sites and simplifying the problem to a single-valued GB segregation energy. While such a view has proven pragmatic for a number of simple phenomena, we argue that further progress in alloy design with GB segregation in mind will benefit from development of the full, spectral view, especially for polycrystals that inevitably sample the spectrum very broadly. We have therefore fully elaborated the thermodynamic framework to predict the equilibrium GB segregation state in polycrystalline binary alloys analytically and computationally. The spectrum of available GB segregation energies was determined for a specific case, Mg in Al, using atomistic simulations. The main findings are:

- A thermodynamic model –Eq. (9)– is developed to solve for the equilibrium segregation state in a polycrystalline binary alloy. To use an approximated (continuous) distribution instead of the full spectrum, Eq. (17) is given.
- We find that the spectrum of segregation energies in a polycrystal is a normal-like distribution, which can be very accurately approximated by a skew-normal distribution. Therefore, only three fitted parameters are needed to describe this distribution for a given binary alloy. Our result holds for a variety of polycrystals that we have studied

computationally, and we expect that such a 3-parameter distribution function will have broad applicability for most all polycrystals to a very good approximation.

- McLean-type models, which assume a single site-type at the GB, do not capture the physics of solute segregation at actual GBs, which have multiple site-types. Whereas the failure of McLean-type models is well known in cases beyond the dilute limit where solutes interact, here the failure of the McLean approach is entirely due to the neglect of the segregation spectrum without any solute interactions at all. We propose that in future studies of GB segregation two (or three) parameters be tabulated to capture the spectrum of sites rather than use any single value, which will not be accurate.

3. LEARNING GRAIN BOUNDARY SEGREGATION ENERGY SPECTRA IN POLYCRYSTALS

In chapter 2, we showed that the spectrum of ΔE_i^{seg} (the enthalpic drive for a solute atom to segregate to a GB site-type (i)) in a polycrystal will determine the extent of equilibrium GB segregation in an alloy [37,39,82]. And, we showed this spectrum to be captured by a skew-normal distribution for an Mg solute segregation in an Al polycrystal [82]. However, the computation of these segregation spectra is a resource-intensive task. For example, a $(50\ \text{nm})^3$ Al polycrystal with an average grain size of 10 nm has roughly one million GB sites, which translates to a million atomistic calculations, where a solute atom is placed substitutionally at each GB site independently and allowed to relax. This makes the task of investigating different microstructures (i.e. multiple polycrystalline samples) cost-prohibitive for a given alloy.

In this chapter, we propose a machine learning (ML) framework that can accurately predict the relaxed segregation energy of a solute atom in a GB site, solely based on its undecorated (pre-segregation) atomic environment. Our approach is tiered and offers two models. The first is a high-fidelity model that is trained to accurately capture the variation of segregation energy across a large swath of the GB space, and thus can be used to study an alloy system in detail and instantaneously evaluate segregation for different microstructures. The second is an accelerated model that uses dimensionality reduction to reproduce the high-fidelity model – with a minimal loss in accuracy – using three orders of magnitude fewer data-points for training (only 100 sites). We use the accelerated approach to scan across the alloy space, and build a first-of-its-kind database giving GB segregation spectra for all aluminum, magnesium, and transition metals-based binary alloys for which an interatomic potential exists in the Interatomic Potentials Repository [83,84] of the National Institute of Standards and Technology (NIST) - a total of 259 binary alloys. This database allows us to identify alloys of interest with minimal computational cost, for which high-fidelity models can be trained and used. The proposed ML framework and the resulting spectral segregation database should provide a general and broadly applicable alloy design toolbox relevant to all material properties impacted by solute segregation.

3.1. HIGH-FIDELITY ML MODEL FOR GB SEGREGATION

If a solute atom is substitutionally placed at a GB site and is allowed to relax, its local neighboring atoms will be affected (and possibly displaced) by the introduced elastic and chemical interactions. Hence it follows that the local atomic environment (LAE) of a GB site will influence its favorability for solute segregation, and thus this environment should be accurately captured in any learning model that aims to correlate the undecorated (pre-segregation) GB site to its final decorated (post-segregation) relaxed state. So far, the state-of-the-art learning models in the literature use simple well-known structural features [78,85], such as atomic volume, coordination, and Voronoi parameters, which mostly limit the description of the LAE to its first nearest-neighbor atoms. Instead, we propose using an atom-centered feature extraction method "descriptor" that encodes the local atomic environment around an atom within a cutoff radius [86,87]. Such descriptors – also known as "fingerprints" – are developed and widely used to construct ML-based interatomic potentials; examples include the atom-centered symmetry functions [88], bispectrum components [89,90], and smooth overlap of atomic positions (SOAP) [91]. There are two main advantages to using such atom-centered descriptors. The first is that no *a priori* knowledge or selection of what constitutes an important structural feature of the LAE (such as volume, coordination, etc.) is required, but rather, by using a complete description of the LAE within a cutoff radius, we relegate the decision of learning the most important features to the ML model. The second is that the use of a large cutoff radius ensures that the most dominant interactions between the solute atom and its LAE are captured. As these descriptors are borrowed from the interatomic potential fitting literature, we can think of our approach as fitting a "pseudo interatomic potential" for solute segregation at GBs.

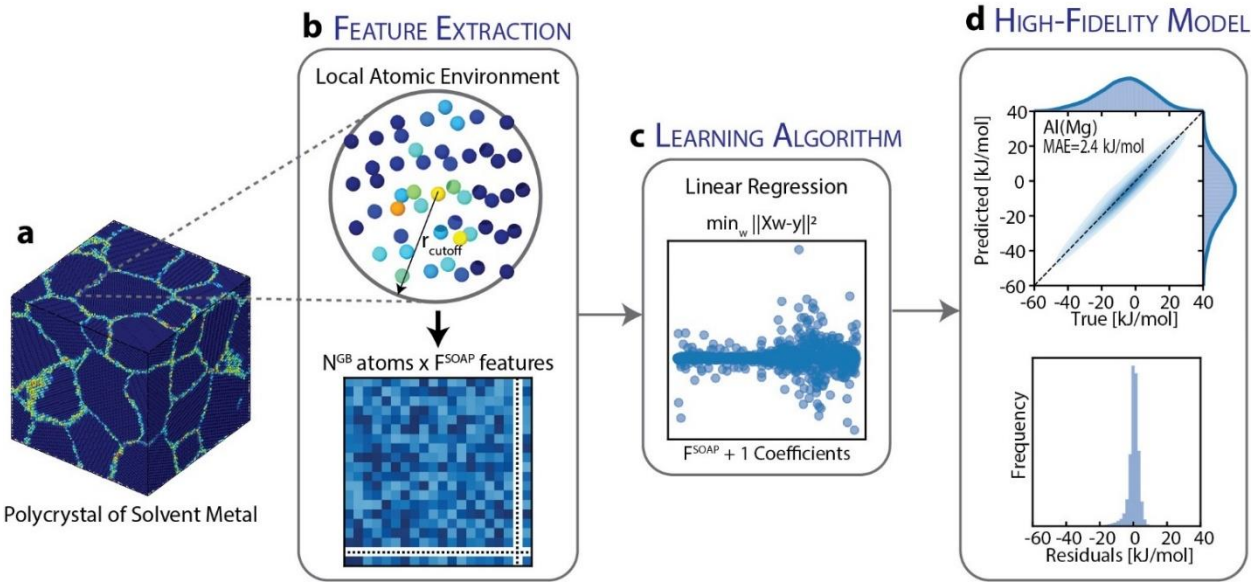

Figure 13: High-fidelity ML model to learn Mg solute [67] segregation at GBs in an Al polycrystal. For the (a) 20x20x20 nm^3 thermally annealed Al polycrystal with 16 grains (colored by the centro-symmetry parameter [92]), (b) the LAE of every identified GB atom is transformed into a feature vector, using the SOAP method [91] with r_{cutoff}=6Å, to construct a feature matrix for the full GB network (N^{GB} atoms x F^{SOAP} features), which is used as the input to the (c) learning algorithm (linear regression) to learn Mg GB segregation energies, using a 50/50 training/testing split. (d) predictive performance – mean absolute error (MAE) – of the trained ML model across the full GB network.

The proposed high-fidelity ML model is summarized in Figure 13, which shows two main steps: (a) feature extraction and (b) a learning algorithm. For feature extraction, we use the SOAP method [91], as it was recently shown to perform well in describing GB environments (albeit for the different problem of predicting GB energies) [93]. The SOAP method produces for a given GB site and its LAE within a cutoff radius, a feature vector (descriptor) that is invariant under all physical symmetries (permutation, translation, rotation, etc.). The size of the feature vector is controlled by the SOAP hyperparameters (detailed in the methods section), which, in essence, determines the resolution of the vector and its sensitivity to changes in the LAE. In this work, the SOAP feature vector for each GB site has F^{SOAP}=1,015 features. For the cutoff radius, we use 6 Å, which is a conservative cutoff used in constructing interatomic potentials, as it captures the most dominant atomic interactions for an atom with its LAE [86,94]. We note that, though we opted to use the same F^{SOAP} and a radial cutoff of 6Å for all binary alloys (as optimal parameters that require minimal input from the user), this procedure is flexible, and one could, by further optimizing the SOAP hyperparameters to the specific alloy of interest, improve the accuracy of the ML model.

(For example, a solute atom that has a large size mismatch with solvent atoms could benefit from a larger radial cutoff.)

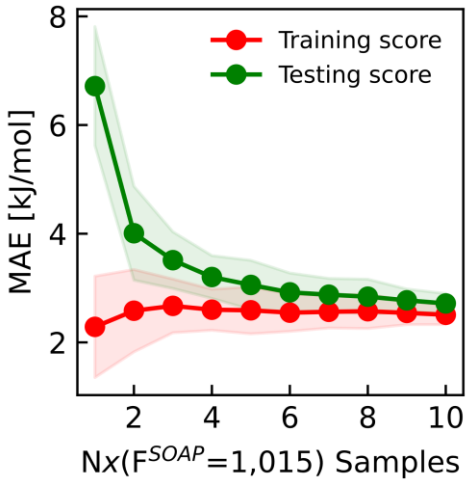

Figure 14: The mean absolute error of the high-fidelity model for the Al(Mg) system as a function of number of training datapoints per SOAP features (N x F^{SOAP}). The shaded region is the standard deviation for 50 repetitions of the 50/50 train/test holdout method used to train the high-fidelity model. The plot validates the 10 points per predictor rule of thumb, as it shows the learning model to converge to a low variance and low bias model with $10xF^{SOAP}$ datapoints.

The product of the first step of the ML framework, feature extraction, is a feature matrix of size (N^{GB} atoms x F^{SOAP} features), which is used as the input to the second step, the learning algorithm, which learns to map the input SOAP features to the target property (segregation energy). For the learning algorithm, we use linear regression for three reasons: first, it is a simple inexpensive model to train and use for predictions; second, it can be automated as it does not require any hyperparameter optimization; and third, it inherently ensures regularization (i.e. is less prone to overfitting) – by simply using a sample size of $>10xF^{SOAP}$ GB sites (following the "one in ten" rule of thumb [95], which we further validate in Figure 14) to fit the F+1 coefficients of the model (F coefficients + intercept), we guard against model overfitting, and selection bias towards a small subset of the population (randomly sampling as few as ~400 points from an infinite population gives a 95% confidence level and 5% margin of error [96]). We note that although more elaborate learning algorithms could be used, such as support vector machines [93], Gaussian process regression [89] or neural networks [94], our proposed ML framework prioritizes simplicity and minimal input from the user, so that other researchers can adopt it easily. We use this approach to

showcase the utility of using atom-centered descriptors for learning GB site segregation energies, without getting lost in the intricate details of fine-tuning more advanced learning algorithms. We note that though the proposed learning framework focuses on segregation spectra in substitutional alloys, it is extensible in principle to interstitial alloys by defining interstitial sites [97] at the GB and bulk regions.

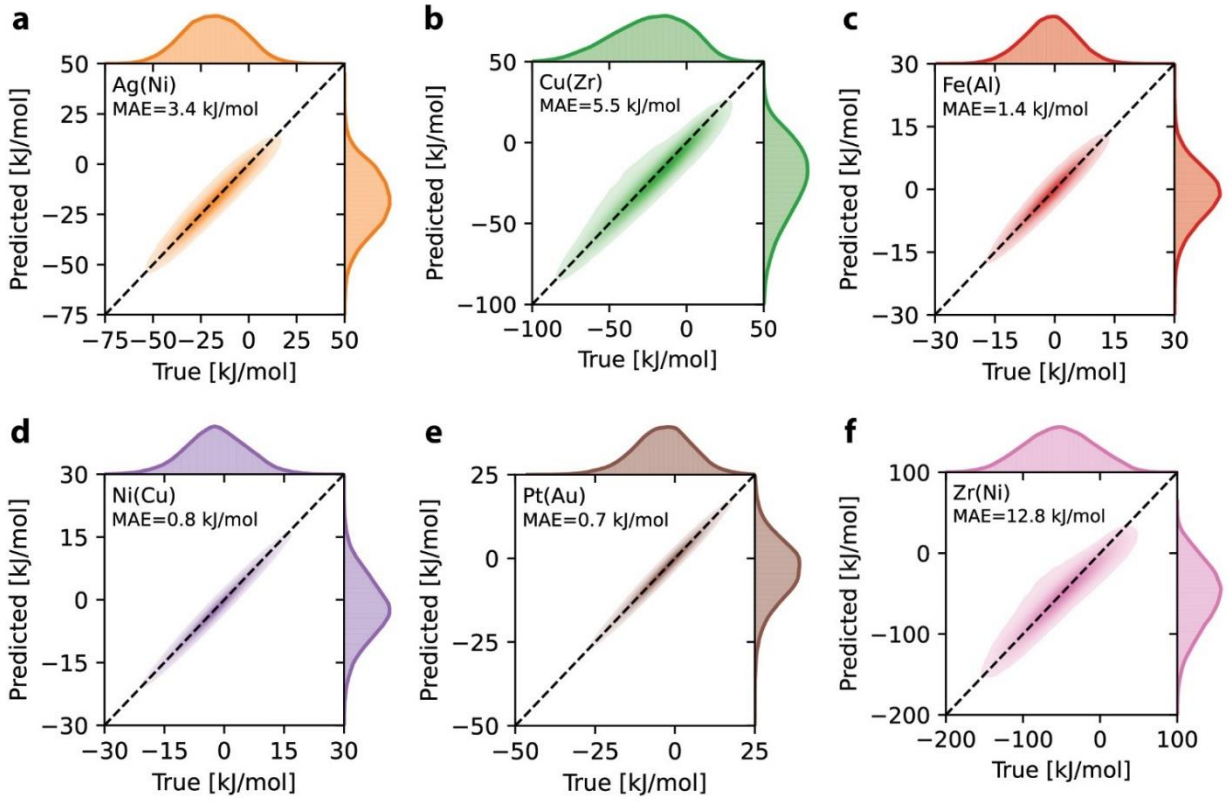

Figure 15: Validation of the high-fidelity ML framework across the alloy space. The predictive performance – mean absolute error (MAE) –of trained ML models, as outlined in Figure 13, for solute segregation in six 20x20x20 nm^3 polycrystalline alloys: **a-f** Ag(Ni) [98], Cu(Zr) [99], Fe(Al) [100], Ni(Cu) [101], Pt(Au) [49], and Zr(Ni) [102].

Using the high-fidelity approach, we train a model, in Figure 13(c), for Mg solute [67] segregation in a thermally annealed 20x20x20 nm^3 Al polycrystal that has 16 grains and ~10^5 GB sites, using a randomized 50/50 split for training/testing. This simple holdout method is easy/cheap to train and use, and its conservative test ratio will guard against a high variance model in most cases. The trained model is highly accurate, with a mean absolute error (MAE) of 2.4(2.5) kJ/mol for the train(test) datasets, respectively, and a root-mean-square error of RMSE=3.8(4.1) kJ/mol. The model faithfully reproduces the distribution of segregation enthalpies in the polycrystal and

has a well-behaved error with normally distributed residuals. This result compares favorably with a more sophisticated ML model by Huber et al. [78], which used 19 structural features (volume, coordination, Voronoi analysis parameters, and Steinhardt bond-order parameters) with gradient boosted decision trees, had a 9-fold cross-validation RMSE=7.7 kJ/mol for Mg solute segregation in a database of 38 low and high-symmetry boundaries in Al. The comparison is not direct, of course, since that work focused on bi-crystals whereas we use polycrystals, but it is also encouraging that the present error is also much lower than the reported error of the interatomic potential as compared to DFT GB segregation energies, which has an RMSE of 8.7 kJ/mol [85].

Table 2: Predictive performance of the high-fidelity model using a) 50/50 training/testing split and b) 5-fold cross validation. The reported errors for the two methods are comparable, which indicates that a simple 50/50 split is sufficient for the model. Also, the low standard deviation (stdv) of error across the 5 folds shows the ability of high-fidelity model to extrapolate well across the GB population.

Solvent(Solute)	**50/50 Training/Testing** train(test) error [kJ/mol]	**5-fold Cross-Validation** mean(stdv) error [kJ/mol]
Ag(Ni)	3.38 (3.49)	3.36 (0.09)
Al(Mg)	2.38 (2.46)	2.45 (0.04)
Cu(Zr)	5.46 (5.62)	5.57 (0.10)
Fe(Al)	1.41 (1.42)	1.29 (0.07)
Ni(Cu)	0.81 (0.82)	0.86 (0.07)
Pt(Au)	0.67 (0.68)	0.69 (0.02)
Zr(Ni)	12.62 (12.96)	12.86 (0.15)

We further validate the efficacy of the high-fidelity ML model for GB solute segregation across the alloy space by training to six more 20x20x20 nm^3 polycrystalline volumes for different alloys: Ag(Ni) [98], Cu(Zr) [99], Fe(Al) [100], Ni(Cu) [101], Pt(Au) [49], and Zr(Ni) [102]. As shown in Figure 15, the ML model accurately reproduces the segregation spectra for the six binary alloys, and has a low MAE typically below ~6 kJ/mol and often below 1 kJ/mol. Alloys with higher absolute values (wider distribution) for the segregation energy will correspondingly have a higher MAE, and the worst of these seen here is MAE = 12.8 kJ/mol for the Zr(Ni) system, but here the segregation spectrum spans about 250 kJ/mol; as a fraction of the total spread of the segregation spectrum, the MAE is uniformly below about 5%. To test the extrapolability of the high-fidelity

framework, we report the mean (and standard deviation) absolute errors using 5-fold cross-validation in Table 2, which shows that the fitted models are able to generalize well to the unseen folds of the dataset (with similar errors as reported in Table 2 for the 50/50 holdout method, and low standard deviation across the folds). We note that although most of the surveyed base-metals have fcc lattice structure, the ML framework seems to be insensitive to the lattice structure, as it similarly performs well for bcc (Fe), and hcp (Zr) metals. Therefore, we conclude that the high-fidelity ML model can be used to accurately model GB segregation across the GB and alloy spaces.

3.2. Accelerated ML Model for GB segregation

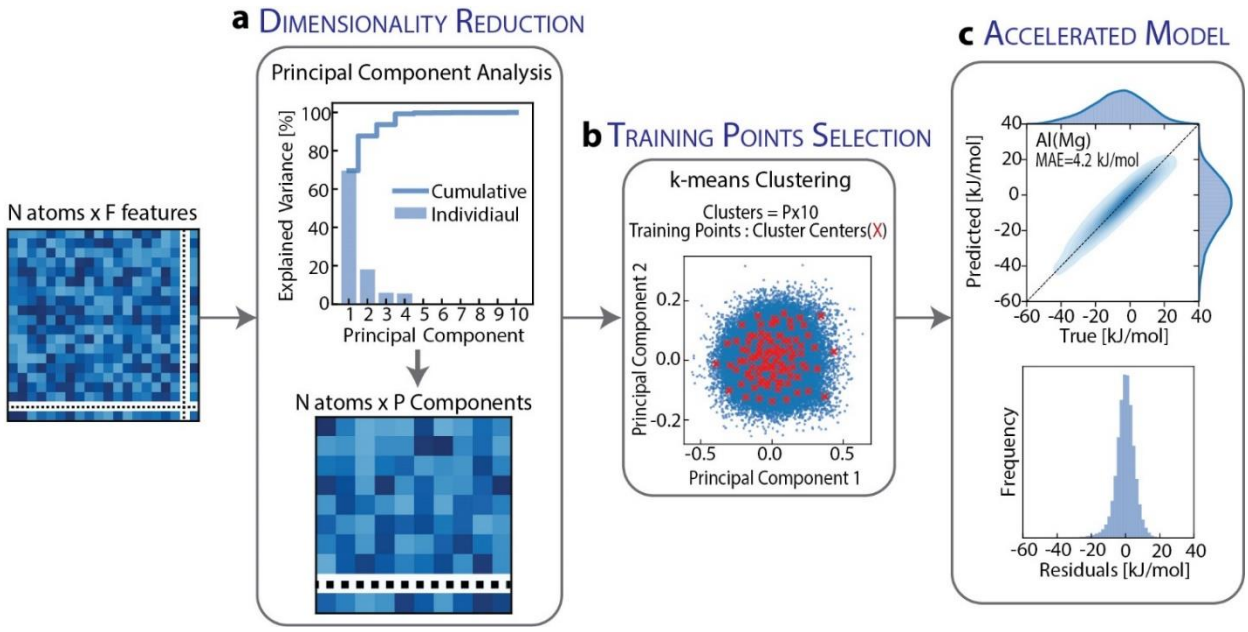

Figure 16: Accelerated ML model for GB segregation. For the Al(Mg) alloy, shown in Figure 13, (a) Principal component analysis is used to reduce the dimensionality of the feature matrix by projecting the F^{SOAP} features into P=10 components that capture >99% of the variance. (b) *k*-means clustering is then used to divide the 10-d transformed feature space into Px10=100 similar clusters; the closest GB sites to the cluster centers (shortest Euclidean distance) are used as training data-points for the learning algorithm (linear regression). (c) Predictive performance – mean absolute error (MAE) – of the accelerated model across the full Al GB network.

In alloy design, it is of interest to be able to quickly scan across the alloy space for interesting combinations. In the context of GB segregation, for example, significant efforts have been conducted to screen for nanocrystalline stabilizing elemental combinations [19,22], complexion forming combinations [103], or GB embrittling solute additions [44,104,105]. Though the high-

fidelity ML model is highly accurate, it still requires ~10^4 data points for training and fitting its ~10^3 coefficients (features). To reduce the training cost and permit a broader scan across the full alloy space, it is appropriate to reduce the dimensions of the input features. We propose the use of unsupervised dimensionality reduction algorithms, which map a high dimensional feature vector into a low-dimensional embedding that captures its main characteristics; "unsupervised" signifies that such mapping is done without a priori knowledge the of the target value (segregation energies). As an illustration, we adopt the simplest of these algorithms, namely principal component analysis[106], which we use to transform the F^{SOAP}=1,015 into 10 principal components (P^{SOAP}) that maximize the captured variance of the feature space. We can think of this process as compressing the 1,015 features into 10 components; such compression captures >99% of the variance of the SOAP feature matrix of the Al polycrystal, as shown in Figure 16.

For an accelerated option of the ML framework, we propose using the 10 principal components obtained from PCA as the input for the linear regression algorithm[107,108]. As the problem is now reduced to fitting P^{SOAP}+1 coefficients (instead of F^{SOAP} + 1), we conservatively only need ~Px10=100 data-points for training; 100 molecular statics computations involving the substitution of a single solute atom at a grain boundary site in a polycrystal give insight on the entire segregation spectrum. As for the selection of the 100 training data points, though random selection can be used, this could be a biased approach due to the low number of points accessing only a prevalent subset of the GB feature space in a given polycrystalline structure. Instead, we propose using *k*-means clustering[109,110] to partition the reduced feature space into *k*=100 clusters that minimize within-cluster variances. The density of cluster centroids aligns with the density of the GB datapoints i.e. more clusters at denser areas of the GB space, as shown in Figure 17(a). We then use the cluster centroids to identify optimal training data-points (i.e., shortest Euclidean distance to the centroids), as shown in Figure 16, for which GB segregation is computed, and use it to train the accelerated model. Such an approach is computationally inexpensive and ensures the full coverage of the feature space in our training dataset.

Similar to the high-fidelity model, the accelerated one can be fully automated and requires minimal input from the user. To compare the performance of both approaches, an accelerated model for Al(Mg), trained with only 100 GB sites, results in an MAE of 4.2 kJ/mol for predictions of the full ~10^5 GB sites, compared to an MAE of 2.5 kJ/mol from the high-fidelity model trained with 50% of GB sites. The error from accelerated model is well behaved across the GB space, as

shown in Figure 17(b), where the model extrapolates well to the extreme points in PC space; this indicates the k-means based sampling does a good job of datapoint selection here. The reduction (two orders of magnitude) in the required training data points, with minimal loss of accuracy, is significant, and showcases the power of the accelerated model to quickly, and accurately, predict the segregation spectra in binary alloys. It also signifies that the full GB space could possibly be reduced to a small number of key GB environments – also known as GB "building blocks" [93] – that decipher the features of the full space. We expect this to be a significant direction of future work in the context of grain boundary segregation.

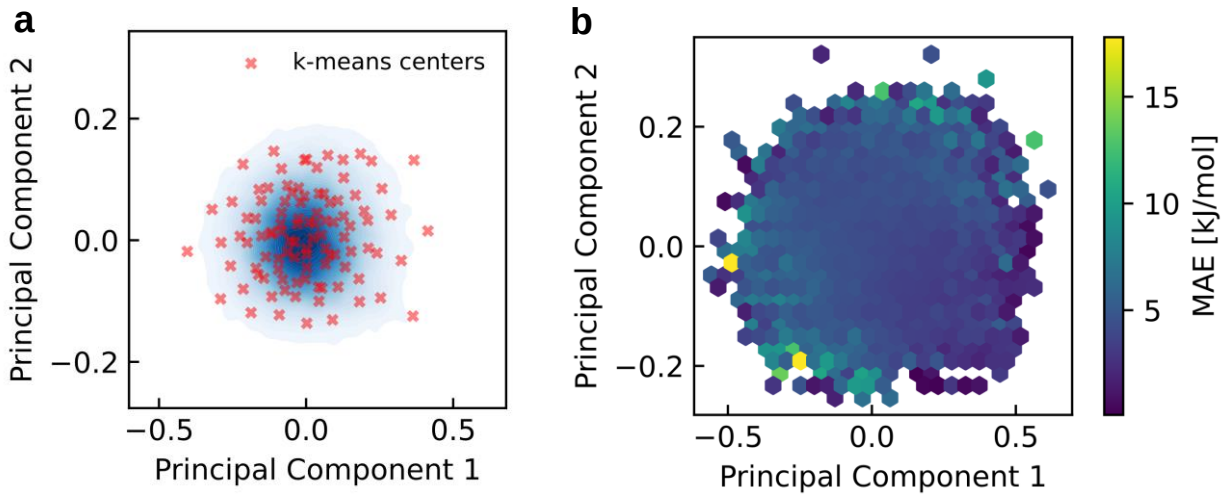

Figure 17: An overview of the accelerated model, outlined in Figure 16, for the Al(Mg) alloy. (a) *k*-means centers plotted over a density-plot of the GB population in PCA space, and (b) a hexbin plot of the MAE across the PCA space.

Using the accelerated approach, we build ML models to predict solute segregation spectra in polycrystals for every aluminum, and magnesium, and transition metal-based binary alloys (Supplementary Figs. 2-20) that have interatomic potentials in the NIST Interatomic Potentials Repository – a total of 259 alloys (see Supplementary Fig. 1). This segregation database not only allows us to screen the alloy space for segregation "hot-spots" or regions of interest, but also to compare the variation of the spectrum with different interatomic potentials (for alloys where more than one potential exists). To illustrate the utility of the database, we plot in Figure 18 all solute segregation spectra in a nickel-based alloy; Ni(Ag) [98] is predicted to be highly segregating, and the opposite for Ni(Al) [111].

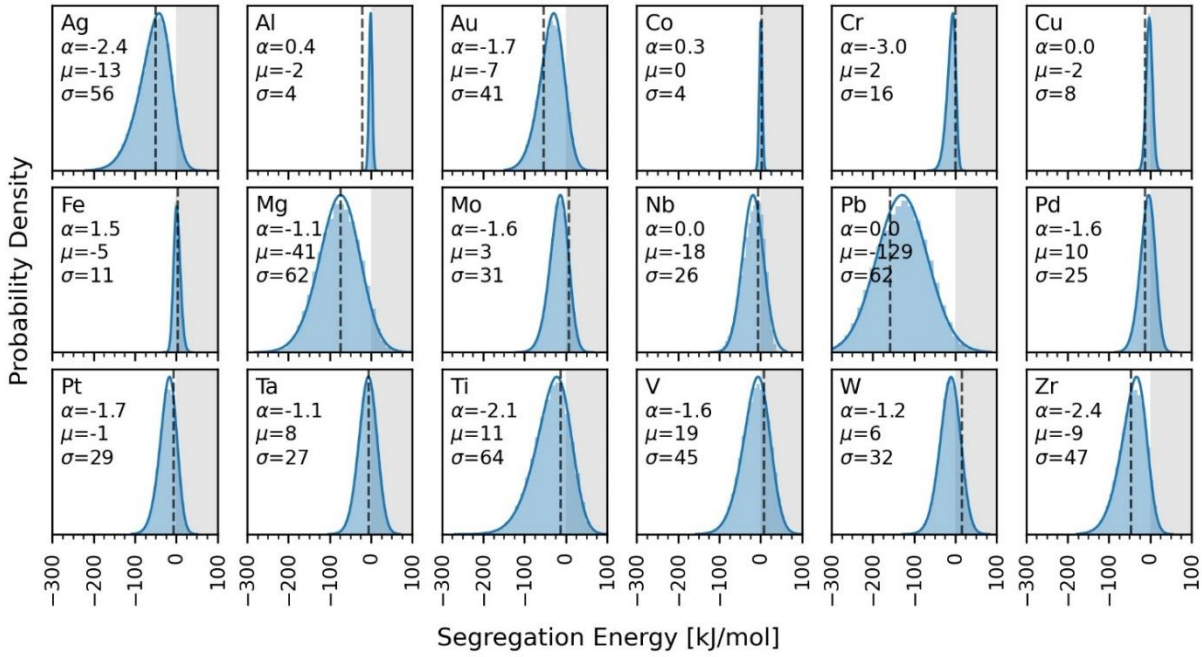

Figure 18: GB segregation spectra in Ni-based alloys. Using the accelerated ML model outlined in Figure 16, we compute GB segregation energy spectra for 18 solutes [98,101,102,111–119] in a 20x20x20 nm^3 Ni polycrystal of grain size 10 nm; the anti-segregation region ($\Delta E_i^{seg} > 0$) is shaded. The spectra are fitted to the skew-normal function Eq. (19)(solid line), and the value of the characteristic energy μ (kJ/mol), width σ (kJ/mol), and shape α of the function are listed. Also, the spectra are compared to the "average" segregation energy (dashed vertical line) used to charecterize these alloys in the database of Murdoch and Schuh [120].

3.3. Spectral Segregation Database

There are three key findings to the spectral segregation database (Figure 18 and Supplementary Figs. 2-20). The first is that all segregation spectra in all binary alloys surveyed, as hypothesized earlier in our study of the Al(Mg) system [82], are captured well by a skew-normal function (the fitted probability density function has an $R^2 > 0.95$ in all but one alloy with an R^2=0.80; see Supplementary Figs. 2-20). This function involves three parameters – the characteristic energy μ, width σ and shape α of the distribution:

$$F_i^{gb}(\Delta E_i^{seg}) = \frac{1}{\sqrt{2\pi}\,\sigma}\exp\left[-\frac{\left(\Delta E_i^{seg}-\mu\right)^2}{2\sigma^2}\right]\mathrm{erfc}\left[-\frac{\alpha\left(\Delta E_i^{seg}-\mu\right)}{\sqrt{2}\,\sigma}\right] \qquad (20)$$

These parameters are provided in the corresponding figure for each alloy considered. The second key finding is that using a McLean "average" [30] segregation energy to characterize a binary

alloy, which is the segregation literature norm [36,120], misses key information about the accessible segregation states at the GB network. For example, the Ni(Ag) system that has a reported "average" segregation energy of -50 kJ/mol [120], has approximately 15% of its GB network with segregation energies more than twice that, below -100 kJ/mol, as shown in the first panel of Figure 18. GB segregation occurs first in the lowest energy states, and before a grain boundary in Ni(Ag) would experience the McLean average segregation energy, it would lie at an extremely high composition of approximately 50 at% Ag. The knowledge of the full spectrum is thus essential to enable the design of microstructures [121] that maximize the desired tail of the segregation spectrum (i.e. either promote or inhibit segregation). The third key finding is that, for alloys with more than one available interatomic potential, the computed segregation spectra can be sensitive to the choice of the potential. For example, potentials for the Al(Ni) system produce completely different segregation spectra, as shown in Supplementary Fig. 3, which range from having almost all GB sites being unfavorable to segregation [118] to the complete opposite[122]; such variation can result in an order of magnitude difference in predictions for GB solute concentration even at low total solute concentrations in the system (see Supplementary Fig. 23). Further work is needed in the future to quantify the accuracy of such potentials for GB segregation studies [123], and as always with atomistic models, it is important to remember that the present framework will only return physically reasonable results if the potential is specifically suitable for the problem at hand. For now, we report all of them, and leave the selection step to the judgment of the user.

Though the analysis in Figs 1-3 shows that the ML models faithfully reproduce most of the details of the GB segregation spectrum, this is not the most critical test for their practical viability; these models are only useful to the extent that they correctly capture GB segregation in some realistic situation. Thus, the most important metric is the prediction for the equilibrium GB segregation state (i.e. extent of segregation). For a spectrum of segregation energies at the GB network, the equilibrium solute distribution among the different sites follows Fermi-Dirac statistics [37,39,82]. In a closed system with finite grain sizes, the total solute concentration X^{tot} is fixed and shared by the bulk (intra-grain) and GB solute concentrations, X^c and $\bar{X}^{gb}$, respectively, according to the GB site fraction f^{gb}:

$$X^{tot} = (1 - f^{gb})X^c + f^{gb}\bar{X}^{gb} \tag{21}$$

The equilibrium X^c and $\bar{X}^{gb}$ are a function of the temperature T, the distribution of GB segregation energies $F_i^{gb}(\Delta E_i^{seg})$, and are obtained by numerically solving for X^c that satisfies the expanded form of Eq. (21) [82]:

$$X^{tot} = (1 - f^{gb})X^c + f^{gb} \sum_i F_i^{gb} \left[1 + \frac{1 - X^c}{X^c} \exp\left(\frac{\Delta E_i^{seg}}{kT}\right)\right]^{-1} \tag{22}$$

In Figure 19, we compare the equilibrium GB segregation state obtained using the true computed spectrum versus the ML predicted ones with both high-fidelity and accelerated models, for all seven alloys from Figure 13 and Figure 15, in a polycrystal of average grain size 15 nm (f^{gb} ≈10%) at T = 600 K. The predictions of the ML models closely match those of the true spectrum, indicating that the ML models capture the necessary information to correctly predict the equilibrium segregation state. Also, as briefly discussed earlier, though the value of the MAE differs from one system to another, a higher MAE does not necessarily translate to a worse result, when one normalizes to the scale of the segregation energy distribution, e.g. the Zr(Ni) system in Figure 19. Finally, we note that the difference (deviation) in predictions of the equilibrium segregation state could be even less of an issue if the skew-normal approximation Eq. (19) is used, instead of the full discrete spectra, to quantify GB segregation using the continuous form of the segregation isotherm Eq. (9) [82]:

$$X^{tot} = (1 - f^{gb})X^c + f^{gb} \int_{-\infty}^{\infty} F_i^{gb} \left[1 + \frac{1 - X^c}{X^c} \exp\left(\frac{\Delta E_i^{seg}}{kT}\right)\right]^{-1} d\Delta E_i^{seg} \tag{23}$$

as the three fitted parameters (μ, σ, and α) of the skew-normal function for the true and ML predicted spectra should closely match, even for systems with high MAE, as the residuals are well-behaved and normally distributed (with a zero mean, as shown in Figure 13 and Figure 16).

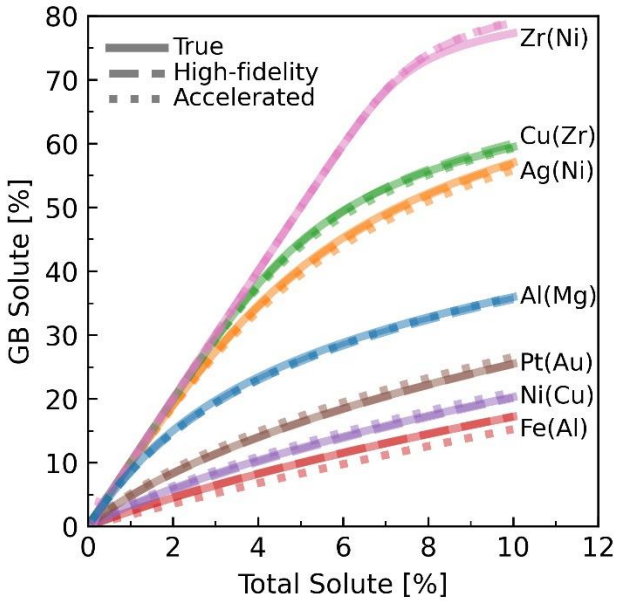

Figure 19: Predictions of the equilibrium segregation state. Predictions of equilibrium $\bar{X}^{gb}$ using the true, and predicted (from both high-fidelity and accelerated ML models) segregation spectra for seven polycrystalline alloys with an average grain size of 15nm at T= 600 K.

To motivate further analysis of the spectral segregation database, and visually summarize the segregation tendency across the alloy space, we plot a two-dimensional Pettifor [124] map in Figure 20 (for most alloys in the database) using the 25th percentile value (energy) for the segregation spectra (i.e. 25% of GB sites have lower segregation energies). As the lower tail is the most enthalpically favorable, it will disproportionately influence the segregation tendency in any given alloy, especially at low or dilute solute concentration. The choice of the Pettifor chemical scale (which preserves the Mendeleev-type features of the elements [124]) is based on its success in pattern clustering (separation) for miscibility [125], ordering tendency [126,127], and crystal structures of intermetallics [124] in binary alloys. Though Figure 20 shows some clustering, it is not enough to draw concrete conclusions on the segregation tendency across the alloy space; the same finding applies to another two routinely used parameters to characterize the chemical and physical nature of the elements – electronegativity [128], and metallic radius [129] – (see Supplementary Figs. 24-27). It is evident that more effort is needed to formulate (or extract from ML) simple phenomenological parameters (preferably derived from atomic features e.g. Miedema-

style parameters [130]) that better explain these trends. We hope that this preliminary exploration of the data will promote further work on this front.

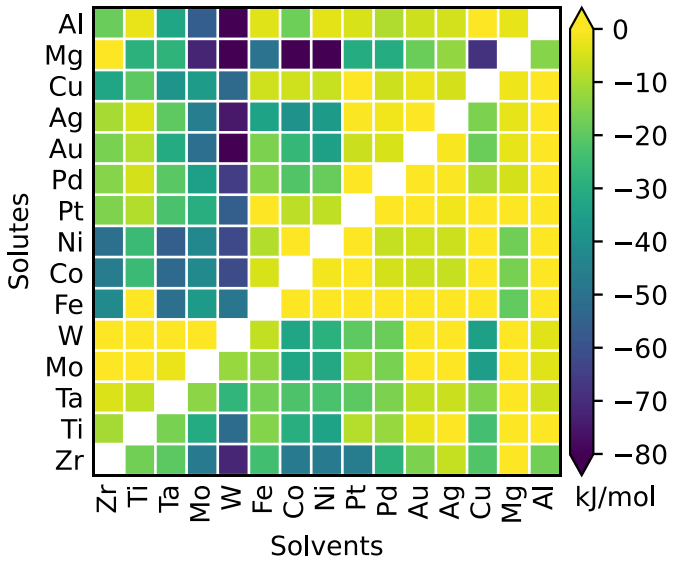

Figure 20: Visual summary of the predicted segregation tendency across the alloy space. The value of the first quartile of the segregation spectra (i.e. 25% of GB sites have lower segregation energies) as predicted using the accelerated model for 225 alloys (we removed columns with empty entries for compact viewing); the elements are arranged by their order on the Pettifor chemical scale [124]. For alloys with multiple interatomic potentials (see Supplementary Fig. 1), we report the least segregating spectra as a conservative choice (see Supplementary Fig. 25 for an alternative version of the figure with the most segregating spectra).

3.4. Computational Methods

3.4.1. GB segregation enthalpies

The atomistic simulation package LAMMPS [66,131] is used for all molecular statics and dynamics simulations; OVITO [73] is used for visualization and identification of atomic structures.

To generate the base-metal polycrystal, we fill a 20x20x20 nm^3 volume with 16 randomly oriented grains using Voronoi tessellations with Atomsk [69]. The polycrystal is thermally annealed at 0.3-0.5 of the melting temperature under a Nose-Hoover thermostat/barostat for 250 ps using a time step of 1 fs, which relaxes the grain structure and boundaries without permitting exaggerated grain growth; this is followed by slow cooling to 0 K at a cooling rate of 3 K/ps, and a final conjugate gradient energy minimization.

To compute the spectrum of segregation enthalpies in a binary alloy, we follow the procedure in Ref. [82]. We first relax the base-metal polycrystal using the interatomic potential of that alloy, by applying an external pressure of zero in a conjugate gradient minimization, followed by a second conjugate gradient minimization (with no applied pressure). This is necessary to scale the cell, and correct for minor differences in the equilibrium lattice parameter of the base-metal across the different interatomic potentials (for example, the Ni polycrystal is thermally annealed using an interatomic potential [102] that is fitted to Ni lattice parameter of 3.518 Å, but the Ni(Al) [111] is fitted to 3.520 Å). Then, every GB site in the annealed polycrystal is identified using adaptive-common neighbor analysis method [74]; all atoms that have a different atomic structure than the base metal are assumed to be GB atoms. For every GB site (*i*), its ΔE_i^{seg} is calculated as the relaxed energy difference between the solute atom occupying the GB site, versus a bulk (intra-grain) site: $\Delta E_i^{seg} = E_{gb,i}^{solute} - E_c^{solute}$; the relaxation of each state is achieved using a conjugate gradient minimization, and the reference bulk site for E_c^{solute} is chosen as the center of a 6 nm sphere of the pure solvent (in the polycrystal), to avoid any long-range interactions with GB atoms. All calculations are at 0 K, isolating the enthalpic portion of the segregation energy for each site.

3.4.2. Machine Learning

For feature extraction, the LAE of every GB site within a cutoff radius of 6 Å is described using the SOAP method, as implemented in the QUIP/GAP software package [89,91]. SOAP fits a set of radial basis functions and spherical harmonics to Gaussian particle density functions placed over all neighboring atoms in the LAE. The maximum number of radial basis functions (n_{max}), degree of spherical harmonics (l_{max}), and the width of Gaussian functions (σ_{at}) control the size and resolution of the SOAP feature vector. We use $n_{max} = l_{max} = 12$ and $\sigma_{at} = 1$ Å for all alloys, which gives a SOAP vector with 1,015 features. As for the other components of the ML framework: linear regression, principal component analysis, and *k*-means clustering are used as implemented in the Scikit-learn [132] python package.

3.4.3. Data and Code Availability

The database for segregation spectra of all 250+ binary alloys, in the form of LAMMPS text dump files of solvent polycrystals with predicted GB solute segregation energies, and an example

Jupyter Notebook with all necessary code to train and use the high-fidelity and accelerated machine learning models are available at https://doi.org/10.5281/zenodo.4107058.

3.5. Conclusion

In summary, our proposed ML framework, inspired by methods developed for fitting ML-based interatomic potentials, aims to fit a "pseudo interatomic potential" for GB segregation energies in polycrystalline alloys. The framework is designed to require minimal input from the user, and as such, is automatable. As the ML literature is constantly evolving, we look forward to new developments and tools that can further improve the framework. We offered two model options. The first is a high-fidelity model that uses a large SOAP vector ($>10^3$ features), a conservative radial cutoff (6Å), and linear regression. The second, is an accelerated model that uses PCA to transform the original features into a few (10) principal components (which are then used as input features to linear regression); this reduces the dimension of the learning problem to just 100 key GB environments, which are selected by k-means clustering to ensure coverage of the GB space. The accelerated model is used to build an extensive database for segregation spectra in 259 binary alloys, which is included the appendix. We look forward to applications of this database in alloy design, and hope it motivates more widespread use of spectral approaches to GB segregation in polycrystalline materials.

4. THERMODYNAMICS AND DESIGN OF NANOCRYSTALLINE ALLOYS USING GRAIN BOUNDARY SEGREGATION SPECTRA

In Chapter 2, we used atomistic simulations to show that, for polycrystals, the spectrum of GB site-types and their segregation energies are well captured by a skew-normal distribution function, and briefly discussed the implications of such a spectrum upon the stability criteria for a nanocrystalline alloy. And, subsequently, in Chapter 3, we used a machine-learning based framework to compute the segregation spectra for over 200 binary alloys, which were all similarly well captured by a skew-normal distribution function. In this Chapter, we take the next step, and showcase the implications of our findings to alloy design. We apply the spectral framework to the problem of designing and screening for nanocrystalline alloy stability.

In pure metals, a nanocrystalline structure, which is generally defined as a polycrystal with a grain size of 100 nm or less, can have a multitude of desirable material properties unattainable otherwise for structures with larger grain sizes [19,133–137]. However, such structures are inherently thermodynamically unstable; a nanocrystalline configuration comes with a large volume fraction of high-energy bearing defects (grain boundaries) that introduces a large excess of energy in the structure (on the order of ~1-10 kJ/mol depending on grain size). In fact, the driving force to reduce its energy can, in some cases, be strong enough to induce grain growth at room temperature [138,139] (and hence the loss of nanocrystallinity and its accompanying desirable material properties).

In 1993, Weissmüller outlined a thermodynamic framework to stabilize nanocrystalline structures through *alloying* [18]. The key concept is that, in an alloy, if solute atoms prefer the grain boundary (GB) environment over the crystalline bulk (intragranular region), a polycrystalline alloy can reduce its energy through solute segregation at the GB. If the energetic benefit from solute segregation is equal to (or larger than) the energetic penalty of having the GB network (necessary to accommodate the solutes), then a solute-segregated nanocrystalline structure can be thermodynamically favorable, and as such, is stable against grain growth. In effect, this translates to a thermodynamic stability criterion that can be used to screen binary alloys for nanocrystalline stability. Subsequent stability criteria have built on the Weissmüller concept [26,140–144] by

incorporating, e.g., energetic competition from phase separation [142] or ordered compound formation [26].

Unfortunately, all the developed stability criteria (and associated alloy screening efforts) for nanocrystalline alloys applied to date have used a simplified representation of GBs, treating the entire GB network as a single entity, with a single site-type available for segregation. Screening is thus conducted on a scalar such as the "average" GB segregation enthalpy, $\Delta\bar{H}^{seg}$. However, this is a substantial oversimplification that misses key physics of GB segregation; GBs are well known to be highly anisotropic [145], and have a variety of site-types (i) that accommodate solute atoms to different degrees, which results in a distribution of segregation enthalpies, ΔH_i^{seg} [34,36,146,37–40,42,78,82,100]. We note that, in solids, the segregation enthalpy is equivalent to the segregation internal energy [46], $\Delta H_i^{seg} \approx \Delta E_i^{seg}$, which can be readily calculated using atomistic simulations at 0 K; throughout the chapter, we therefore use the terms "energy" and "enthalpy" interchangeably.

In this spectral representation of GB segregation, the enthalpic benefit of segregation is not the averaged quantity $\Delta\bar{H}^{seg}$ anymore, but is the cumulative benefit of solute segregation to all favorable GB site-types with $\Delta H_i^{seg} < 0$ (in this notation, a favorable GB site has a negative segregation energy, such that the system reduces its energy by ΔH_i^{seg} upon solute segregation). In this chapter, we address the limitation of using an "averaged" representation of GBs, and develop a thermodynamic framework to screen for nanocrystalline stability, which takes into account the spectral nature of GBs. We develop enthalpic stability and metastability criteria for a nanocrystalline alloy in the spectral representation, and subsequently use it to screen over 200 binary alloys for viable candidates that can form stable (and metastable) nanocrystalline structures.

4.1. Spectral Enthalpic Stability Criteria for Nanocrystalline Alloys

4.1.1. Stability of a polycrystal with respect to a solid solution

For a polycrystalline alloy with N^{gb} GB atomic sites, the dilute-limit segregation energy of a solute atom at site-type (i) is:

$$\Delta E_i^{seg} = E_{gb,i}^{solute} - E_{c(sln)}^{solute} \tag{24}$$

where $E_{gb,i}^{solute}$, $E_{c(sln)}^{solute}$ are the relaxed total energy of the polycrystal with a solute atom at GB site-type (*i*), and a crystalline bulk site (intragranular), respectively. While this expression incorporates the conventional reference state for GB segregation, i.e. the solid solution state (denoted by "sln" in the subscript), this state is metastable by nature at 0 K, and is never the ground state configuration for a metal alloy with a nonzero heat of mixing; at 0 K, an alloy with a positive mixing enthalpy should phase separate (demix), and one with a negative mixing enthalpy should form an intermetallic compound. Therefore, the computed ΔE_i^{seg} from Eq. (24) can be used only to establish a criterion for nanocrystalline *metastability* i.e. enthalpic stability with respect to a solid solution:

$$\sum_{\Delta E_i^{seg}=-\infty}^{0} N_i^{gb} \cdot \Delta E_i^{seg} < -\sum_{\Delta E_i^{seg}=-\infty}^{\infty} \sum_{j=0}^{N_i^{gb}} \Delta E_{i,j}^{xs} \tag{25}$$

where N_i^{gb} is the number of GB sites of type (*i*), and $\Delta E_{i,j}^{xs}$ is the excess energy of GB site (*j*), type (i). We stress here that the subscript "*j*" denotes a single GB site (*j*), and that the subscript "*i*" denotes GB site-type (i), which encompasses all GB sites with the same segregation energy ΔE_i^{seg}. Simply, the left-hand side of Eq. (25) is the maximum enthalpic benefit that can come from solute segregation to all favorable GB sites ($\Delta E_i^{seg} \leq 0$), and the right-hand side is the enthalpic benefit of removing the GB network (N^{gb} GB atomic sites with excess energy of ΔE_j^{xs} per site). For stability analysis, we are concerned with the total enthalpic cost of the whole GB network, rather than the underlying distribution of excess energies $\Delta E_{i,j}^{xs}$ (though a precise treatment should capture it). The spectrality of the GB environments is still fully captured by the left-hand side i.e. the whole system reduces its energy by ΔE_i^{seg} upon solute segregation to site-type (*i*), regardless of the coordinates of the GB site itself (*i*,*j*) or its excess energy $\Delta E_{i,j}^{xs}$. We can thus simplify the right-hand side of Eq. (25) by evaluating the summations to give $N^{gb} k_\gamma \gamma$, where γ is the average GB energy of the polycrystal (per unit area, as traditionally defined), and k_γ is a constant to convert the GB energy to a per-atom quantity and thus incorporates a grain boundary thickness. In practice, we directly compute the full GB energy directly over all sites in a computational structure as suggested by the double summation in Eq. (25). Making this substitution and dividing Eq. (25) by N^{gb} to express it in terms of a discrete distribution function, we obtain:

$$\sum_{\Delta E_i^{seg} = -\infty}^{0} F_i^{gb} \cdot \Delta E_i^{seg} < -k_\gamma \gamma \tag{26}$$

where $F_i^{gb} = N_i^{GB}/N^{GB}$ is the distribution function: the fraction of site-type (i) in the GB network (i.e., $\sum F_i^{gb} = 1$). Recasting Eq. (26) in terms of a continuous distribution function, we have:

$$\int_{\Delta E_i^{seg} = -\infty}^{0} F_i^{gb} \cdot \Delta E_i^{seg} \; d(\Delta E_i^{seg}) < -k_\gamma \gamma \tag{27}$$

For screening purposes, it is more convenient to express Eq. (27) in terms of a metastability score Φ^M, with the condition for enthalpic stability against a solid solution being $\Phi^M \geq 1$:

$$\Phi^M = \frac{1}{-k_\gamma \gamma} \int_{\Delta E_i^{seg} = -\infty}^{0} F_i^{gb} \cdot \Delta E_i^{seg} \; d(\Delta E_i^{seg}) \tag{28}$$

It is important to emphasize again that owing to the reference state in these equations being a solid solution, the criterion of Eq. (27) and the ranking metric of Eq. (28) represent only the stability of a polycrystalline or nanocrystalline state against the competing solid solution phase. While this is exactly the original competition envisioned by Weissmuller [18], it is formally only a *metastability* criterion in the global sense, because the solid solution reference state is not a ground state, but gives way at zero Kelvin to more stable configurations (second phases).

4.1.2. Stability of a polycrystal with respect to competing ground state phases

Looking beyond metastability to a hypothetical enthalpic stability condition, we need to compare the energy of a solute-segregated nanocrystalline state against that of the most stable (bulk) state for the alloy at 0 K, which involves the terminal solute phase and either an intermetallic compound or a second terminal phase. In such cases, the enthalpic benefit from segregation to site-type (i) is not ΔE_i^{seg} anymore, as defined by Eq. (24), but should be redefined ($\Delta E_{i,eq}^{seg}$) to quantify the enthalpic benefit of a solute atom leaving the competing bulk ground state ($E_{c(eq)}^{solute}$ at 0 K) to a GB site-type (i):

$$\Delta E_{i,eq}^{seg} = E_{gb,i}^{solute} - E_{c(eq)}^{solute} \tag{29a}$$

$$\Delta E_{i,eq}^{seg} = \Delta E_i^{seg} - \Delta E_{ref=sln}^{solute} \tag{29b}$$

Eqs. (29a) and (29b) are equivalent, with Eq. (29a) used to present a parallel with the traditional definition of segregation energies in Eq. (24), and Eq. (29b) explicitly showing the shift in the reference frame in a single quantity $\Delta E_{ref=sln}^{solute}$. This quantity is the energy difference between embedding a solute atom into the new reference state of a bulk equilibrium configuration $E_{c(eq)}^{solute}$, and a solid solution ($E_{c(sln)}^{solute}$, the reference state for Eq. (24)); this is illustrated in Figure 21, and will be discussed in more detail below. We note that in an earlier publication we presented a schematic discussion of these ideas in which this shift in reference state was missing [82]. The present correction is certainly necessary for thermodynamic consistency when performing quantitative calculations as we are about to in what follows.

Accounting for this energetic shift in the reference state, we derive, in a similar fashion to Eq. (27) (and as detailed in Supplementary Section 2 of Ref [147]), the criterion for nanocrystalline *ground state stability* i.e. enthalpic stability with respect to the alloy ground state at 0 K:

$$\int_{\Delta E_i^{seg} = -\infty}^{\Delta E_{ref=sln}^{solute}} F_i^{gb} \cdot (\Delta E_i^{seg} - \Delta E_{ref=sln}^{solute})\ d(\Delta E_i^{seg}) < -k_\gamma \gamma \tag{30}$$

We similarly recast Eq. (30), for screening purposes, in terms of a stability score Φ^S, with the condition for nanocrystalline ground state stability being $\Phi^S \geq 1$:

$$\Phi^S = \frac{1}{-k_\gamma \gamma} \int_{\Delta E_i^{seg} = -\infty}^{\Delta E_{ref=sln}^{solute}} F_i^{gb} \cdot (\Delta E_i^{seg} - \Delta E_{ref=sln}^{solute})\ d(\Delta E_i^{seg}) \tag{31}$$

Eqs. (30) and (31) have the same form as Eqs. (27) and (28), respectively, for stability against the solid solution, but instead use the modified segregation energy ($\Delta E_i^{seg} - \Delta E_{ref=sln}^{solute}$) in the integrand, which in turn, changes the upper limit of the integral to $\Delta E_{ref=sln}^{solute}$; the upper bound of energetically favorable GB sites is now defined by $\Delta E_i^{seg} - \Delta E_{ref=sln}^{solute} \leq 0$, as shown schematically in Figure 21. Therefore, the key difference in Eqs. (30) and (31) is the quantity $\Delta E_{ref=sln}^{solute}$, the energy of removing a solute atom from a solid solution, and placing it into a bulk equilibrium configuration. Since equilibrium at T = 0 K involves pure phases and line compounds,

a new solute addition effectively samples a tie-line between the equilibrium phases, in this case, the terminal solvent phase and the nearest second phase. The result for a binary alloy has the generalized form (derived in the Supplementary Section 2 of Ref [147]):

$$\Delta E_{ref=sln}^{solute} = \frac{1}{x_s^c}\Delta E_{ord}^{form} - \Delta E_{sol}^{B\ in\ A} \tag{32}$$

where $\Delta E_{sol}^{B\ in\ A}$ is the energy of embedding one solute atom (B) into the equilibrium lattice matrix of solvent (A), and, for compound forming alloys, ΔE_{ord}^{form} is the formation energy (at 0 K) of the intermetallic compound with the lowest stoichiometry x_s^c; both quantities can be obtained from atomistic simulations (at 0 K) as detailed in the following section. Eq. (32) should reduce to $(-\Delta E_{sol}^{B\ in\ A})$ in non-compound forming systems, which occurs by setting $\Delta E_{ord}^{form} = 0$. We note that $\Delta E_{ref=sln}^{solute}$ should be less than zero ($\Delta E_{ref=sln}^{solute} < 0$), as a positive value means that it is more enthalpically favorable for a solute atom to exist in a solid solution, over the predicted 0 K ground state (lying on a tie-line between the solvent phase and the nearest compound) – this is never the case enthalpically.

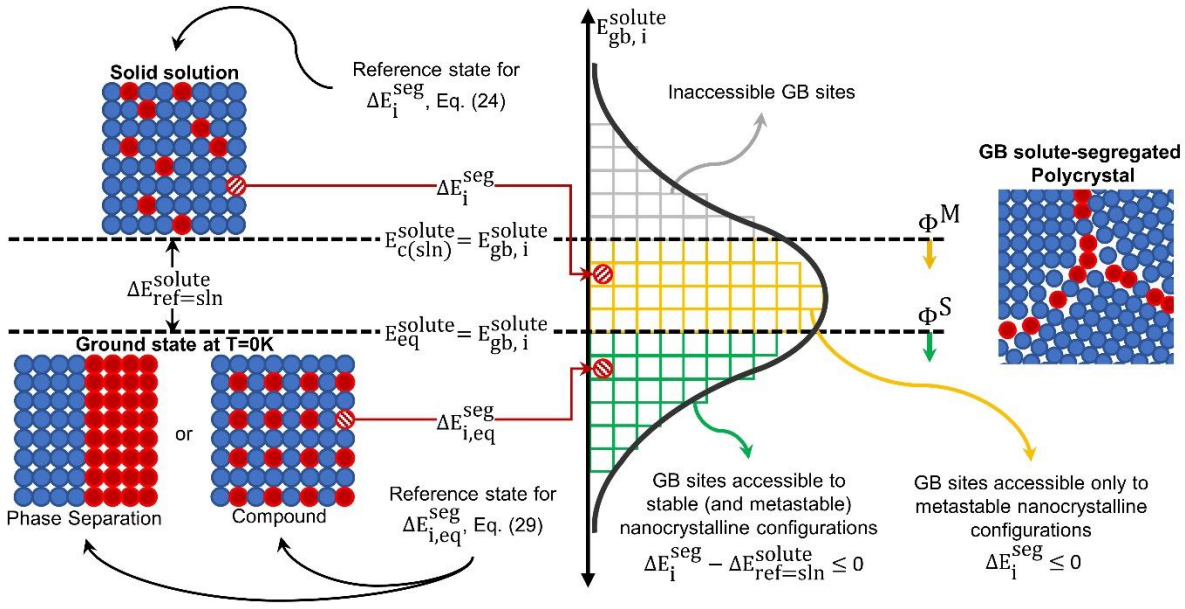

Figure 21: An illustration of the effect of changing the reference state for the solute (i.e. in a solid solution versus the ground state at T=0K) on the (calculated) energetics of solute segregation at GBs, and subsequently, the enthalpic favorability for the different GB site-types.

4.1.3. Functional form of the grain boundary segregation energy

The proposed screening framework (outlined by Eqs. (28) and (31)), being strictly enthalpic, enables high-throughput evaluation of alloy candidates using quantities that can be computed from atomistic simulations at 0 K. Among these is the spectrum of grain boundary segregation energies, which we have addressed in several prior papers [82,146,148]. In those works, we have shown that the full distribution F_i^{gb} can be computed rigorously [82] or approximated with regression models [148]. More importantly, we have shown that to a very good approximation, an exhaustive list of hundreds of thousands of ΔE_i^{seg} values can be condensed into an accurate analytical form requiring only three parameters to characterize the distribution. Taking a skew-normal distribution function for polycrystals – based on our findings in [82,148] – three fitted parameters are required to characterize the distribution function, F_i^{gb} – the characteristic energy μ, the width σ, and the shape α:

$$F_i^{gb} = \frac{1}{\sqrt{2\pi}\,\sigma} \exp\left[-\frac{\left(\Delta E_i^{seg} - \mu\right)^2}{2\sigma^2}\right] \operatorname{erfc}\left[-\frac{\alpha \cdot \left(\Delta E_i^{seg} - \mu\right)}{\sqrt{2}\,\sigma}\right] \tag{33}$$

This expression, when introduced into Eqs. (28) or (31), completes the framework for screening alloys, which are now parameterized by their phase energies along with grain boundary segregation parameters μ, σ, and α. Our approach is similar in spirit to the use of density-functional theory calculations to screen (and search for) materials and develop 0 K phase diagrams [149–152], but is now inclusive of a realistic grain boundary segregation spectrum. Clearly, a comprehensive assessment of candidate alloys should include entropic contributions [153] and state parameters (such as composition, temperature, and grain size), to identify viable temperature-composition domains of nanocrystalline stability. Such developments are more rigorously possible with the present baseline in place, and since these analyses are more resource-intensive, can be reserved for post-screening candidates from the present enthalpic approach. This is the subject of some of our future work.

4.2. Atomistic Computational Methods

We use Eqs. (28) and (31) to calculate the nanocrystalline metastability Φ^M and ground state stability Φ^S scores, respectively, for binary alloys of 15 metals: Ag, Al, Au, Co, Cu, Fe, Mg, Mo,

Ni, Pd, Pt, Ta, Ti, W, and Zr – a total of 210 alloys. As detailed in Section 4.1, we need five parameters for each phase separating pair, and seven parameters for each compound forming pair, in order to compute Φ^M and Φ^S. These include the GB segregation skew-normal distribution parameters (α, μ, σ), the excess energy per GB atom $k_\gamma\gamma$, the dilute energy of mixing per solute atom $\Delta E_{sol}^{B\ in\ A}$, and for compound-forming systems, the formation energy ΔE_{ord}^{form} of the competing intermetallic compound and its stoichiometry x_s^c.

We obtain (α, μ, σ) from our earlier work in Ref [148], in which a machine-learning based framework was used to compute the distribution of GB segregation energies in thermally annealed 20x20x20 nm^3 polycrystals of the base metals. That analysis used all available interatomic potentials of the embedded atom method (EAM) type [154] and its variants in the interatomic repository [83,84] of the National Institute of Standards and Technology. For more details on the learning framework, and the simulation methodology, we refer the reader to Ref [148]. To make the stability and metastability scores calculations self-consistent, for every set of (α, μ, σ), we use the same interatomic potential employed earlier in Ref [148] to also compute $k_\gamma\gamma$, $\Delta E_{sol}^{B\ in\ A}$, and ΔE_{ord}^{form}. The atomistic simulation package LAMMPS [66,131] is used to perform all molecular statics and dynamics simulations, and OVITO [73] is used to visualize and identify atomic structures.

For each base metal, we use molecular statics to compute $k_\gamma\gamma$ for the (20 nm)^3 polycrystals from Ref [148]:

$$k_\gamma\gamma = \frac{1}{f^{gb}} \cdot (\mathrm{E}^{\mathrm{poly}} - \mathrm{E}^{\mathrm{eq}}) \tag{34}$$

where $\mathrm{E}^{\mathrm{poly}}$ and E^{eq} are the energies per atom for the polycrystal, and a perfect crystalline supercell of the metal (i.e. cohesive energy), respectively, and f^{gb} is the site fraction of GB atoms in the polycrystal. The adaptive-common neighbor analysis method [74] is used to compute f^{gb}; all atoms that have a different crystalline structure from the base metal are assumed to be GB atoms. We construct a supercell comprising 1,024 atoms spanning 8x8x8, 8x8x8, and 16x4x4 multiples of the orthorhombic unit cell [69,155] for bcc, fcc, and hcp metals, respectively. This is followed with a conjugate gradient energy minimization in LAMMPS to optimize the supercell for both the lattice parameter, and atomic positions (for each interatomic potential).

To compute $\Delta E_{sol}^{B\ in\ A}$, we substitutionally add one solute atom (B) into the 1,024 atom supercell of solvent (A), and compute:

$$\Delta E_{sol}^{B\ in\ A}(\text{per solute atom}) = E(A_{N-1}B) - [(N-1)\cdot E_A^{eq} + E_B^{eq}] \quad (35)$$

where $E(A_{N-1}B)$ is the relaxed total energy of the supercell with one solute atom (B), N is the number of atoms in the supercell, and E_A^{eq}, E_B^{eq} are the energies per atom for both metals A and B, respectively, in their perfect crystalline (unalloyed) supercells (i.e. cohesive energies). We note that the quantity $\Delta E_{sol}^{B\ in\ A}$ is different from the traditional concentration-dependent energy of mixing $\Delta E^{mix}(x)$, where x is the solute concentration; $\Delta E_{sol}^{B\ in\ A}$ is the derivative of the mixing energy at the composition endpoint [156], $\Delta E_{sol}^{B\ in\ A} = [\partial \Delta E^{mix}/\partial x]_{x=0}$. And thus, in the dilute limit, we can approximate $\Delta E^{B\ in\ A} \approx (1/x)\cdot \Delta E^{mix}$ [157]; multiplying by $(1/x)$ converts ΔE^{mix} from a "per atom" to a "per solute atom" quantity. This is further discussed in Supplementary Section 1.2 of Ref [147].

To compute ΔE_{ord}^{form}, we use 0 K phase diagrams from the density functional theory (DFT) based Open Quantum Materials Database (OQMD) [149,150] to, first, identify if the alloy is compound forming, and second, identify the intermetallic compound with the lowest stoichiometry x_s^c, for which the relaxed ΔE_{ord}^{form} is calculated using molecular statics:

$$\Delta E_{ord}^{form} = E^{ord} - [(1-x_s^c)\cdot E_A^{eq} + x_s^c\, E_B^{eq}] \quad (36)$$

where E^{ord} is the relaxed per atom energy (using the interatomic potential) of the intermetallic compound cell (as obtained from OQMD).

We note that, for some compound-forming alloys, the available interatomic potential does not correctly predict compound formation in the alloy (e.g., gives a positive value for ΔE_{ord}^{form}). In such cases, the DFT value for ΔE_{ord}^{form}, obtained from OQMD is used (and is correspondingly marked). Although a more conservative approach would be to just discount the offending interatomic potential, this leaves us without options to screen for nanocrystalline stability in that alloy. Furthermore, it is still possible for an interatomic potential to provide accurate segregation energies, but incorrectly predict compound formation (positive ΔE_{ord}^{form}) if the potential is not well-fitted to intermetallic compounds of the alloy. For example, although the Al(Mg) potential by Zhou et al. [118] misses the relevant nearest $Al_{30}Mg_{23}$ compound, it gives similar segregation

energies to the Mendeleev et al. [67] potential, which correctly predicts compound formation (and its energetics). Therefore, in absence of other alternatives, we find this approach of using DFT values of ΔE_{ord}^{form}, when necessary, to still give us the best metrics (and chance) to examine nanocrystalline stability in a binary alloy.

In Figure 22(a), we plot the nanocrystalline ground state stability score Φ^S for 180 alloys, and in Figure 22(b), the nanocrystalline metastability score Φ^M for all 210 alloys. We removed 30 alloys (marked with X) from Figure 22 (a), for which the calculated value of $\Delta E_{ref=sln}^{solute}$, Eq. (32), is incorrectly positive even when the DFT value for ΔE_{ord}^{form} is used; this error indicates that the interatomic potential incorrectly computes the mixing and/or the compound formation energies for this alloy. In the cases where an alloy has multiple interatomic potentials available (a total of 67 alloys), we judiciously chose one of the potentials (that we think is most appropriate) to represent it in Figure 22. We highlight such choices in the Supplementary Material of Ref [147], but for all intents and purposes, this can be deemed an arbitrary choice, as it is not justified by a quantifiable metric. For completeness, we provide the calculation outputs for all alternative potentials in the Supplementary Data of Ref [147].

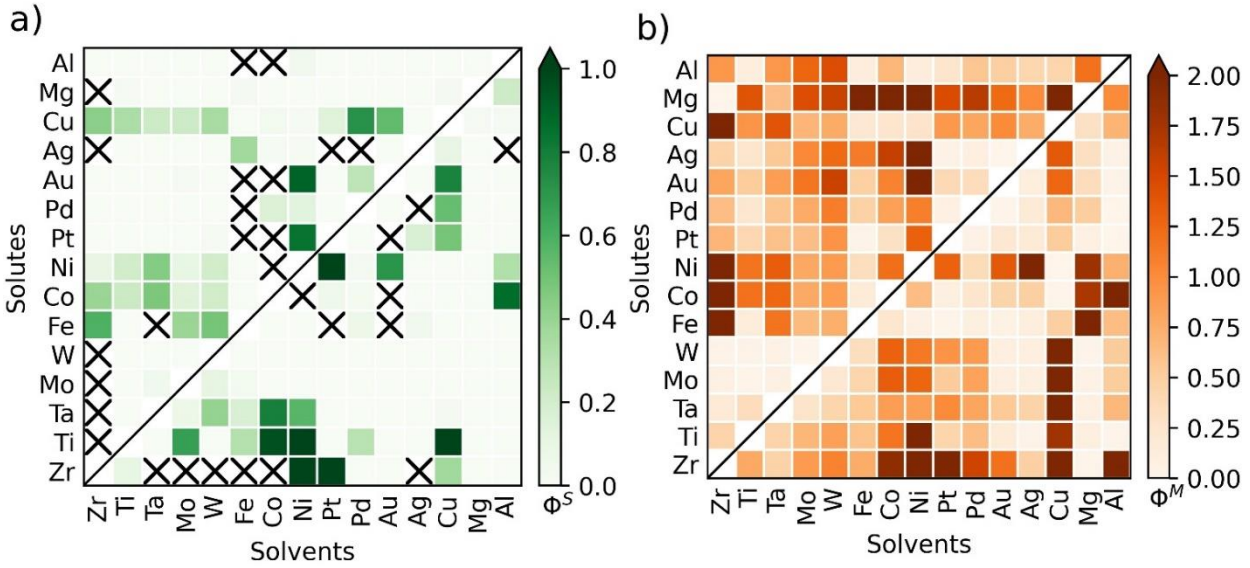

Figure 22: (a) The ground state stability score Φ^S and (b) metastability score Φ^M for the surveyed 210 alloys. Entries marked with (X) in (a) are for alloys, where the available interatomic potential gives an incorrect value of $\Delta E_{ref=sln}^{solute} > 0$ in Eq. (32).

4.3. NANOCRYSTALLINE ALLOYS VS. ENTHALPIC GROUND STATES

The ground state stability scores Φ^S, in Figure 22 (a), show that a nanocrystalline configuration, in almost all surveyed alloys, is not a formally enthalpically favorable state, compared to the equilibrium bulk state at 0 K (i.e., a two-phase state). This is established by virtue of their Φ^S scores being below unity, which by comparison with Eq. (31), means that the bulk phases are more stable at 0 K than any polycrystalline structure; the amount of GB segregation that occurs in these alloys is not enough to offset the energy cost of having the grain boundary network appear, relative to phase separation, based strictly on enthalpy at 0 K. This result aligns with the third law of thermodynamics, which permits only pure elements and ordered compounds at 0 K [158,159], as we shall discuss in more detail below. It is also consistent with our group's prior work on the phase stability of nanocrystalline alloys which has pointed to the importance of entropy and finite temperatures to achieve an equilibrium nanocrystalline state [160,161].

However, an interesting set of counterexamples is also present in the data of Figure 22(a): five alloys are outliers to the above trend, and have a score of $\Phi^S > 1$: Cu(Ti), Ni(Ti), Ni(Zr), Pt(Ni), and Pt(Zr). These points seem to suggest that GB segregated nanocrystalline states in these alloys could have a lower enthalpy than the competing bulk ground states at 0 K, with a significant fraction of their GB energy states lying in the green regime of Figure 21. However, it is important to remember that the present screening uses only a dilute-limit analysis, and neglects the energetics of solute-solute interactions. Whereas a naïve filling of the energy levels in the GB energy spectrum of Figure 21 achieves a lower enthalpy total than the competing bulk phases, a true calculation of system energy for such a non-dilute system must account for the fact that solute atoms interact physically at grain boundaries. We have addressed the issue of non-dilute solute interactions in our work in Ref. [146] in the context of the spectral segregation energy, and noted how the spectrum itself shifts as it is populated with solute.

For these particular five alloys, we expect that solute interactions at the GBs will oppose further segregation. This is because all of these alloys are negative heat of mixing alloys, meaning that solutes prefer to be surrounded by solvent atoms rather than by themselves. When segregating to a GB, this implies a short-range repulsion between solutes, such that when a favorable GB site is filled, neighboring sites should become less favorable. In Figure 21, each green site that becomes occupied shifts the distribution upward, leading to fewer green sites for subsequent segregation.

Thus, the segregation tendency, while very strong in these alloys, may decline with composition, and such decline might be enough to affect the stability proposition. Such a composition-dependence should shift their scores to $\Phi^S < 1$, similar to all other alloys surveyed.

To rigorously test this hypothesis for the five alloys with $\Phi^S > 1$, we use a two-stage Monte Carlo computation developed earlier in our work in Ref [146]. For this analysis, we use a low finite temperature rather than 0 K, to avoid getting locked in metastable states during the Monte Carlo routine. The solute interaction effects on the GB segregation spectrum that we seek to analyze are present at all temperatures, and thus the present finite temperature calculations remain relevant to the discussion at 0 K as well.

First, for a given solute concentration, we run a Monte Carlo equilibration that is strictly energetic, on a full numerical GB segregation energy spectrum that is constant, i.e., does not change as it is populated. Solute atoms are first assigned as bulk solutes ($\Delta E_i^{seg} = 0$), and subsequently allowed to swap with solvent atoms; swap attempts are accepted according to the Metropolis criterion using dilute-limit segregation energies from the spectrum; the equilibrated segregation state from this stage of the computation is the one we expect assuming no solute interactions at the GB.

Second, to account for solute interactions, the output of the first stage is used as the input to a fully atomistic hybrid Monte Carlo/Molecular Dynamics simulation; one hybrid step is a Monte Carlo run of one swap attempt per solute atom, followed by a molecular dynamics run at finite temperatures for relaxation, for 20 steps with a time step of 1 fs. A total of 1000 hybrid steps are used to achieve equilibration. As all atoms are allowed to interact in the hybrid simulation, the final equilibrated state is the true equilibrium segregation state for the nanocrystalline structure at the prescribed solute concentration. The difference between the final segregation states from the two stages determines the nature of GB solute interactions for the system; for repulsive interactions, the output of the second stage should have less solute content at the GB.

We applied this procedure to all five alloys, using the $(20\ \text{nm})^3$ polycrystals from Section 4.2, and a total solute concentration of 10% at 300 K. The procedure results are shown, as an example, for Pt(Ni) [114] in Figure 23. For this alloy, filling all GB sites with solute atoms barely crosses the threshold of stability with a score of $\Phi^S = 1.04$. But as shown in Figure 23, the repulsive nature of solute interactions is strong enough to reduce the equilibrium solute concentration at the

GB from 0.48 to 0.27 – more than 40% reduction in occupancy of GB sites; this roughly translates to a 40% reduction in the stability score for Pt(Ni). The repulsive solute interactions at the GB make it energetically unfavorable to fill all (dilute-limit favorable) GB sites, and thus, will depress the score for Pt(Ni) to $\Phi^S < 1$. Similarly, parallel simulations show that the other four alloys listed above also have repulsive solute interactions at the GB (as posited earlier) large enough in magnitude to reduce their computed dilute-limit score below unity as well. We note that for other alloys, the opposite effect is possible, i.e. to raise the Φ^S score, in the case of attractive solute interactions at the GB. This is an interesting effect that further motivates the need for a full understanding of the nature and magnitude of solute interactions in all surveyed alloys, and will be the focus of future work.

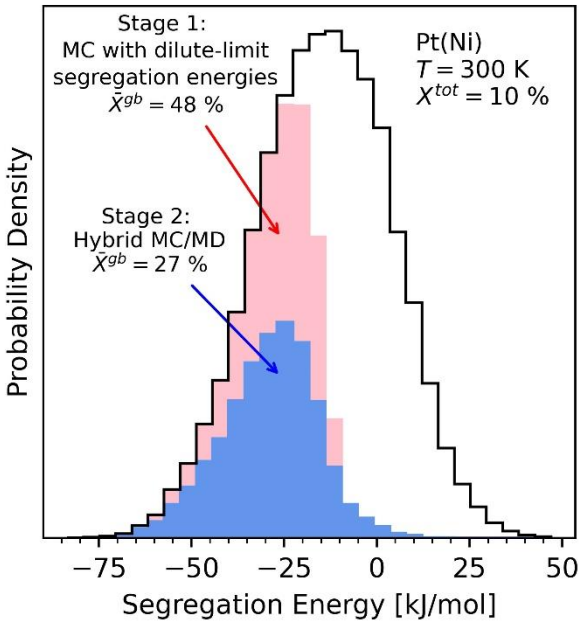

Figure 23: An illustration of the two-stage procedure developed in Ref [146] to show the impact of solute interactions on the equilibrium segregation state for Ni solutes in a Pt polycrystal [114], for a total solute concertation, $X^{tot} = 10\%$, and T=300 K. The repulsive solute interactions at the GB reduce the solute concentration at the GB from $\bar{X}^{gb} = 48\%$ to 27%. The shaded red and blue regions show the occupied GB sites (by solute atoms) before, and after taking into account solute interactions, respectively.

This analysis suggests that a full spectral view of GB segregation is needed to enforce the third law of thermodynamics, including not only the dilute-limit form of the spectrum, but its evolution

with increasing concentration. The third law posits that the entropy of a system (including all its subsystems, e.g. configurational, vibrational, etc.) approaches zero, as the temperature approaches zero [158,159]. In other words, the ground state must be non-degenerate, whereas grain boundary networks are generally highly degenerate. This observation helps clarify thermodynamic difficulties associated with the use of a single 'average' segregation energy. Often when such a single segregation energy value is calculated (for example, in experiments), it represents some average over the lowest-energy sites in the full spectrum, as those are the sites that nature actually samples. And indeed, those segregation enthalpies, reflective of just the tail of the spectrum, can outcompete bulk phases [26]. This situation will be discussed at more length with specific examples in Section 6. However, in a fuller statement of the ground state conditions, the entire spectrum needs to be considered, including the favorable and the unfavorable sites, the latter of which are difficult to measure since they would never be naturally sampled. We note that one possible caveat to this discussion would be the formation of highly ordered GB complexions [10,11,162–165]. While it is known that some GBs can exhibit phase-like energetics, it is not clear whether any complexions might be ground state configurations at 0 K, or whether a full GB network could be comprised of such. This poses an interesting question for future work, in which details of the GB segregation spectrum would need to be altered to permit specific populations of GB types.

In any event, a critical finding here is that when the full GB segregation spectrum is employed, our results suggest that it should be possible to enforce the third law for a rigorous thermodynamic analysis. This is important because although GB states are not 0 K ground states, at finite temperature they can appear when entropy favors activation out of the ground state [160,161] . At finite temperatures, it is only necessary that the GB energies outcompete the equilibrium phases, which for low solute contents means solid solutions. Our analysis shows that nanocrystalline alloys are often stable against solid solution formation; this is indicated by Figure 22(b) and will be the focus of the next section.

4.4. Screening nanocrystalline alloys stable against solid solution formation

In contrast to Φ^s, which is relevant at 0 K, the metastability score Φ^M, is relevant at finite temperatures. Especially for the dilute limit case that we address in this work, a terminal solid solution is the correct bulk phase against which the GB segregated state would compete. And as

shown in Figure 22 (b), Φ^M has a wider range of stabilization possibilities for nanocrystalline alloys. For more than one-third of surveyed alloys, it is possible to eradicate the enthalpic penalty of the GB network, and have a nanocrystalline configuration that is at least enthalpically comparable ($\Phi^M = 1$) or favorable ($\Phi^M > 1$) to a crystalline random solid solution. This observation suggests that, at finite temperatures, a nanocrystalline configuration is the thermodynamic equilibrium state in a large number of alloys, in a similar fashion to the thermodynamic stability of a solid solution (over a temperature-composition range) in the bulk phase diagram. This is the conclusion of prior studies mapping the entropic effects on structural equilibria in nanocrystalline alloys as well [26,160], and the rankings in Figure 22(b) provide a new quantitative view of this on the basis of a fuller understanding of the GB segregation spectrum.

Table 3: Calculated Φ^S and Φ^M scores, and the maximum homologous temperature (relative to the alloy solidus) for stability for several alloys with experimentally observed nanocrystalline stability/metastability.

Alloy	Solute Concentration [at. %]	Maximum Temperature [K]	Homologous Temperature	Φ^S	Φ^M	Ref.
Ag(Ni)	25	673	0.5	0.0	2.0	[166]
Ag(W)	0.3	473	0.4	0.0	0.1	[167]
Co(W)	11	873	0.5	0.0	1.3	[168]
Cu(Ag)	30	573	0.5	0.1	1.4	[169]
Cu(Ta)	10	1173	0.9	0.0	6.2	[170]
Cu(W)	14	673	0.5	0.0	2.6	[171]
Cu(Zr)	3	1223	1.0	0.4	2.0	[172]
Fe(Ag)	3.2	673	0.5	0.4	1.1	[173]
Fe(Cu)	5	600	0.3	0.0	0.2	[174]
Fe(Mg)	10	1036	1.1	0.0	2.7	[175]
Fe(Ta)	1	873	0.5	0.2	0.5	[22]
Fe(Zr)	4	1173	0.7	–	0.8	[176]
Ni(Cu)	30	573	0.4	0.0	0.3	[177]
Ni(W)	21	773	0.4	0.0	1.1	[24]
Pt(Au)	10	775	0.4	0.0	0.4	[49]
Pd(Zr)	19	873	0.5	0.0	1.3	[178]
Ti(Cu)	10	583	0.3	0.3	0.9	[179]
W(Ti)	20	1373	0.5	0.0	0.9	[19]

The results in Figure 22(b) are immediately applicable to any dilute alloy within its nominal solid solution range on the bulk phase diagram. For the alloys in Figure 22(b) with $\Phi^M > 1$, the existing bulk phase diagrams require revision in the face of the nanocrystalline, GB-segregated alternative state that is not typically considered in phase analysis, because their expected solid solutions are of higher energy than the nanocrystalline state. The extent to which such considerations reshape the phase diagram and extend into the nominal bulk two-phase fields is a topic of some of our future work.

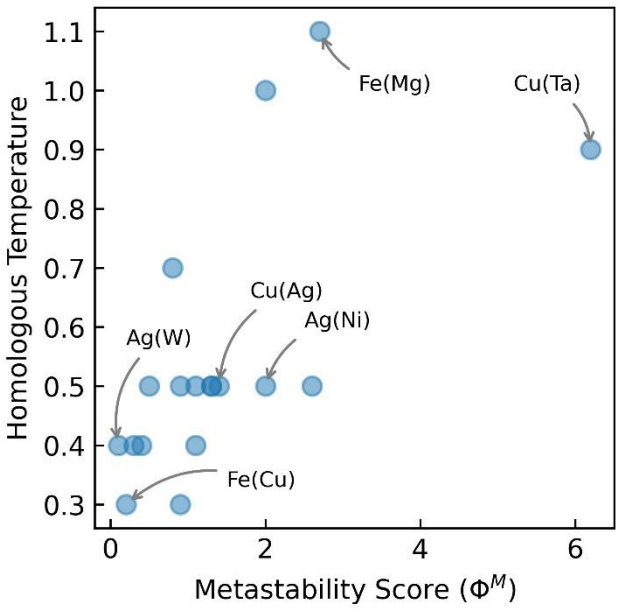

Figure 24: The metastability scores for alloys in Table 3 versus the maximum experimentally observed homologous temperature (calculated relative to the alloy solidus) for nanocrystalline stability. We highlight three pairs of alloys (of the same base metal) where a higher metastability score translates into observed nanocrystalline stability at higher temperatures.

The score Φ^M appears able to predict the possibility of equilibrium nanocrystalline states in a number of experimental systems studied for their stability, including Ag(Ni) [166], Cu(Ta) [170], Cu(Zr) [172], Fe(Mg) [175], Ni(W) [24], and Pd(Zr) [178]. In general, the higher the Φ^M score for an alloy, the more feasible a nanocrystalline configuration is; for example, a score of $\Phi^M = 4$ requires solute segregation at only 25% of favorable GB sites ($\leq$ 25% of the GB network), as opposed to $\Phi^M = 1$ that requires solute segregation at 100% of favorable GB sites. This effect should translate into higher stability temperatures for higher Φ^M scores (for alloys of the same base metal). To illustrate, we plot in Figure 24 the values of Φ^M against the maximum homologous

temperature (calculated relative to the solidus of the alloy) at which alloys in Table 3 are experimentally observed to be stable. And indeed, a positive correlation does exist between Φ^M and the maximum temperature across all alloys. Perhaps more specifically relevant, we see that alloys of the same base metal with higher Φ^M scores tend to be metastable at higher homologous temperatures, such as Cu(Ta) [170], Fe(Mg) [175], and Ag(Ni) [166], compared to Cu(Ag) [169], Fe(Cu) [174], and Ag(W) [167], respectively.

As a final comment on this nanocrystalline alloy screening tool, we note that the use of interatomic potentials, though a step forward in screening compared to an "averaged" segregation energy, has limitations. For example, the computed Φ^M and Φ^S scores are quite sensitive to the choice of interatomic potential. For example, the Al(Ni) system had Φ^M scores that varied from 0 to 3.5 between 5 different potentials [111,118,122,180,181]; this is far more than an issue of accuracy, and affects the fundamentals of the thermodynamic equilibrium. Also, for many of the present alloys, only one interatomic potential is available, by Zhou et al. [118], which is not fitted to intermetallic compounds or alloy solid solutions. And, though one could imagine that errors in energetics will mostly self-cancel (i.e. if the segregation, mixing, and compound formation energies are all off, their relative errors may cancel out), there is no guarantee to that effect. The fact that 30 alloys (marked with X in Figure 22 (a)) have an interatomic potential that fails to correctly compute a positive value for $\Delta E^{solute}_{ref=sln}$ in Eq. (32) suggests that such errors of potential are a serious concern for this kind of analysis. This work thus calls for more validation efforts to test the reliability of potentials in capturing the energetics of solute segregation at GBs [123], and further motivates the need for the evolving field of quantum-accurate machine-learning based interatomic potentials [86,87,94].

4.5. Spectral Improvements over the Classic "Averaged" Approach to Nanocrystalline Stability

To compare the findings of the spectral approach to that of a classic "averaged" approach in the spirit of Weissmuller's model, we apply the nanocrystalline stability criteria developed earlier by Kalidindi and Schuh [26] to the 210 alloys surveyed here. The Kalidindi-Schuh framework employs the same enthalpic approach (outlined here), but with two main distinctions: first, it uses an "averaged" segregation energy to represent the whole GB network $\Delta\bar{E}^{seg}$, and second, uses a

Miedema-based approach [120,182] to compute $k_\gamma\gamma$, $\Delta\bar{E}^{seg}$, $\Delta E^{B\ in\ A}$, and obtains ΔE_{ord}^{form}directly from OQMD. To directly compare to the spectral Φ^M scores, we reformulate the Kalidindi-Schuh criterion, and express it in terms of a non-spectral or "averaged" score Φ_{avg}^M, with the metastability condition $\Phi_{avg}^M \geq 1$:

$$\Phi_{avg}^M = \frac{1}{-k_\gamma\gamma} \cdot \min\{0, \Delta\bar{E}^{seg}\} \tag{37}$$

where the subscript "avg" is used as a reminder that this criterion is non-spectral and uses a single 'average' grain boundary segregation energy. The "min" function in Eq. (37) sets the minimum value to zero, because otherwise, a positive value for $\Delta\bar{E}^{seg}$ would result in a negative "averaged" score. There are alloys which have average GB segregation energies that are in this "anti-segregating" regime, which is an artifact of not allowing a full spectrum of GB segregation states.

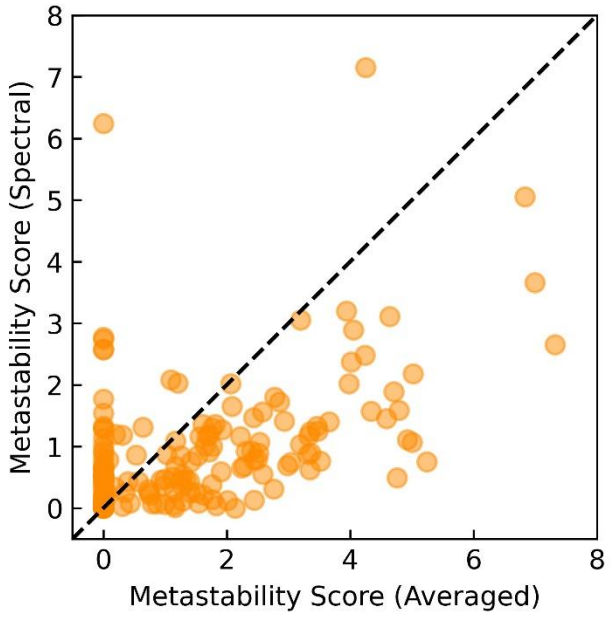

Figure 25: A comparison of the "averaged" metastability score Φ_{avg}^M, Eq. (37) with the spectral Φ^M, Eq. (28).

We compute Φ_{avg}^M scores for all 210 alloys, and plot it against the spectral metric Φ^M in Figure 25. First, it is encouraging to see a general correlation between these analyses; the averaged approach typically can separate strong from weak segregators. However, the "averaged" score Φ_{avg}^M is generally higher (as shown in the lower triangle of Figure 25) than the spectral Φ^M, with ~25% of alloys predicted to be stabilized by Φ_{avg}^M but not Φ^M; in comparison, only ~9% of alloys

switch in the other direction, with the spectral approach anticipating metastability when the averaged model does not.

A contributing factor to the discrepancy between the two screening approaches is the different method used to compute $k_\gamma\gamma$, $\Delta E^{B\ in\ A}$ and ΔE_{ord}^{form} (Miedema-based versus atomistic simulations). However, the major factor to emphasize is the spectral versus "averaged" representation of segregation energies, i.e. $F_i^{gb}(\Delta E_i^{seg})$ versus $\Delta\bar{E}^{seg}$. We explore this in Figure 26 using Fe(Mg) as an example. This is a system that has been reported to have significant thermal stability in nanocrystalline form, and explicit documentation of grain boundary segregation as well [175,183]. In Figure 26(a), we show the Kalidindi-Schuh construction of the energetics, which compares the grain boundary segregation energetics (y-axis) against the bulk phase energetics (x-axis). In Figure 26(b), we show a computed grain boundary segregation spectrum [148,184] for comparison.

For this system, both the spectral and "averaged" approaches compute very similar values for $k_\gamma\gamma \approx 12$ kJ/mol, $\Delta E^{B\ in\ A} \approx 72$ kJ/mol, and $\Delta E_{ord}^{form} = 0$ (non-compound forming). What is more, the Miedema-based "averaged" value for dilute segregation, $\Delta\bar{E}^{seg} = -86$ kJ/mol, is an accurate approximation, as it does fall on the attractive (dilute) tail of the ΔE_i^{seg} spectrum calculated by the interatomic potential [184], as shown in Figure 26(b). In fact, the Miedema value is a reasonable "average" for the first 5% solute added to the GB network, and lies within the green "stable" region of Figure 26(a) where the segregation energies are below the competing phase energies in this system. However, the classic "averaged" approach takes that single $\Delta\bar{E}^{seg}$ value and assigns it to the whole GB network, when in fact, the majority of the segregation spectrum is far less attractive (Figure 26(b)). The "averaged" approach thus misses the need to include many unattractive sites in the system in order to create the few most favorable ones; it overpredicts the stability of the GB network.

The spectral approach captures the true fraction of GB sites that have comparable segregation energies to the "averaged" value, $\Delta E_i^{seg} \leq \Delta\bar{E}^{seg}$ (Figure 26(b)), and thus more realistically represents the level of stability of this alloy. In this case, it is the spectrality of the GB network (independently of other factors) that shifts the stability prediction for Fe(Mg) from enthalpically stable according to the "averaged" approach (as $\Delta\bar{E}^{seg} - \Delta E_{ref=sln}^{solute} < -k_\gamma\gamma$) to a metastable

system (with Φ^M = 2.65), which matches its experimentally observed limited stability up to 763 °C (~0.5 of the liquidus temperature for Fe).

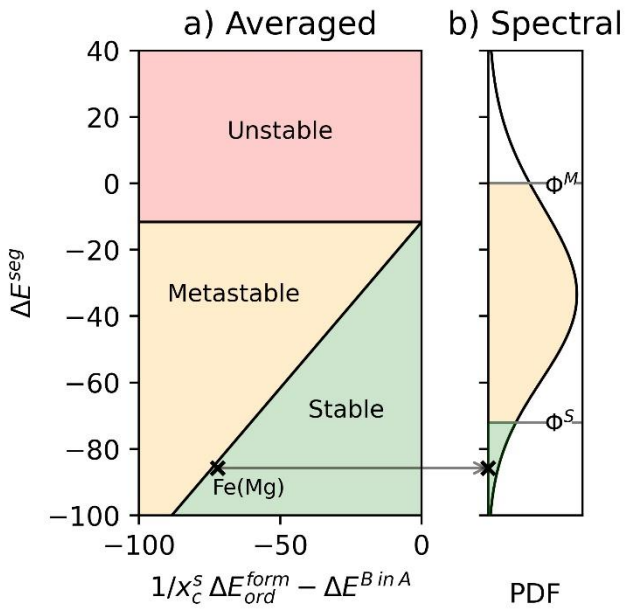

Figure 26: A comparison of the (a) "averaged" and (b) spectral approach to screening Fe(Mg) for nanocrystalline stability. As the "averaged" approach assumes a dilute value for $\Delta\bar{E}^{seg}$ for the whole GB network, the classic stability map in (a) predicts the system to be stable. However, by examining the spectrum of segregation energies (probability density function (PDF)) in (b), we realize that only a small fraction of GB sites has comparable (favorable) segregation energies to $\Delta\bar{E}^{seg}$ (green shaded area bounded by Φ^S), which is not enough to stabilize the whole GB network. Instead, the spectral approach predicts the system to be metastable, as a large fraction of GB sites (yellow shaded region in (b)) is accessible to Φ^M.

4.6. Conclusion

In conclusion, we have outlined the thermodynamic framework for screening the thermodynamic stability of nanocrystalline alloys, in the presence of a spectrum of solute segregation energies at the GB; the framework is strictly enthalpic, and uses easily obtainable quantities from atomistic simulations at 0 K. We used the framework to screen for nanocrystalline stability and metastability in 210 alloys. The main findings are:

- *Nanocrystalline configurations are not ground states at 0 K*: a nanocrystalline configuration can be enthalpically comparable to a solid solution, but not the ground state at zero Kelvin for an alloy. In just 5 out of 180 cases studied here, alloys were

found to exhibit dilute-limit energetics that implied enthalpic stability of segregated GBs, but a more detailed analysis including non-dilute (solute interaction) effects corrected that interpretation; none of the alloys screened here exhibit energetics such that GBs are 0 K ground states. And thus, similar to solid solutions, the thermodynamic stability of nanocrystalline configurations (when they are possible) will also involve entropic contributions at finite temperatures.

- *The GB segregation spectrum permits a strict enforcement of the third law of thermodynamics*: in contrast to the classical "averaged" approach, a full accounting of the spectrality of the GB network, and solute-solute interactions, enforces the third law of thermodynamics, as it pertains to permissible alloy ground states at zero Kelvin.
- *The "averaged" approach usually overestimates nanocrystalline stability*: The "averaged" approach in which a single grain boundary segregation energy is used to evaluate GB energetics, tends to only sample the attractive (dilute) tail of the GB spectrum, and assigns its segregation value to the whole GB network. This fails to capture the full energetic penalty of having a GB network, and its less attractive (and unattractive) sites; as such, the "averaged" approach tends to overestimate nanocrystalline stability.
- *The metastability score Φ^M is a good screening metric*: the metric Φ^M compares the energetics of GB segregation with those of solid solution formation and exhibits good predictive power for experimentally observed nanocrystalline stability. A higher Φ^M score correlates with increased nanocrystalline stability at higher homologous temperatures.

Finally, the findings of this Chapter suggest that entropy plays a significant role in stabilizing nanocrystalline alloys. The inclusion of the full free energy (both enthalpic and entropic contributions) should be pursued in future studies of nanocrystalline alloys, in order to fully understand the prospect of thermodynamic stability at finite temperatures, and map "nanocrystalline regions" across the composition-temperature space in phase diagrams.

5. Grain Boundary Segregation Beyond the Dilute Limit

In Chapters 2-4, we assumed a dilute-limit analysis. However, when GB segregation occurs beyond the dilute limit, it collects solutes in close proximity to one another and locally amplifies the concentration dramatically, so a critical aspect of the theory of GB segregation is the treatment of concentration dependence of GB segregation [25,31,36,185–189]. The most common approach to modeling concentration dependence in GB segregation is based on the concept of Fowler and Guggenheim [31], who argued that at higher concentrations, the interaction between solutes increases, opposing further GB segregation when the interaction is repulsive, or conversely, promoting further segregation in the case of attractive interactions; the model uses an average solute interaction energy term to account for this effect.

However, there is a second, independent contribution to the concentration dependence of GB segregation that is considerably less studied and understood, namely, the gradual exhaustion of the most energetically suitable segregation sites. In Chapter 2, we showed that GBs, with their complicated set of atomic environments, present a variety of unique atomic sites for GB segregation, and these have a spectrum of energies [34,37–40,42,46]. Many authors have explored the range of segregation sites in individual boundaries [44,190–198], and in Chapters 2 and 3, we showed that this spectrum is a mildly skewed normal distribution in a polycrystal [82]. Given such a distribution, GB segregation occurs first at the most favorable sites, leaving them unavailable for the next round of solute atoms, forcing consequent segregation at less desirable GB sites and reducing the segregation tendency with increasing solute concentration.

The solute interaction effect and the site saturation effect are, to first order, independent of each other, but there has been no prior study of their relative importance or even any effort to disentangle their effects on the concentration dependence of GB segregation. Therefore, in this Chapter, our goal is to develop a methodology to separate these two contributions for the first time, and directly measure their relative importance to segregation in a binary polycrystalline alloy. This, in turn, enables the development of atomistically-informed segregation isotherms that account for both contributions.

5.1. THERMODYNAMICS OF GRAIN BOUNDARY SEGREGATION

In this section, we briefly review the thermodynamics of segregation in a binary alloy from two perspectives: (i) the classical approach, which uses an average segregation energy, $\Delta\bar{E}^{seg}$, and (ii) the spectral approach, which uses a distribution of segregation energies at the GB, $F_i^{gb}(\Delta E_i^{seg})$.

5.1.1. The classical "average" approach

This approach – first outlined by McLean [30] – represents the grain boundary network with an "average" $\Delta\bar{E}^{seg}$, which is the energy difference between a solute atom occupying a GB site, E_{gb}^{solute}, and a bulk site, E_c^{solute}:

$$\Delta\bar{E}^{seg} = E_{gb}^{solute} - E_c^{solute} \tag{38}$$

and assumes that $\Delta\bar{E}^{seg}$ is independent of GB character, average solute concentration at the GB ($\bar{X}^{gb}$), and temperature (T). These assumptions lead to the classic McLean isotherm [30]:

$$\frac{\bar{X}^{gb}}{1-\bar{X}^{gb}} = \frac{X^c}{1-X^c}\exp\left(-\frac{\Delta\bar{E}^{seg}}{kT}\right) \tag{39}$$

where X^c is the solute concentration in the bulk (intra-grain) regions and k is Boltzmann's constant. Eq. (1) can be rearranged to solve directly for $\bar{X}^{gb}$:

$$\bar{X}^{gb} = \left[1 + \frac{1-X^c}{X^c}\exp\left(\frac{\Delta\bar{E}^{seg}}{kT}\right)\right]^{-1} \tag{40}$$

To explain the concentration dependence of GB segregation beyond the dilute-limit, Fowler and Guggenheim proposed adding an interaction term, ω, to account for increasing solute-solute interactions as a function of $\bar{X}^{gb}$; this modification translates into the classic Fowler-Guggenheim isotherm [31]:

$$\frac{\bar{X}^{gb}}{1-\bar{X}^{gb}} = \frac{X^c}{1-X^c}\exp\left(-\frac{\Delta\bar{E}^{seg} + \omega\bar{X}^{gb}}{kT}\right) \tag{41}$$

We note that the interaction term $\omega\bar{X}^{gb}$ assumes that solute-solute interactions in the bulk are negligible, and it can be generalized to include bulk terms in a variety of ways [36], the simplest of which is with an additional correction term ($\pm\omega X^c$).

5.1.2. The spectral approach

On the other hand, the spectral approach argues that grain boundary networks have complex environments and a variety of site-types (i) that cannot be represented with a single "average" $\Delta\bar{E}^{seg}$, but with a distribution F_i^{gb} of segregation energies ΔE_i^{seg} [37–39,42]. For each site-type (i), its solute concentration, X_i^{gb}, is given as an analog of Eq. (2) [37,42]:

$$X_i^{gb} = \left[1 + \frac{1 - X^c}{X^c} \exp\left(\frac{\Delta E_i^{seg}}{kT}\right)\right]^{-1} \tag{42}$$

and the total concentration of solute at the GB, $\bar{X}^{gb}$, is the weighted integral of solute concentration at the different site-types (i) [40]:

$$\bar{X}^{gb} = \int_{-\infty}^{\infty} F_i^{gb} X_i^{gb} \; d\Delta E_i^{seg} \tag{43}$$

Combining Eqs. (42) and (43):

$$\bar{X}^{gb} = \int_{-\infty}^{\infty} F_i^{gb} \left[1 + \frac{1 - X^c}{X^c} \exp\left(\frac{\Delta E_i^{seg}}{kT}\right)\right]^{-1} \; d\Delta E_i^{seg} \tag{44}$$

Though F_i^{gb} can notionally take any form, we have shown that a skew-normal function is appropriate for polycrystals [82], which requires three parameters: the characteristic energy μ, width σ and shape α of the distribution:

$$\mathrm{F_i^{gb}} = \frac{1}{\sqrt{2\pi}\,\sigma} \exp\left[-\frac{\left(\Delta E_i^{seg} - \mu\right)^2}{2\sigma^2}\right] \mathrm{erfc}\left[-\frac{\alpha\left(\Delta E_i^{seg} - \mu\right)}{\sqrt{2}\,\sigma}\right] \tag{45}$$

At this point, it is important to note that the classical McLean isotherm, Eq. (40), and the spectral isotherm of Eq. (44) both neglect any energetic contribution from solute-solute interactions; they are analogs of one another for the two approaches. However, whereas the McLean form, Eq. (40), has no concentration dependence of grain boundary segregation, Eq. (44) carries an implicit concentration dependence because it includes a site spectrum which would tend to fill with solute in increasing order of energetic preference. This form can, therefore, be used to explicitly evaluate the spectral contribution to concentration dependence.

To address the full concentration dependence, though, requires that we further adapt Eq. (44) to account for solute-solute interactions. In the spirit of the Fowler-Guggenheim model, we might adopt the simplest possible approach and add a linear mean-field interaction term $\omega\bar{X}^{gb}$:

$$\bar{X}^{gb} = \int_{-\infty}^{\infty} F_i^{gb}\left[1 + \frac{1-X^c}{X^c}\exp\left(\frac{\Delta E_{i,\omega=0}^{seg} + \omega\bar{X}^{gb}}{kT}\right)\right]^{-1} d\Delta E_i^{seg} \tag{46}$$

We note that the subscript ($\omega = 0$) is added to ΔE_i^{seg} to stress that the GB site energies must be computed in the limit where solute-solute interactions are negligible.

5.1.3. Finite Grain Sizes

In a closed system with finite grain sizes, the total solute concentration $\mathrm{X^{tot}}$ is fixed, and shared by the bulk (intra-grain) and GB site fractions ($f^c + f^{gb} = 1$), according to the mixture rule [199]:

$$X^{tot} = (1 - f^{gb})X^c + f^{gb}\bar{X}^{gb} \tag{47}$$

The total grain boundary site fraction is typically connected to grain size (d) and thickness (t) using $f^{gb} = 1 - [(d-t)/d]^3$ [141].

Although it is a common practice in the literature on GB segregation to assume $X^c \cong X^{tot}$, this is invalid when $\mathrm{f^{gb}}$ is not negligible, e.g., in nanocrystalline alloys or in the limited sampling volumes of atomistic simulations. In those cases, the McLean, Eq. (40), Fowler, Eq. (41), and spectral, Eq. (44), isotherms should all be recast in terms of the mixture rule, Eq. (47).

Combining Eqs. (40) and (47) gives us the generalized (mixture rule) form of the McLean approach:

$$\mathrm{X^{tot}} = \left(1 - \mathrm{f^{gb}}\right)\mathrm{X^c} + f^{gb}\left[1 + \frac{1-X^c}{X^c}\exp\left(\frac{\Delta\bar{E}^{seg}}{kT}\right)\right]^{-1} \tag{48}$$

Similarly, casting the Fowler model Eq. (41) into the general form of Eq.(47), we obtain:

$$\mathrm{X^{tot}} = \left(1 - \mathrm{f^{gb}}\right)\mathrm{X^c} + f^{gb}\left[1 + \frac{1-X^c}{X^c}\exp\left(\frac{\Delta\bar{E}^{seg} + \omega\bar{X}^{gb}}{kT}\right)\right]^{-1} \tag{49}$$

and substituting for $\bar{X}^{gb}$ from Eq. (47):

$$\mathrm{X^{tot}} = f^c\,\mathrm{X^c} + f^{gb}\left[1 + \frac{1-X^c}{X^c}\exp\left(\frac{\Delta\bar{E}^{seg} + \omega\,[X^{tot} - f^cX^c]/f^{gb}}{kT}\right)\right]^{-1} \tag{50}$$

Eq. (50) is the generalized form of the Fowler-Guggenheim approach that solves for the equilibrium segregation state, which accounts for the concentration dependence of GB segregation and finite grain sizes. In the limit of dilute concentrations ($\bar{X}^{gb} \to 0$) or weak interactions ($\omega \to 0$), the McLean form, Eq. (48), is recovered.

In a similar fashion, we combine Eqs. (44) and (47) to obtain the governing spectral relationship for a closed system with multiple site-types at the GB without solute-solute interactions [82]:

$$\mathrm{X^{tot}} = \left(1 - \mathrm{f^{gb}}\right)\mathrm{X^c} + f^{gb}\int_{-\infty}^{\infty} F_i^{gb}\left[1 + \frac{1-X^c}{X^c}\exp\left(\frac{\Delta E_i^{seg}}{kT}\right)\right]^{-1} \mathrm{d}\Delta E_i^{seg} \tag{51}$$

and in the case of solute-solute interactions, Eqs. (46) and (47) are combined to give:

$$\mathrm{X^{tot}} = \left(1 - \mathrm{f^{gb}}\right)\mathrm{X^c} + f^{gb}\int_{-\infty}^{\infty} F_i^{gb}\left[1 + \frac{1-X^c}{X^c}\exp\left(\frac{\Delta E_i^{seg} + \omega\bar{X}^{gb}}{kT}\right)\right]^{-1} \mathrm{d}\Delta E_i^{seg} \tag{52}$$

and substituting for $\bar{X}^{gb}$ from Eq. (47), we obtain the thermodynamic framework to solve for equilibrium segregation in GBs with both multiple site-types and solute-solute interactions:

$$\mathrm{X^{tot}} = f^c\mathrm{X^c} + f^{gb}\int_{-\infty}^{\infty} F_i^{gb}\left[1 + \frac{1-X^c}{X^c}\exp\left(\frac{\Delta E_{i,\omega=0}^{seg} + \omega(X^{tot} - f^cX^c)/f^{gb}}{kT}\right)\right]^{-1} \mathrm{d}\Delta E_i^{seg} \tag{53}$$

We note that these generalized (mixture rule) forms of the McLean, Eq. (48), Fowler, Eq. (50), and spectral isotherms without/with interactions, Eqs. (51) and (53), respectively, are presented differently from the literature norm of segregation isotherms in the form of $\bar{X}^{gb} = f(X^c)$, such as in Eq. (1). In fact, Eqns. (50), (51) and (53) have no closed form solutions, and further simplification is not possible. Instead, for a given X^{tot}, f^{gb}, T (and F_i^{gb} for the spectral models), we must solve numerically for X^c that satisfies the left-hand side of the equations (prescribed X^{tot}), which solves concurrently for the equilibrium distribution of solute atoms in the bulk X^c and GB X^{gb}. The added complexity of such isotherms is necessary in order to correctly solve for the equilibrium solute distribution in the case of finite grain sizes ($f^{gb} \neq 0$), and as such, moving forward, these are the isotherms used throughout the chapter, and all the figures are presented in the form of $\bar{X}^{gb} = f(X^{tot})$ to reinforce the notion that X^{tot} is the fixed prescribed quantity in the system (and not X^c, which is a variable quantity that is solved for).

5.1.4. Interpretation of Energies

It is important to point out that for all the segregation isotherms discussed in Section 5.1, a complete thermodynamic treatment should use the free energy of segregation ΔG_{seg} [46] in place of the internal energy ΔE_{seg}:

$$\Delta G_{seg} = \Delta E_{seg} - P\Delta V - T\Delta S_{seg}^{xs} \tag{54}$$

where P is the pressure, ΔV is the change in volume and ΔS_{seg}^{xs} is the excess non-configurational entropy of segregation [200]. In this chapter, we take the approach of limiting our discussion to the internal free energy of segregation as represented in Eqs. (1-16), in the following manner. First, the term $P\Delta V$ is negligible in solids [77] and thus can be ignored. Second, while the non-configurational entropy can be significant at elevated temperatures and should also be spectral, in what follows we evaluate the energies of segregated conditions only at 0 K through the use of conjugate gradient minimizations, as detailed below. Although configuration space is therefore evaluated at finite temperatures, there is no contribution of excess entropy in the segregation energies as assessed. Thus, our conditions conform to the forms of the isotherms above with $\Delta G_{seg} \approx \Delta E_{seg}$.

With these measures, comparison of Eqs. (51) and (53) permits direct evaluation of the solute interaction effect, where Eq. (51) alone can handle the site spectrality effect, and Eq. (53) additionally assesses the interaction term. By comparison with the classical approach, Eq. (50), which requires two parameters to characterize a binary alloy, $\Delta\bar{E}^{seg}$ and ω, our proposed spectral approach that incorporates site spectrality for the first time, Eq. (53), requires four parameters, three for the distribution function and a fourth for interaction: μ, σ, α and ω.

5.2. Atomistic Computational Methods

We now turn our attention to the use of Eqs. (51) and (53) with atomistic data to directly measure the two contributions to the concentration dependence of GB segregation. We consider Mg segregation in an Al polycrystal as a model system, for the quality of its embedded atom method potential [67], as reported in GB segregation studies [68]. The atomistic simulation package LAMMPS is used to perform all molecular statics and dynamics simulations [66], and OVITO is used to visualize and identify atomic structures [73]. A 15x15x15 nm^3 Al polycrystal is

generated using Voronoi tessellations with the toolkit Atomsk [69], and then thermally annealed at 400 K under a Nose-Hoover thermostat/barostat for 250 ps using a time step of 1 fs, followed by cooling to 0 K at a cooling rate of 3 K/ps. The thermally annealed sample had 203,854 atoms, in 8 grains with an average diameter of 8 nm, as shown in Figure 27(a). GB sites are identified using the adaptive-common neighbor analysis method [74], with all non-FCC atoms assumed to be GB atoms – a total of 37,515 GB atoms and a GB volume fraction of 18.4%.

5.2.1. The Spectrum of Segregation Energies

To compute the distribution of segregation energies in the Al polycrystal, which is a required input for the spectral model (Eqs. (51) and (53)), we use our recently developed procedure [82], where we sample every GB site in the specimen exhaustively and compute the energy difference between the relaxed system energy at 0 K, with the solute atom at GB-site (i), $E_{gb,i}^{solute}$, and the solute atom at a bulk site, E_c^{solute}:

$$\Delta E_i^{seg} = E_{gb,i}^{solute} - E_c^{solute} \tag{55}$$

with the site for E_c^{solute} chosen as the center of a 6 nm FCC sphere to eliminate long-range interactions with GBs. The computed discrete distribution for dilute-limit Mg segregation in the Al polycrystal is shown in Figure 27(b), and is fitted to the skew-normal function, Eq. (19), with $\alpha = -1.1$, $\mu = 4$ kJ/mol, $\sigma = 19$ kJ/mol; this distribution matches that of a larger 36x36x36 nm^3 polycrystal [82], and is, therefore, representative of Mg segregation in larger Al polycrystals.

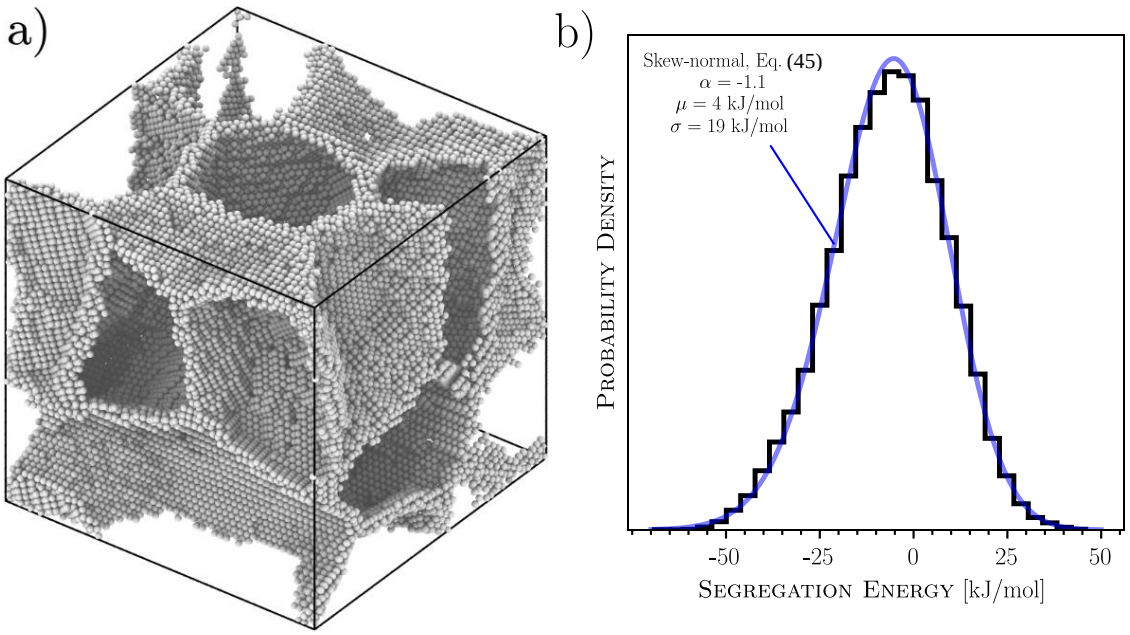

Figure 27: (a) The thermally annealed 15x15x15 nm^3 Al polycrystal with 8-grains of an average size of 8 nm; the 37,515 GB sites are only shown after deleting all FCC atoms identified using the adaptive common neighbor analysis method. (b) the calculated distribution of dilute-limit segregation energies of an Mg solute at all GB sites, and a best-fit of the skew-normal function, Eq. (19), with $\alpha = -1.1$, $\mu = 4$ kJ/mol, $\sigma = 19$ kJ/mol.

5.2.2. GB Segregation States

We need to ascertain two types of segregation states, namely, that evolved when no solute-solute interactions are allowed (corresponding to Eq. (51)) and that evolved when they are (corresponding to Eq. (53)). For this purpose, we use hybrid Monte-Carlo (MC) at finite temperatures and molecular statics (MS) simulations at 0 K to identify the equilibrium segregation state for a fixed solute concentration at finite temperatures. The hybrid scheme uses transmutational MC to sample the chemical degree of freedom, and MS lattice relaxations to sample the structural degree of freedom [201]. The choice to use molecular statics simulations at 0 K in this hybrid scheme, in lieu of molecular dynamics at finite temperatures [201], is to exclude any contributions from the non-configurational entropy (i.e. vibrational contributions) ΔS_{seg}^{xs}, as stated in Eq. (54), and thus the approximation $\Delta G_{seg} \approx \Delta E_{seg}$ holds true for our simulations. By limiting our simulations to the configurational entropy, we focus on separating the two intertwined effects of GB site spectrality and GB solute-solute interactions. Future work that employs molecular dynamics in a hybrid MC scheme could be used to separately account and solve for the excess non-configurational entropy [202], which we believe to be less than 10 J/(mol K) based on

some preliminary work in this regard. Finally, our computational procedure is divided into two stages, as elaborated below.

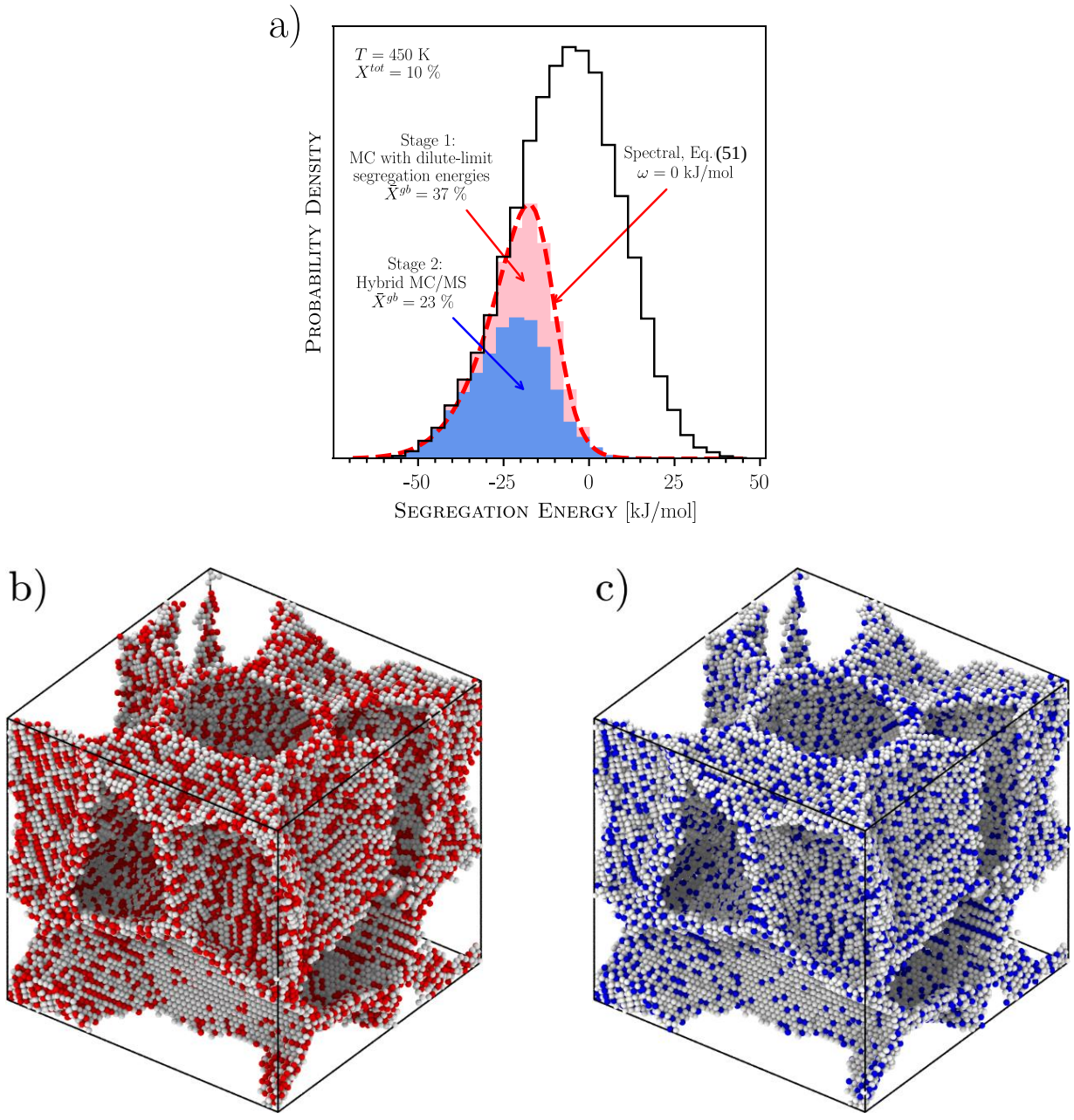

Figure 28: (a) We obtain the equilibrium segregation state for $X^{tot} = 10\%$ in two stages: First, we run an MC simulation using dilute-limit segregation energies (no-interactions); this state (shaded in red) matches the predictions of the spectral model (red dashed line, Eq. (51)) with no interactions ($\omega = 0$). Second, we run hybrid MC/MS for 1000 swaps/solute atoms (a total of $\sim 2 \times 10^7$ swap attempts for $X^{tot} = 10\%$) to correct for solute-solute interactions, and obtain the final equilibrium segregation state (shaded in blue). The equilibrated structures for both stages are shown in (b) and (c), respectively, with solute atoms colored.

In the first stage, we place solute atoms randomly at bulk (intra-grain) sites, so that the polycrystal has initially no solute atoms at the GB, and allow solute atoms to swap sites with solvent atoms using the Metropolis criterion [203], using the energy difference in the dilute-limit $\Delta E^{seg}_{i,\omega=0}$ calculated earlier (bulk sites are assigned $\Delta E^{seg}_{i} = 0$). This procedure makes no additional use of the interatomic potentials beyond the earlier exhaustive determination of the site energies $\Delta E^{seg}_{i,\omega=0}$, which are all at zero concentration. Thus, this method yields an atomistic simulation of grain boundary segregation in the absence of any solute-solute interactions. A total of 10,000 swaps per solute atom are performed, leading to an adequate system equilibration. The equilibrium segregation state predicted using this procedure matches that of the spectral model, Eq. (51), without interactions, as shown in Figure 28(a) for $\mathrm{X}^{\mathrm{tot}} = 10\%$, and for many other cases not shown. The atomic configuration for this case is shown in Figure 28(b).

In the second stage, we take the output of the first stage above as an input, and proceed to run hybrid MC/MS simulations as are often undertaken in the GB segregation literature [25,53,194,204–208]; this stage makes direct use of the interatomic potential for all energy calculations. For one hybrid step, solute/solvent atoms swaps are attempted using the Metropolis criterion at a prescribed finite temperature, with a rate of one swap per solute atom, which is followed with energy minimization using the conjugate gradient method. A total of 1000 hybrid MC/MS steps is carried out for the system to be equilibrated. This final state serves as our true equilibrium segregation state, inclusive of all atomistic effects including the site spectrality and solute-solute interactions. Figure 28 shows this state for $\mathrm{X}^{\mathrm{tot}} = 10\%$; it diverges substantially from the predictions of Eq. (51) which includes only site spectrality and no interaction effects. Notably, the total amount of segregated solute after equilibration is much lower than expected based on site spectrality alone: the blue distribution subsumes considerably less area in Figure 28 than does the red one. This speaks to repulsive solute-solute interactions favoring a significant degree of de-segregation off GBs and back into the bulk. This effect is also directly visible in the solute distribution visualized in Figure 28(c), where the total amount of solute present is lower than in Figure 28(b) (with no interactions), and furthermore, near-neighbor solute contacts are dramatically reduced owing to their repulsive interaction.

5.3. Contributions of Site Spectrality and Solute-Solute Interactions

The discussion in this section is focused on Figure 29, where we show the "true" thermodynamic segregation state, X^{gb}, measured using hybrid MC/MS simulation for values of $X^{tot} = 0.1\%$ to 10% at 450 K (data points in Figure 29). The shape of these data reflects a typical concentration dependence, where the marginal segregation tendency declines with solute content. The classical approach used to explain such concentration dependence is to assume all of it as being captured by a solute-solute interaction term alone; by fitting with the classical Fowler term to capture this effect (Eq. (50), dashed black line in Figure 29) we obtain a representative $\Delta\bar{E}^{seg} = -29$ kJ/mol and $\omega = 99$ kJ/mol for this system.

We note here that an additional correction term for possible solute-solute interactions in the bulk, ($\pm\omega X^c$), as discussed briefly in Section 2.1, though valid in general, is not necessary for our simulations. As seen in Figure 29, X^c is limited to low concentrations (<7%) over the range of conditions we have studied. In fact, at lower total concentrations before the GB becomes saturated, the bulk concentration is even lower. For all of the simulations discussed in this chapter, we estimate the average interaction distance for solutes in the bulk to be no less than 5 Å in any case, beyond which solute-solute interactions are negligible for the embedded atom potential [67]. Therefore, we limit our discussion in this chapter to the effect of GB solute-solute interactions, which are far more relevant due to the elevated concentrations in the grain boundaries.

As Figure 29 shows, above the dilute limit where the McLean model deviates from the true X^{gb}, the added Fowler "correction" of $\omega = 99$ kJ/mol results in an excellent fit for all solute concentrations. And, in the dilute limit where there are no solute-solute interactions ($\omega = 0$), the equivalent McLean solution, Eq. (48), correctly predicts X^{gb} for X^{tot} < 2% with the same segregation energy. This aligns on its face with the classical GB segregation framework, which argues that the deviation of the McLean model beyond the dilute limit is solely due to solute-solute interaction, and can be corrected by just adding ω. Similarly, prior work that has fitted limited data to Fowler-type equations can reproduce the average behavior over the range of conditions where it has been fitted. However, we will show in what follows that this is a forced-fit with no relevance to other conditions, and no extensibility beyond the fitted range. This is because the underlying physical picture of this approach is incorrect; the deviation of segregation behavior at higher concentrations is more complex, and is due to two factors, GB site spectrality, and solute-solute

interactions. In what follows we develop this notion in more detail, and subsequently return to evaluate the failings of the classical approach.

5.3.1. Site Spectrality

If we plot the predictions of the spectral isotherm without any solute-solute interaction term, Eq. (51), using the computed dilute limit distribution (μ, σ, α), rather than directly fitting to MC/MS predictions as we did with the classical approach, we obtain the red curve in Figure 29. This curve correctly predicts X^{gb} in the dilute-limit and a bit beyond, up to $X^{gb} = 10\%$ where solute-solute interactions seem to be negligible. Beyond that, the spectral ($\omega = 0$) solution deviates from the true data, and yet lies well below the McLean linear prediction; the deviation between the solid black and red curves in Figure 29 is a direct presentation of the role of site spectrality on composition dependent segregation. Whereas an "average" $\Delta\bar{E}^{seg}$ model, like McLean's, keeps adding solute atoms to the boundary with increasing concentration, the spectral model accounts for the gradual exhaustion of favorable segregation sites from the tail of the distribution in Figure 27, forcing subsequent solute atoms to compete for energetically less favorable sites, and resulting in less segregation as the overall solute concentration increases. At $X^{tot} = 10\%$, the error in a McLean-type prediction of X^{gb} is 155%; accounting for the spectrality of GB sites reduces the error to 52%, and thus gets us more than halfway to the truth. This shows, however, that we still need to account for solute-solute interactions to further reduce the error and more physically model GB segregation.

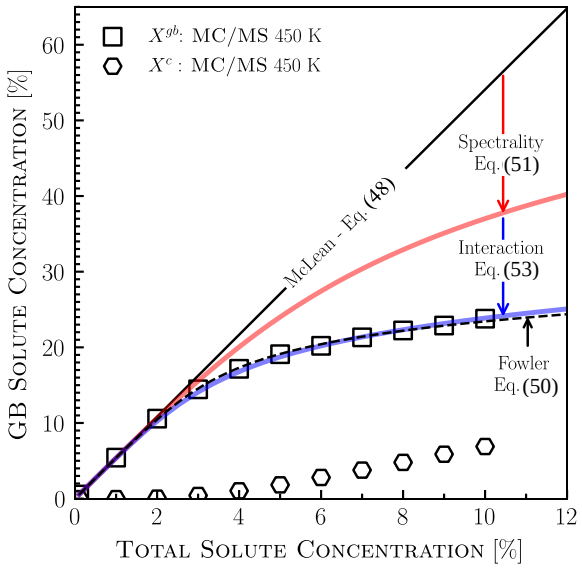

Figure 29: Comparison of the predictions of the McLean (Eq. (48), $\Delta\bar{E}^{seg} = -29\ kJ/mol$), Fowler-Guggenheim (Eq. (50) $\Delta\bar{E}^{seg} = -29$, $\omega = 99$ kJ/mol), spectral without interactions (Eq. (51) with $\omega = 0$) and spectral with interactions (Eq. (53) with $\omega = 37$ kJ/mol) models against MC/MS simulations at 450K; the contribution of spectrality to the concentration dependence of segregation is of a comparable magnitude to solute-solute interactions.

5.3.2. Solute-Solute Interactions

To extract the proper magnitude of the interaction parameter ω for use with the full spectral approach, we fit Eq. (53) to the true thermodynamic state (the MC/MS predictions) at 450 K, and obtain $\omega = 37$ kJ/mol. This fit is shown in Figure 29 as a blue solid line, where it accurately predicts the true X^{gb} for all solute concentrations. While the fit of a traditional non-spectral Fowler model (dashed black line) to this specific data set is also very good, this is an artifact of taking a narrow view on one set of conditions, a point to which we will return shortly. In any event, Figure 29 makes clear that it is the addition of the interaction component that allows the spectral model to correctly predict equilibrium solute occupancy. This is true not only of the average quantities, but in greater detail of the different GB site-types (energy levels) at the GB, as shown in Figure 30 for different X^{tot}.

These results indicate that understanding both site spectrality and solute-solute interactions are key to correctly capture the physics of solute segregation to GBs beyond the dilute-limit. It can be argued, based on Figure 29, that the spectral contribution is of an equal magnitude/importance to

the solute-solute interactions, and therefore, only by delineating both contributions can we correctly account for the concentration dependence of solute segregation across the composition and temperature space. This will be illustrated more thoroughly in the next section, where we address the ability of these various models to predict GB segregation beyond the regime where they have been fitted.

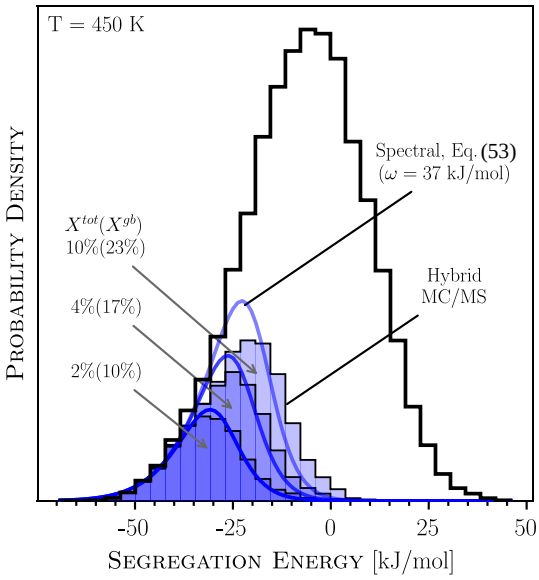

Figure 30: The predicted equilibrium segregation state, obtained using the spectral-with-interactions (Eq. (53), ω = 37 kJ/mol) model, and the true state from hybrid MC/MS simulations for X^{tot} = 2, 4, and 10%, at 450K.

5.4. Limitations of the Classical Approach are Remedied by the Spectral Approach

Though we have shown the spectral approach, once augmented with a simple solute-solute interaction term, can correctly predict the equilibrium X^{gb} beyond the dilute limit, one might argue that the same could be achieved with the classical Fowler-Guggenheim approach, based on Figure 29 (dashed black line). Using the simple average (Eq. (50)) approach with $\Delta\bar{E}^{seg} = -29$ kJ/mol and $\omega = 99$ kJ/mol gives an excellent fit of the true X^{gb} obtained from hybrid MC/MS simulations. However, as noted briefly above, this "excellent" fit is highly misleading, as the two required parameters, $\Delta\bar{E}^{seg}$ and ω, are dependent on the fitting (MC/MS) temperature and concentration range; the true test of these models lies in how well the results extrapolate to other conditions not explicitly fitted, which we now consider in fuller detail.

For a set of MC/MS simulations at T= 300, 450, and 600 K, we obtain three different equilibrium GB segregation configurations as shown in Figure 31. For each of these, we fit the classical Fowler isotherm, Eq. (50), giving the best-fit parameters summarized in Table 4. Inspection of these fitted values shows the problem clearly: because the "average" $\Delta\bar{E}^{seg}$ approach inherently misses the essential physics of segregation, no single set of $\Delta\bar{E}^{seg}$ and ω will capture the equilibrium the segregation state across the full composition and temperature space, and wildly variant values of these parameters (more than a factor of two) are needed to cover just 300 degrees of temperature range.

Table 4: Best-fit parameters for the Fowler-Guggenheim model. For each temperature, we fit Eq. (50) to MC/MS simulations to obtain representative $\Delta\bar{E}^{seg}$ and ω.

T [k]	$\Delta\bar{E}^{seg}$ [kJ/mol]	ω [kJ/mol]
300	-17	46
450	-29	99
600	-38	149

To illustrate this concept, Figure 31 shows the lower and upper bounds of the Fowler-Guggenheim approach using the three sets of best-fit parameters in Table 4, and the errors of using any one set of these parameters in other conditions are shown in Figure 32 using the maximum error of the three sets of parameters in Table 4 to illustrate the magnitude of the problem. Although the Fowler-Guggenheim model is an improvement over using McLean's model, the errors are still high, up to 22%, with an average error of 8% for all data points; we suspect that these errors could even get higher at elevated temperatures. The classic Fowler-Guggenheim model is thus only valid at the temperature used to fit its parameters, and the physical values of those parameters are highly suspect because of these limitations. Unfortunately, a common procedure in the literature is to fit a Fowler-Guggenheim type isotherm to isothermal experimental measurements of X^{gb} versus X^{tot}[186,202,209–212]. Such results are not expected to extrapolate well to other conditions outside the range of composition or temperature to which they were fitted.

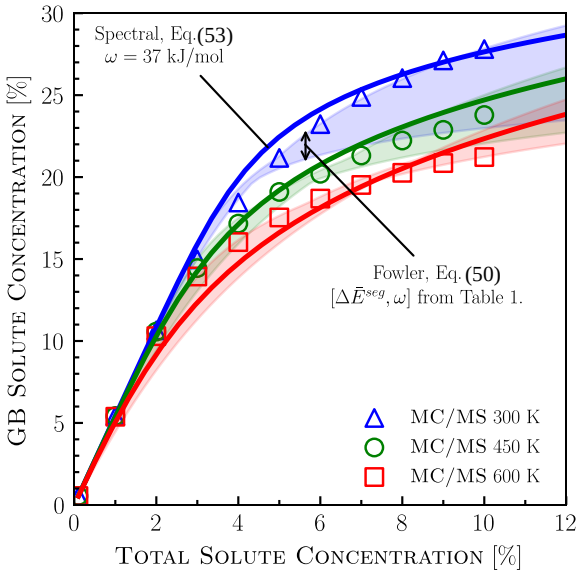

Figure 31: The predictions of the spectral model (ω = 37 kJ/mol) against MC/MS simulations at three different temperatures (300, 450, and 600 K); the shaded areas are the upper and lower bound of the Fowler-Guggenheim model, Eq. (50), using the three sets of best-fit parameters in Table 4, obtained by fitting each temperature independently.

By contrast, the spectral model better captures the true physics of GB segregation and therefore can extrapolate successfully beyond the conditions where it is calibrated. Figure 31 shows the predictions of Eq. (53) using the previously-calibrated fitting parameters ($\alpha = -1.1$, μ = 4 kJ/mol, σ = 19 kJ/mol and ω = 37 kJ/mol) with no recalibration for the two new temperatures considered; the fit is good across the full range. And Figure 32 reveals that the spectral model with interactions has an average error of less than 4%. We believe, therefore, that the two contributions of (i) site spectrality, and (ii) solute-solute interactions, represent the most important controlling physics of grain boundary segregation. The remaining errors in this approach are most likely due to the assumption of a Fowler-like average interaction term, which is the only component of Eq. (53) that does not come directly from a supported physical model. We briefly discuss this in the section that follows.

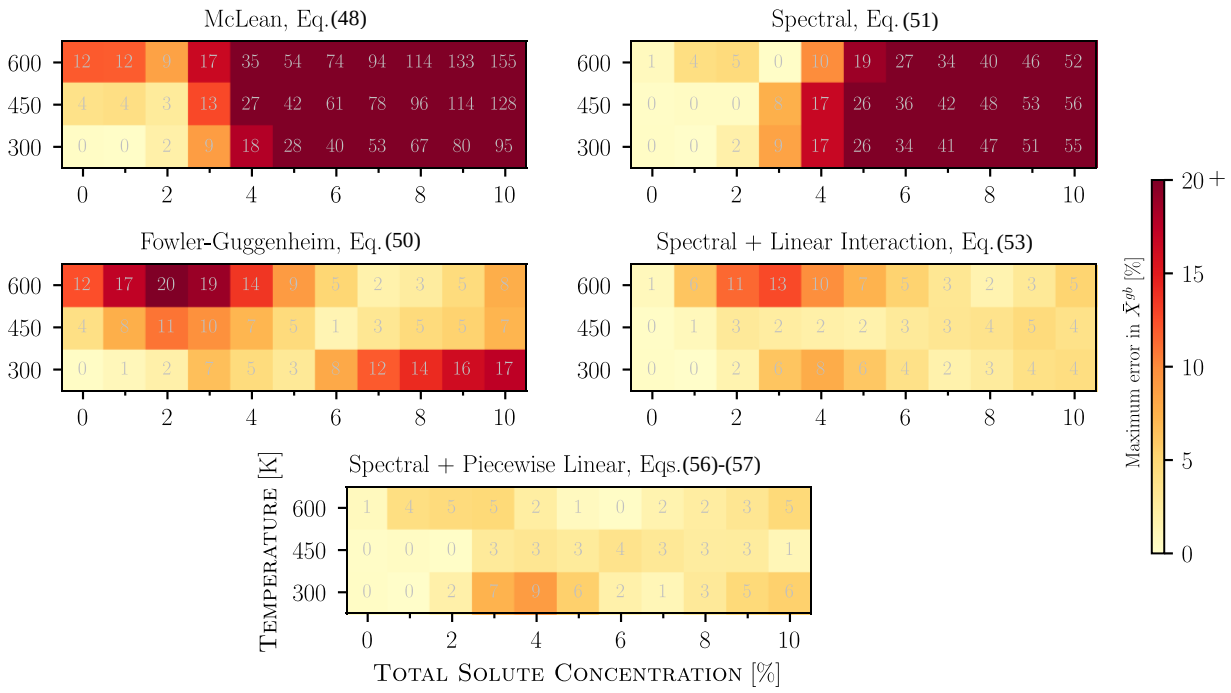

Figure 32: The maximum error in predictions of X^{gb} of the spectral and classic approaches with/without interaction, as compared to MC/MS simulations at 300, 450, and 600 K. For the classical approach (McLean and Fowler-Guggenheim), the plotted error is the maximum error using the three different sets of best-fit ($\Delta\bar{E}^{seg}$ and ω) listed in Table 4. The spectral model parameters are the same for any temperature: (α=-1.1, μ=-4 kJ/mol, σ=19 kJ/mol) for the distribution, ω = 37 kJ/mol for linear interactions. The Spectral (piecewise linear) is discussed in section 5.5.

5.5. Nonlinearity of Solute-Solute Interactions

In developing the spectral model, Eq. (53), we adopted the Fowler-Guggenheim approach of a mean-field approximation for solute-solute interactions, and added a linear interaction term, ωX^{gb}. Although a complete thermodynamic treatment should account for the spectrum of possible solute-solute interactions for all GB sites (~4×10^5 in our system), in practice, this is computationally challenging. Therefore, the linear (mean-field) form is enticing for its simplicity, and indeed, it does capture most of the missing physics as compared to using the spectral model alone, as seen in Figures 3, 5, and 6. However, interestingly, the spectral model without interactions ($\omega = 0$) actually performs *better* than the spectral model with linear interactions ($\omega = 36$ kJ/mol) for $X^{tot} \leq 2\%$ (approximately $X^{gb} \leq 10\%$), according to Figure 32. This implies that in the dilute limit, below about 10% solute concentration in the GB, there is no significant solute interaction, and thus adding an interaction term degrades the model. Put another way, the true segregation state

involves a non-linearity in the interaction term. Therefore, in this section, we re-examine the nature of the interaction term and more explicitly evaluate its form from our simulations, and whether another non-linear form of the mean-field approximation could be used.

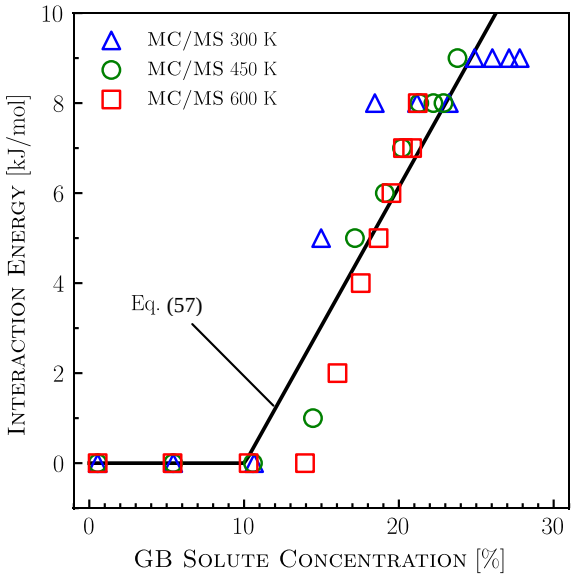

Figure 33: We fit Eq. (53) to hybrid MC/MS simulations of each X^{tot} independently, and obtain the magnitude of interaction energy required for the spectral model to have an absolute error of 1% in X^{gb}; the piecewise linear function (solid line), Eq. (57), is fitted to all data points, with ω=62 kJ/mol, and X_0=10%.

We first re-write the spectral model, Eq. (53), assuming no functional form for the interaction energy, ΔE^{ω}:

$$X^{tot} = \left(1 - f^{gb}\right)X^{c} + f^{gb} \int_{-\infty}^{\infty} F_i^{gb} \left[1 + \frac{1 - X^c}{X^c} \exp\left(\frac{\Delta E_i^{seg} + \Delta E^{\omega}}{kT}\right)\right]^{-1} d\Delta E_i^{seg} \qquad (56)$$

By fitting Eq. (53) to our hybrid MC/MS simulations we directly obtain ΔE^{ω} as a function of X^{gb} for each X^{tot} independently, as shown in Figure 33. Clearly, a linear Fowler-like form for $\Delta E^{\omega}(X^{gb})$ is invalid. Instead, we observe two regions for solute-solute interactions, discussed in turn below.

First, we identify a non-interaction region for $X^{gb} \leq 10\%$, where solute-solute interactions are negligible. In this region, the spectral approach ($\omega = 0$) captures all the essential physics of GB segregation, as was shown earlier in Figure 29, where the model correctly predicts the equilibrium

segregation state up to $X^{gb} = 10\%$. Therefore, a threshold of solute content at the GB is required before solute atoms can "see" each other and interact – in this case, $X^{gb} = 10\%$. This speaks to the physical spacing amongst the most energetically favorable segregation sites. Intuitively, one expects nature to space out the GB defect sites that can most easily accommodate solutes. For example, rarefied low-density regions would self-avoid due to their interacting hydrostatic tensile strain fields, and spread out in the grain boundary network; by extension, the first solutes to segregate would take on a nonrandom spacing to minimize interactions.

This notion is explored in Figure 34(a) for $X^{gb} = 5\%$, where we plot the distribution of nearest-neighbor solute spacings for the true equilibrium configuration, in comparison to a random distribution. It is clear that in equilibrium, segregated solute atoms are spaced further apart than expected for a random distribution; beyond simply a dilute-limit separation, the system has a built-in physical preference for solute-solute separations. Many atoms shift from the first peak in Figure 34(a) to the second, a physical separation increase from ~3 to ~5 Å, over which more than 75% of the interaction energy is lost based on the interatomic potential. In fact, the segregated atoms on average have no interactions with more than one other solute atom, as shown in Figure 34(b), where the average distance to the N^{th} nearest neighbors is plotted. The second nearest neighbor is at more than 6Å, which is beyond the interaction range for the embedded atom potential (~5 Å) [67]. Close inspection of Figure 28(c) agrees with this line of reasoning as well; there is a significant tendency for solutes to spread out and surround themselves mostly with solvent atoms. Such considerations can explain why up to 10% Mg can populate the grain boundary with no need to account for solute-solute interactions. Accordingly, in future work, the definition of the dilute limit should likely be adjusted based on a better understanding of site spectrality and its physical distribution.

Second, at higher concentrations where solute-solute interactions set on, we observe a roughly linear interaction region in Figure 33 ($X^{gb} > 10\%$). Note that this linear range is quite different from the Fowler form because it is offset on the concentration axis from the origin; no Fowler approximation would capture this trend without the inclusion of the offset from the origin. What is more, a strictly linear interaction is not expected using an embedded atom potential. The apparent simplicity of the average interaction in Figure 33, therefore, suggests that in this

composition range there is some solute organization that prevails despite the complexity of the segregation site spectrum and solute-solute interactions.

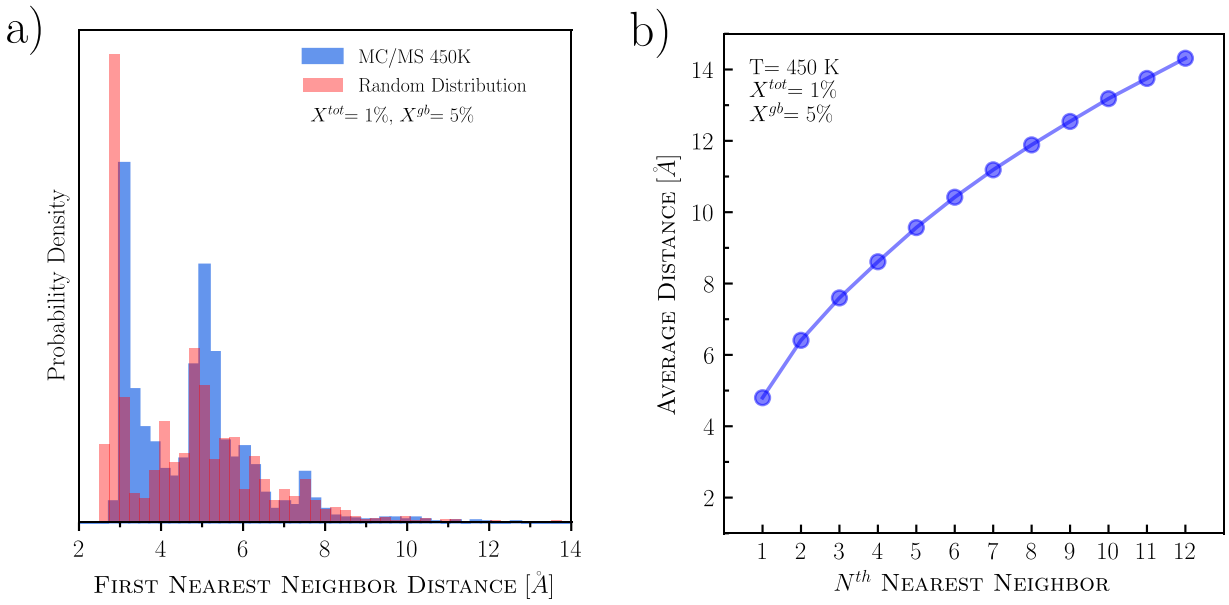

Figure 34: (a) The distribution of the distance to first nearest neighbors for solute atoms segregated at the GB for $X^{tot} = 1\%$ ($X^{gb} = 5\%$) at 450K, compared to a random solute distribution with the same X^{gb}. (b) The average distance to N^{th} nearest neighbors for the same sample; beyond ~5 Å, the Mg-Mg interactions are negligible for the embedded atom potential [67].

All of the above aspects of solute interaction are worthy of further exploration, and it would appear that relatively little literature on such topics yet exists; we leave these studies for future research. In any event, it seems clear that in the future the best isotherm for GB segregation will certainly involve a more complex interaction model that incorporates some of the above ideas. In the absence of any first-principles motivation for an interaction model, we find that a simple piecewise linear form that captures the two regimes above provides an even better functional fit to the true segregation state:

$$\Delta E^{\omega}(X^{gb}) = \begin{cases} 0 & if\ X^{gb} \le X_0 \\ \omega(X^{gb} - X_0) & if\ X^{gb} > X_0 \end{cases} \quad (57)$$

Here X_0 defines the onset of the linear interactions region. A best-fit of Eq. (57) for all data points of hybrid MC/MS simulations is shown in Figure 33 (solid line), with $\omega = 62$ kJ/mol, and $X_0 = 10\%$. The piecewise-linear model takes advantage of the predictive ability of the spectral model

without interactions below $X^{gb} = 10\%$, and gives a better overall fit across the composition-temperature space, and the lowest errors, of all the models so far (less than 3%) for X^{gb} predictions as shown in Figure 32. We look forward to future developments on the nature of solute-solute interactions that can lead to improved and more physically-motivated models to incorporate with the spectral model.

5.6. Conclusion

In conclusion, we have decoupled the effects of both the spectrality of GB sites and solute-solute interactions on the concentration dependence of solute segregation at GBs in a polycrystal, and cast both effects into a simple thermodynamic model, Eq. (53), that correctly predicts the equilibrium GB segregation state in a binary alloy across the composition-temperature space. The model requires only four fitted parameters, which are easily extractable using atomistic simulations – three to represent the skew-normal function of the distribution and one to represent solute-solute interactions. We have shown, for the first time, that the failure of McLean-type models beyond the dilute limit is due to two factors, first, the spectrality of the GB, and second, solute-solute interactions; this is different from the prevalent understanding in the literature, where the failure is solely attributed to solute-solute interactions – the Fowler-Guggenheim approach. We propose that in the future, researchers should use more than just the two parameters required by "averaged" models, to correctly characterize GB segregation in a binary alloy with a spectrum of sites.

6. Future Work Directions

In this thesis, we outlined the proper thermodynamic framework for GB solute segregation in polycrystals, which take into account the spectrum of atomic environments at the GB network, and the variation in their tendencies to accommodate solute atoms. We elucidated the nature of this spectrum for over 250 alloys, using a machine learning framework. Throughout the analysis, we encountered many interesting questions that are worthy of future explorations that can further improve the current spectral approach to GB solute segregation, which we hope to be widely adopted in the future by the research community. These questions include:

Contributions of Vibrational Entropy

The proposed spectral framework for GB solute segregation accounts for the configurational component of entropy, but ignores the vibrational component, and assumes it is negligible. However, for some alloys, this assumption might be invalid, especially at elevated temperature. This is indicated by previous studies of GB solute segregation in CSL GBs, where, at elevated temperatures, the vibrational component was shown to be of a similar magnitude to the configurational one. We thus expect a similar effect for polycrystals, and, as the vibrational entropy is site-type dependent i.e. the vibrations of a solute atom will be a function of its local atomic environment at the GB, we expect a spectrum for the vibrational entropies of solute segregation in a polycrystal. *Future work*: What is the nature of this spectrum? How does it vary across the alloy space? and How to efficiently compute it?

Interstitial Solute Segregation

Throughout the thesis, we assumed that solute atoms only substitutionally segregate at the GB. However, as the GB environment is disordered in nature, it is possible in principle for solute atoms to also favorably segregate interstitially at the boundary. Similar to the substitutional spectrum elucidated here, we expect a spectrum for interstitial segregation energies. The nature of this spectrum and its correlation with the substitutional spectrum will determine the equilibrium segregation at the GB. *Future work*: How to extend the current models to account for possible interstitial solute segregation at the GB? What is the nature of the spectrum of interstitial solute segregation at the GB in polycrystal? And how does it vary across the alloy space?

Validating Interatomic Potentials

In Chapter 3, we showed that the computed GB segregation spectra are sensitive to the choice of interatomic potential. For the same alloy system, we can get predictions that range from the GB network being highly favorable to completely unfavorable to solute segregation. The natural question to follow is which one should we trust? Currently, there is no clear answer to that. *Future work*: How to test and validate interatomic potentials for the study of GB solute segregation? The end goal should be to develop a quantifiable metric that measures the accuracy of an interatomic potential for the problem.

Learning from Ab-initio Methods

Aside from the concerns about accuracy, the availability of interatomic potentials is a major limiting factor. For example, there are no alloy potentials for the metals Ir, Os, Sc. And, even for widely studied metals, such as Al, there are only potentials for 19 solutes – a small subset of metals. This effect is illustrated in Supplementary Fig. 1, where much of the alloy space is empty, or covered by a single interatomic potential that is not fitted directly to alloy properties. And though, an ideal goal is to develop accurate interatomic potentials for more alloys, this is a resource intensive task, that is not economical (or even possible in a reasonable time) for the purpose of screening, i.e. we expect potential development to be reserved to post-screening efforts in materials science generally for years to come. In Chapter 3, we developed a learning framework that can faithfully reproduce the segregation spectrum of an alloy, using only 100 GB environments. *Future work*: Can we extend the learning framework to learn directly from ab initio methods e.g. density functional theory calculations? And completely bypass the need for interatomic potentials? at least for the purpose of screening.

Ternary and Higher Order Alloys

In this thesis, we have only examined binary alloys. However, in practice, alloys are rarely binary, but rather multinary, as multiple solute additions expand the alloy design space, and gives more opportunities for fine tuning the alloy properties. Therefore, a major future direction is to extend the current framework to handle ternary, and higher order alloys. *Future work*: How to extend the spectral model to treat ternary alloys? Can we use the current binary segregation spectra to design ternary and higher alloys? Is it possible to generate similar segregation spectra database

through machine learning for higher order alloys? And finally, what is the nature of solute-solute interactions? and, how to account for it?

Appendix A: Spectral Segregation Database

A.1. Segregation Spectra

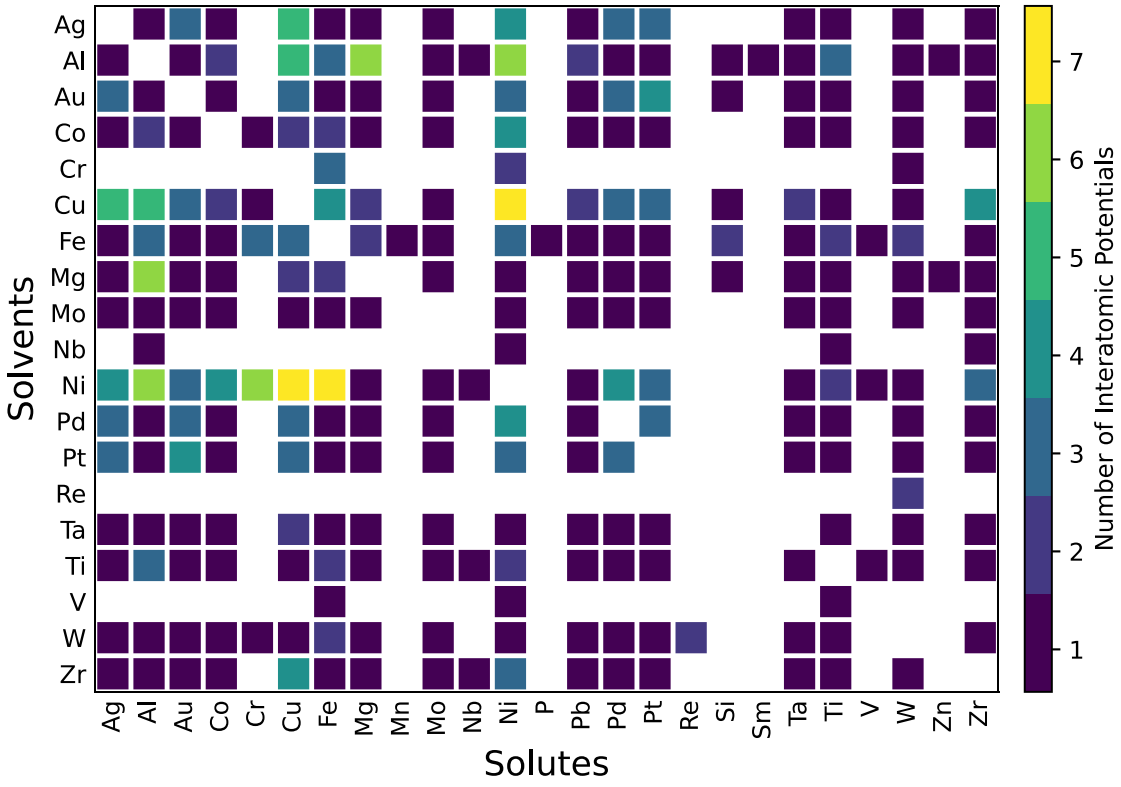

Supplementary Fig. 1: All surveyed binary alloys and their existing interatomic potentials – a total of 260 alloys and 434 combinations of interatomic potentials. We sought to report all interatomic potentials without judging their relevance to segregation studies, but we 1) limited solvents to bcc, fcc, and hcp metals, and 2) removed H, C, O, U, Xe solutes, and 3) excluded interatomic potentials that do not correctly predict the equilibrium 0 K lattice structure for the solvent, e.g. fcc Fe instead of bcc Fe.

A.1.1. Ag-based alloys

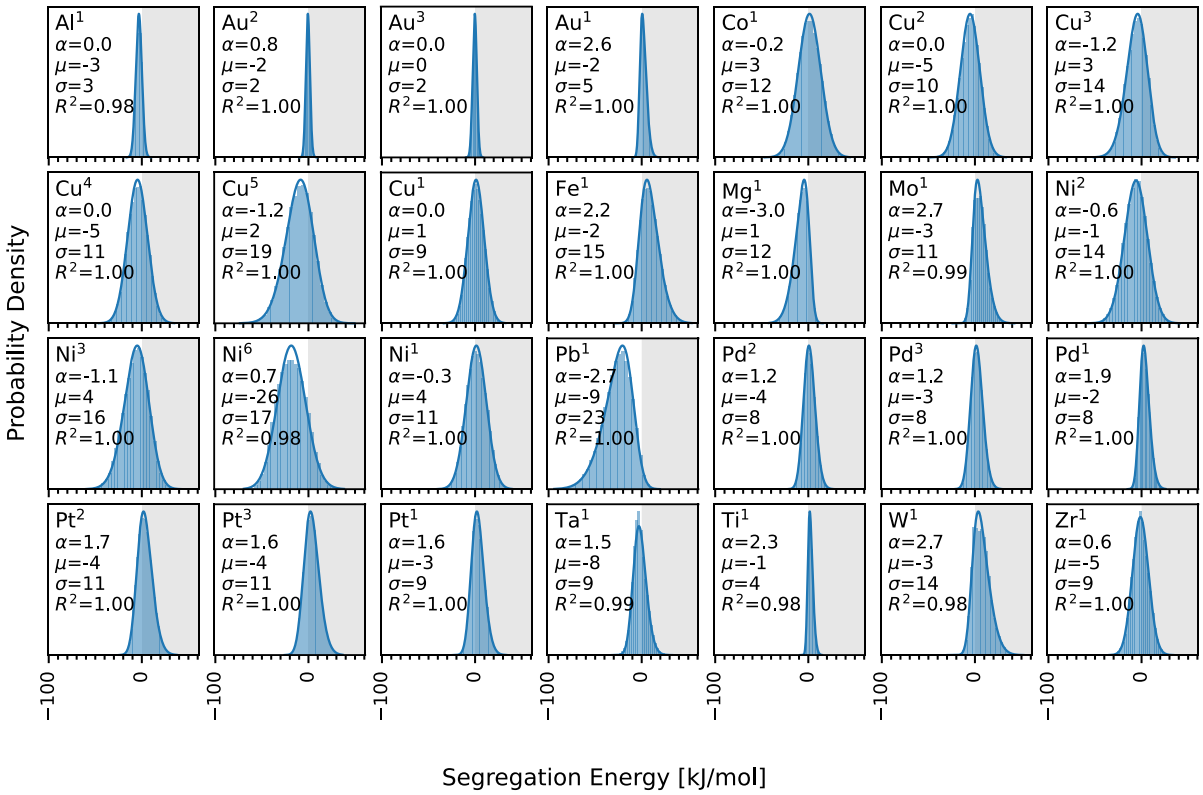

Supplementary Fig. 2: Solute segregation spectra at GBs in Ag-based alloys. References for potential identifiers (superscript to solute) are in Supplementary Table 1.

A.1.2. Al-based alloys

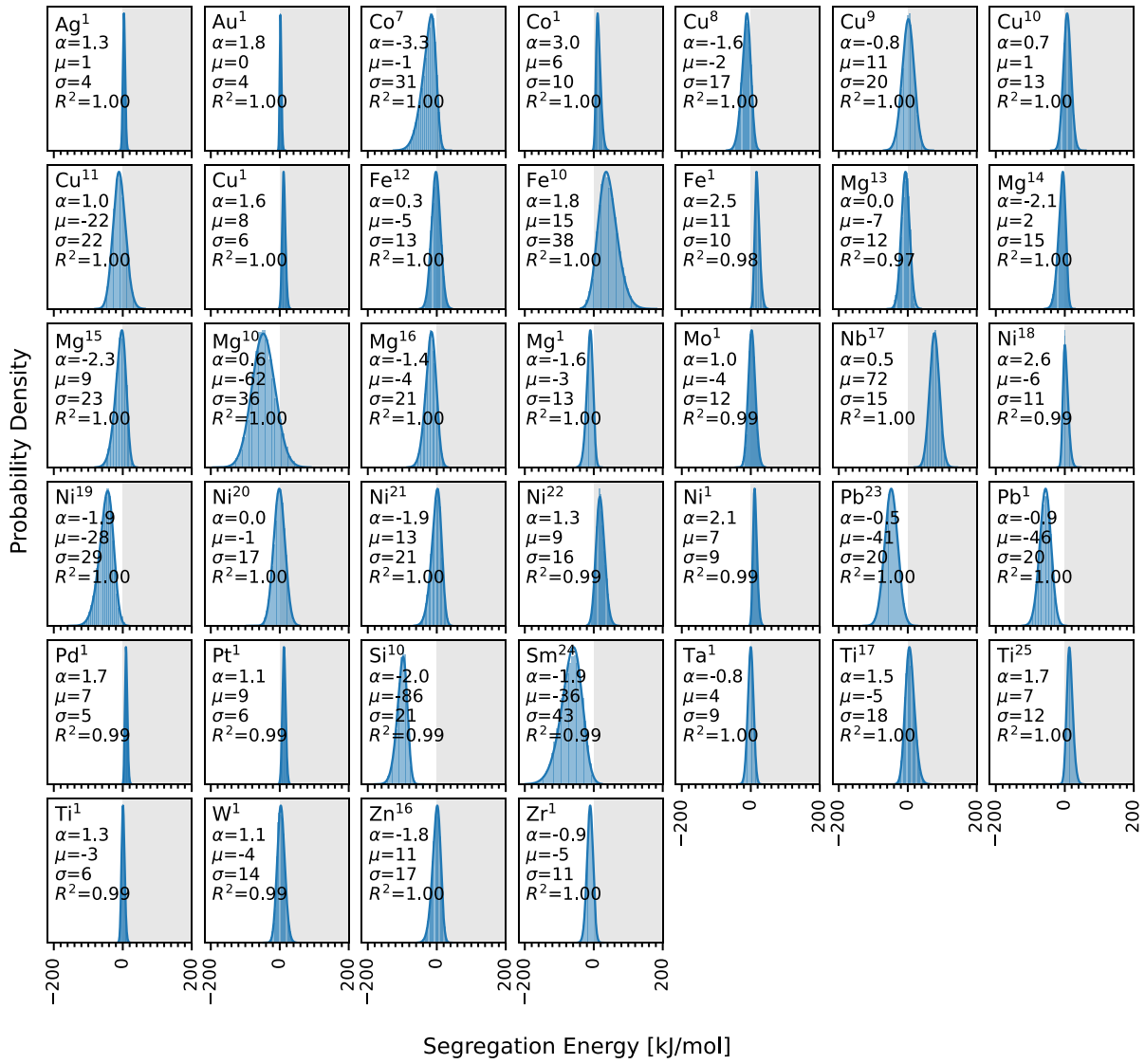

Supplementary Fig. 3: Solute segregation spectra at GBs in Al-based alloys. References for potential identifiers (superscript to solute) are in Supplementary Table 1.

A.1.3. Au-based alloys

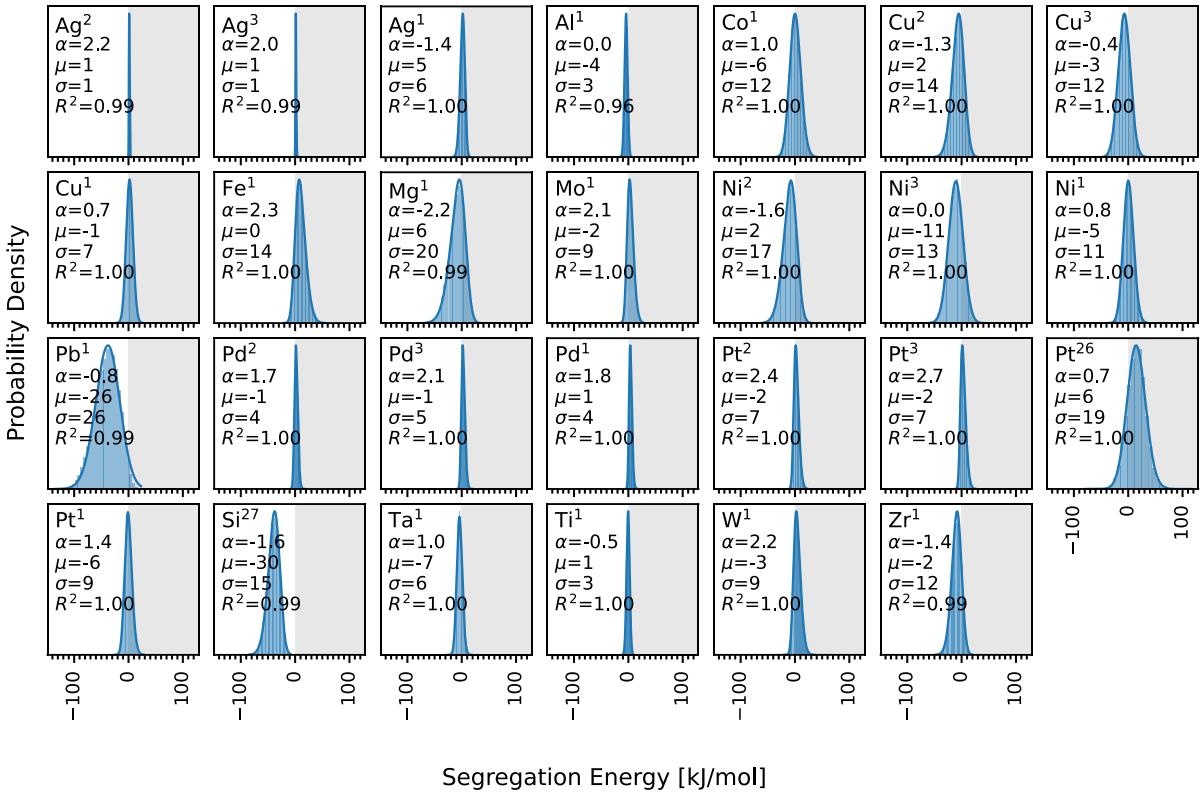

Supplementary Fig. 4: Solute segregation spectra at GBs in Au-based alloys. References for potential identifiers (superscript to solute) are in Supplementary Table 1.

A.1.4. Co-based alloys

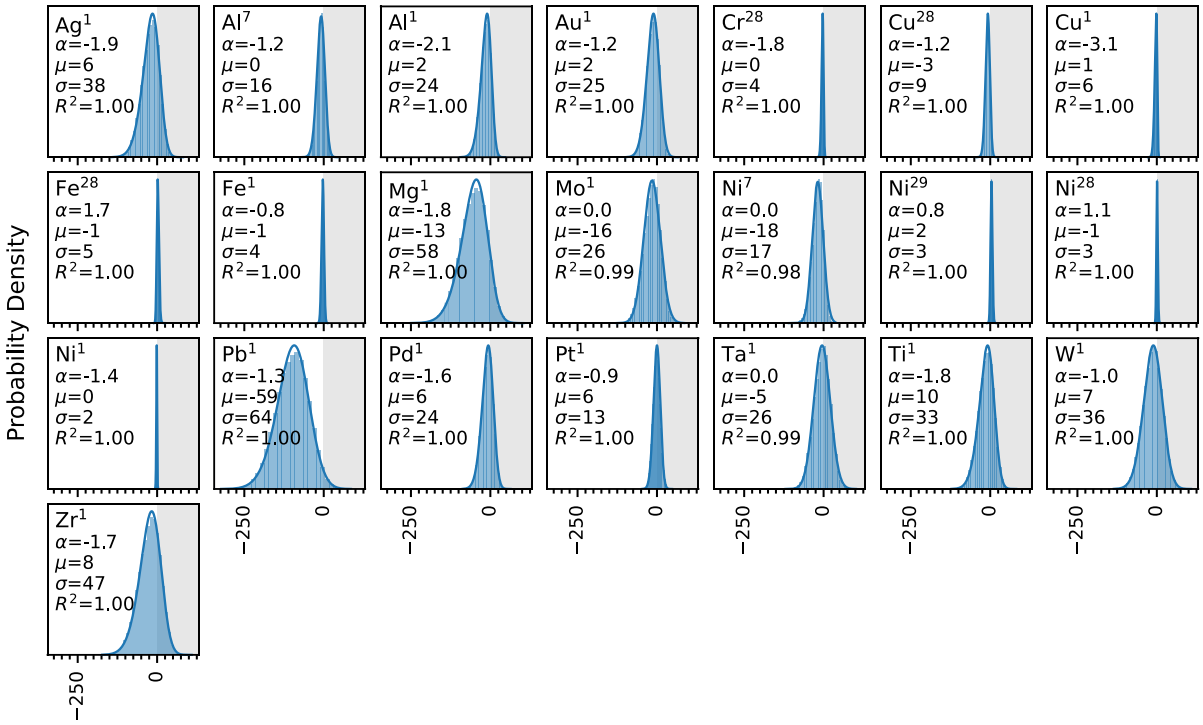

Supplementary Fig. 5: Solute segregation spectra at GBs in Co-based alloys. References for potential identifiers (superscript to solute) are in Supplementary Table 1.

A.1.5. Cr-based alloys

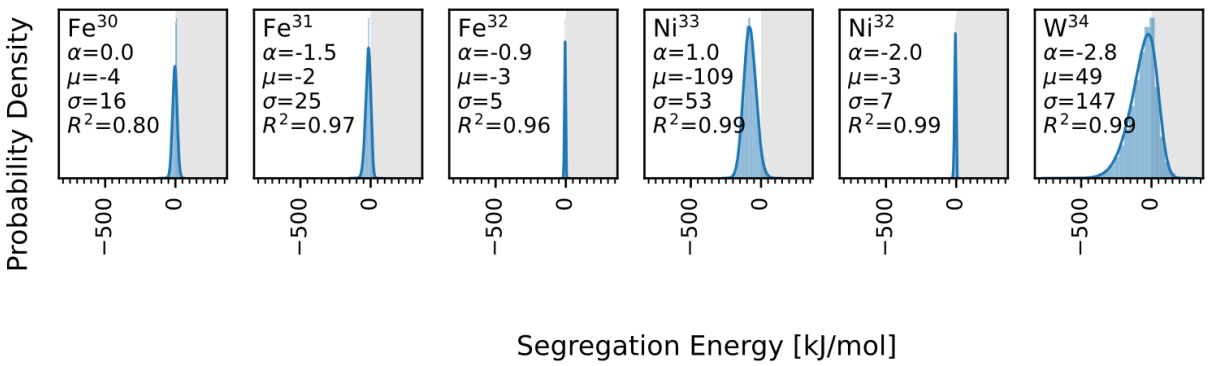

Supplementary Fig. 6: Solute segregation spectra at GBs in Cr-based alloys. References for potential identifiers (superscript to solute) are in Supplementary Table 1.

A.1.6. Cu-based alloys

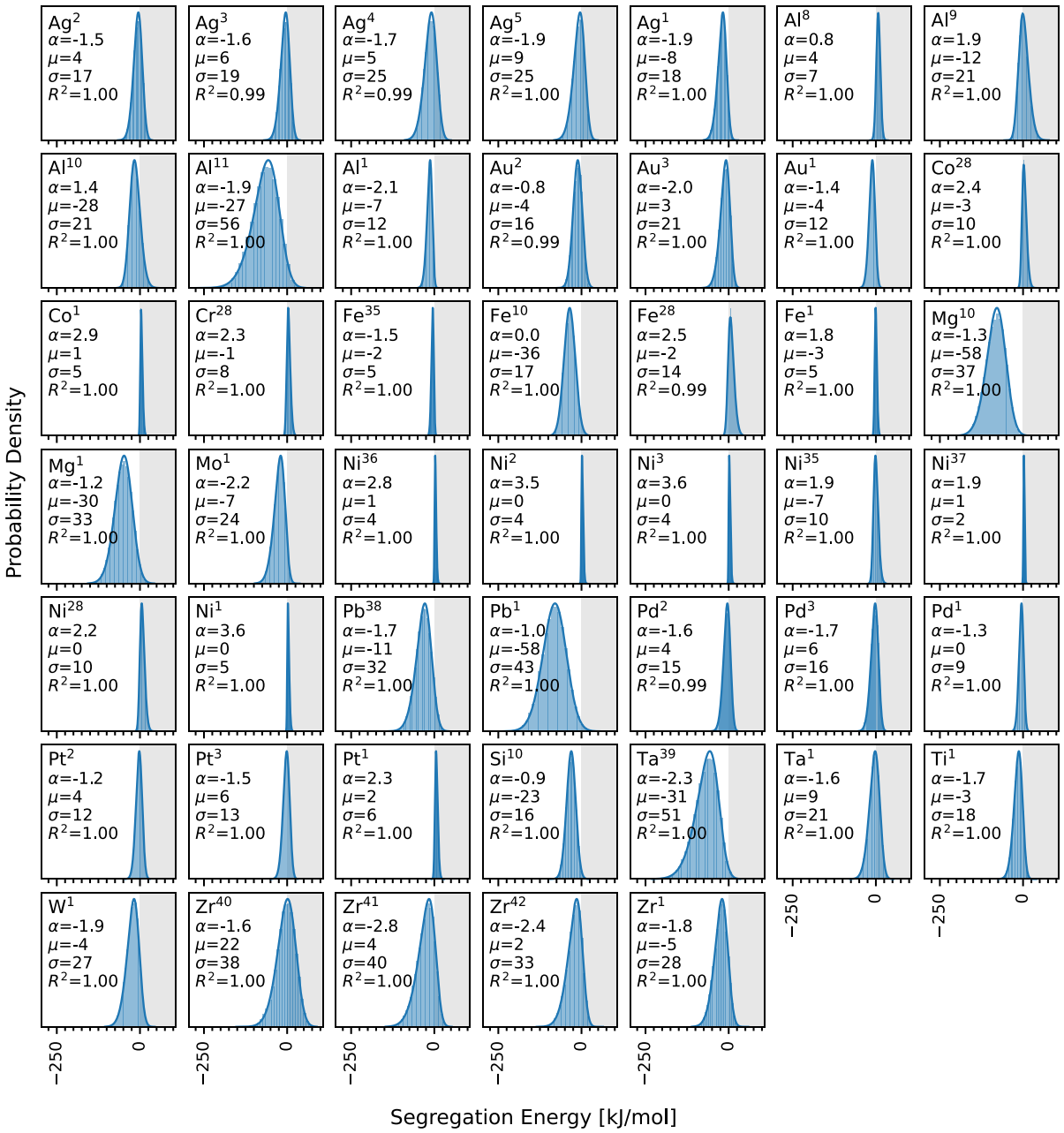

Supplementary Fig. 7: Solute segregation spectra at GBs in Cu-based alloys. References for potential identifiers (superscript to solute) are in Supplementary Table 1.

A.1.7. Fe-based alloys

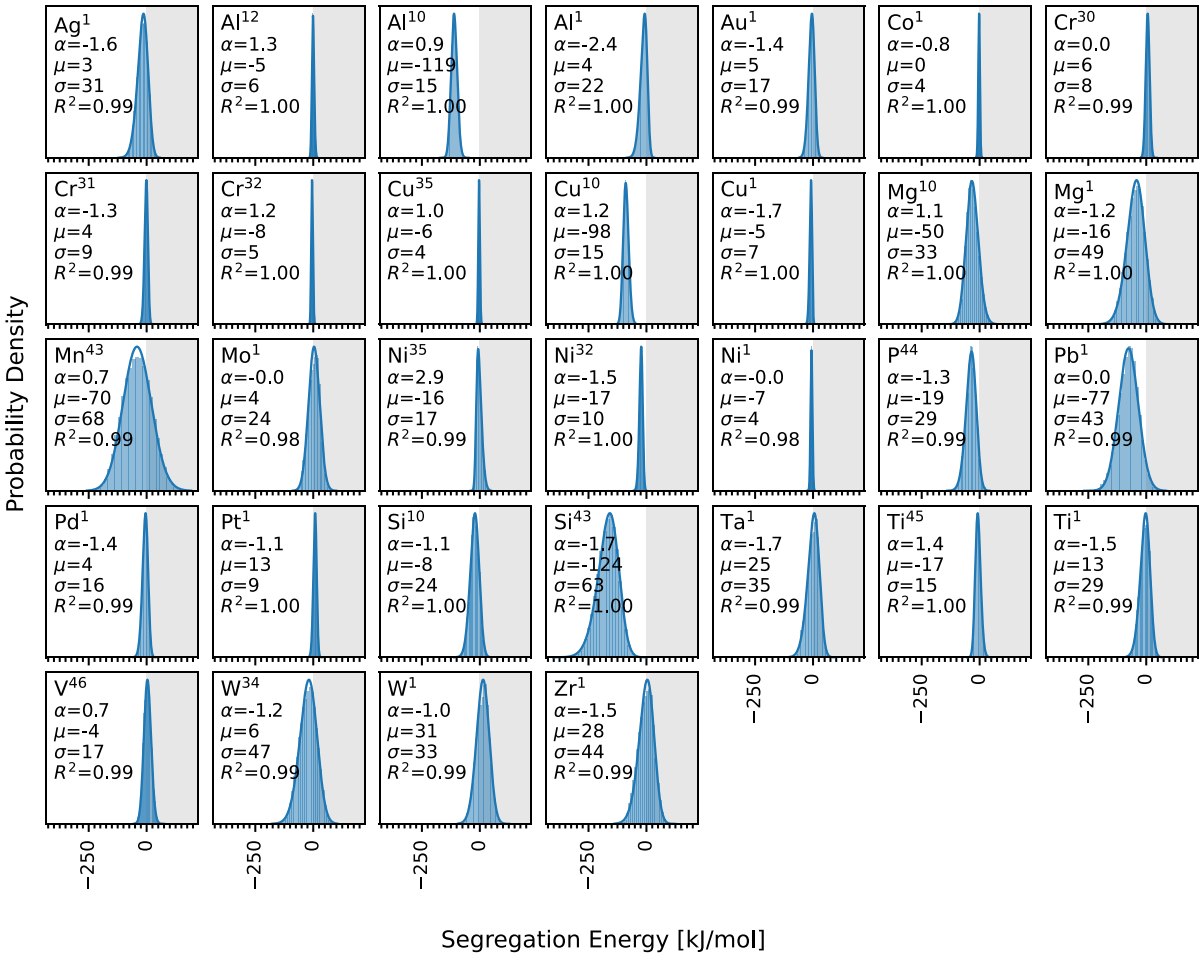

Supplementary Fig. 8: Solute segregation spectra at GBs in Fe-based alloys. References for potential identifiers (superscript to solute) are in Supplementary Table 1.

A.1.8. Mg-based alloys

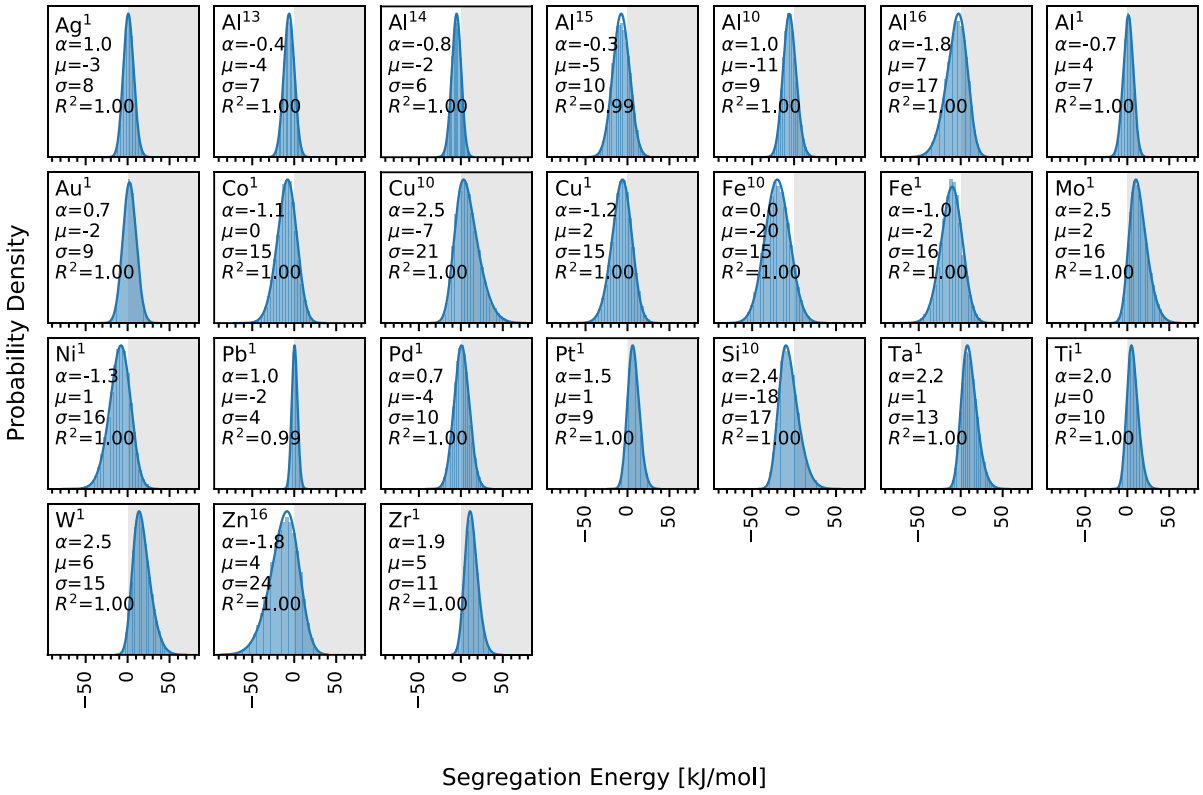

Supplementary Fig. 9: Solute segregation spectra at GBs in Mg-based alloys. References for potential identifiers (superscript to solute) are in Supplementary Table 1.

A.1.9. Mo-based alloys

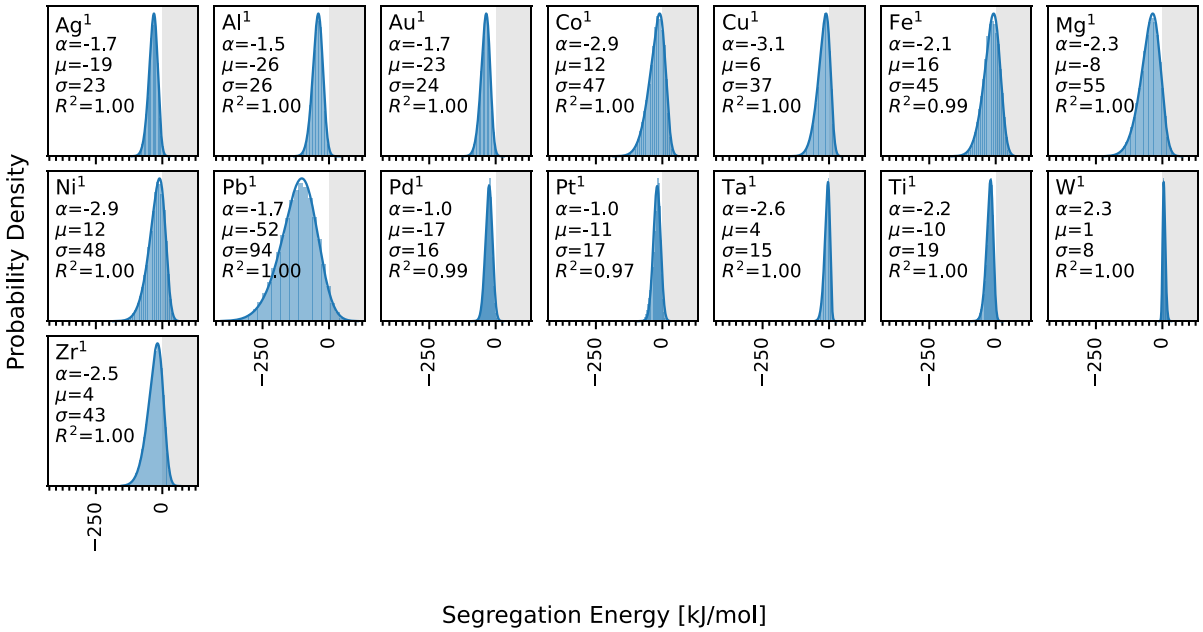

Supplementary Fig. 10: Solute segregation spectra at GBs in Mo-based alloys. References for potential identifiers (superscript to solute) are in Supplementary Table 1.

A.1.10. Nb-based alloys

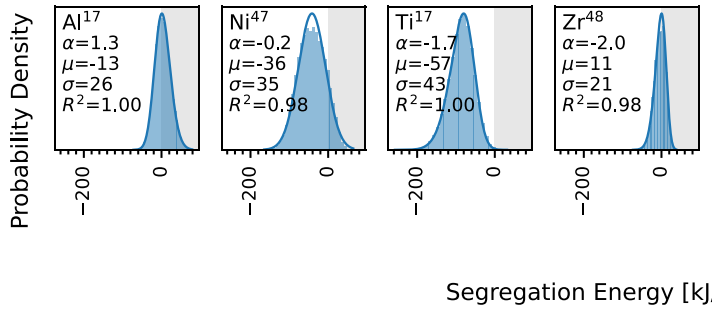

Supplementary Fig. 11: Solute segregation spectra at GBs in Nb-based alloys. References for potential identifiers (superscript to solute) are in Supplementary Table 1.

A.1.11. Ni-based alloys

Supplementary Fig. 12: Solute segregation spectra at GBs in Ni-based alloys. References for potential identifiers (superscript to solute) are in Supplementary Table 1.

A.1.12. Pd-based alloys

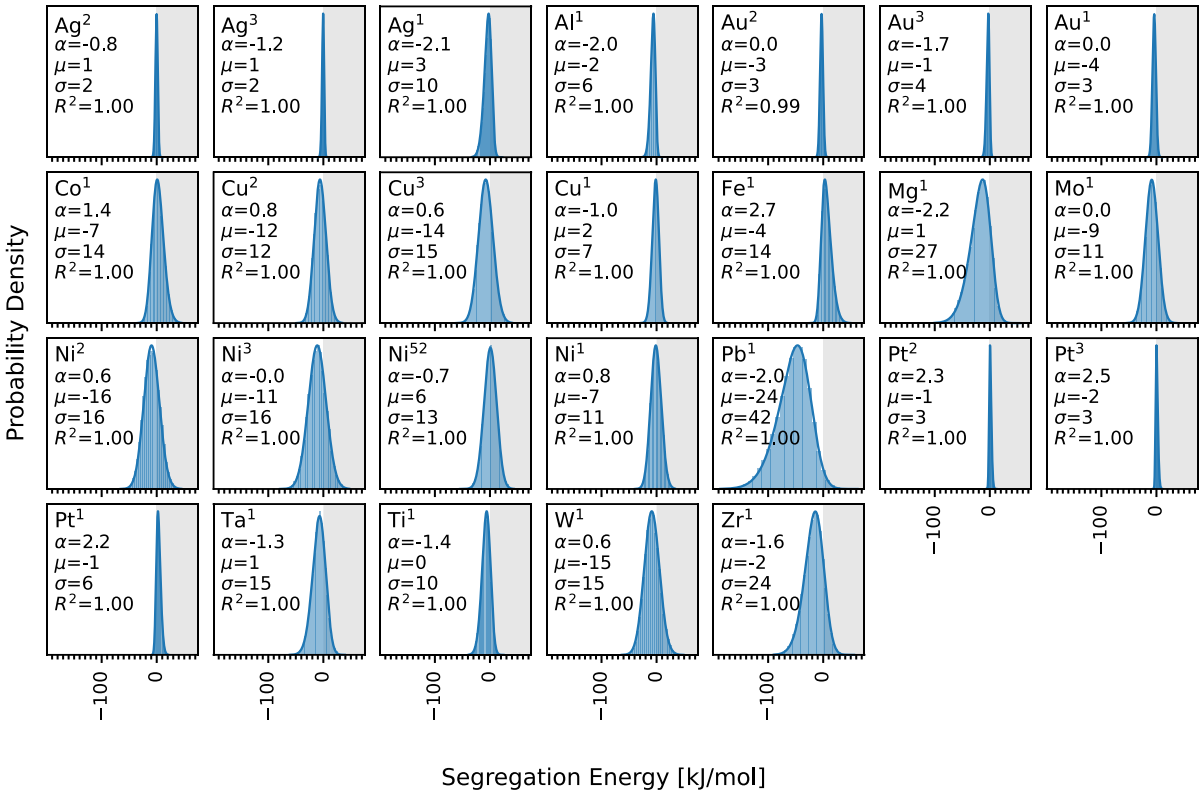

Supplementary Fig. 13: Solute segregation spectra at GBs in Pd-based alloys. References for potential identifiers (superscript to solute) are in Supplementary Table 1.

A.1.13. Pt-based alloys

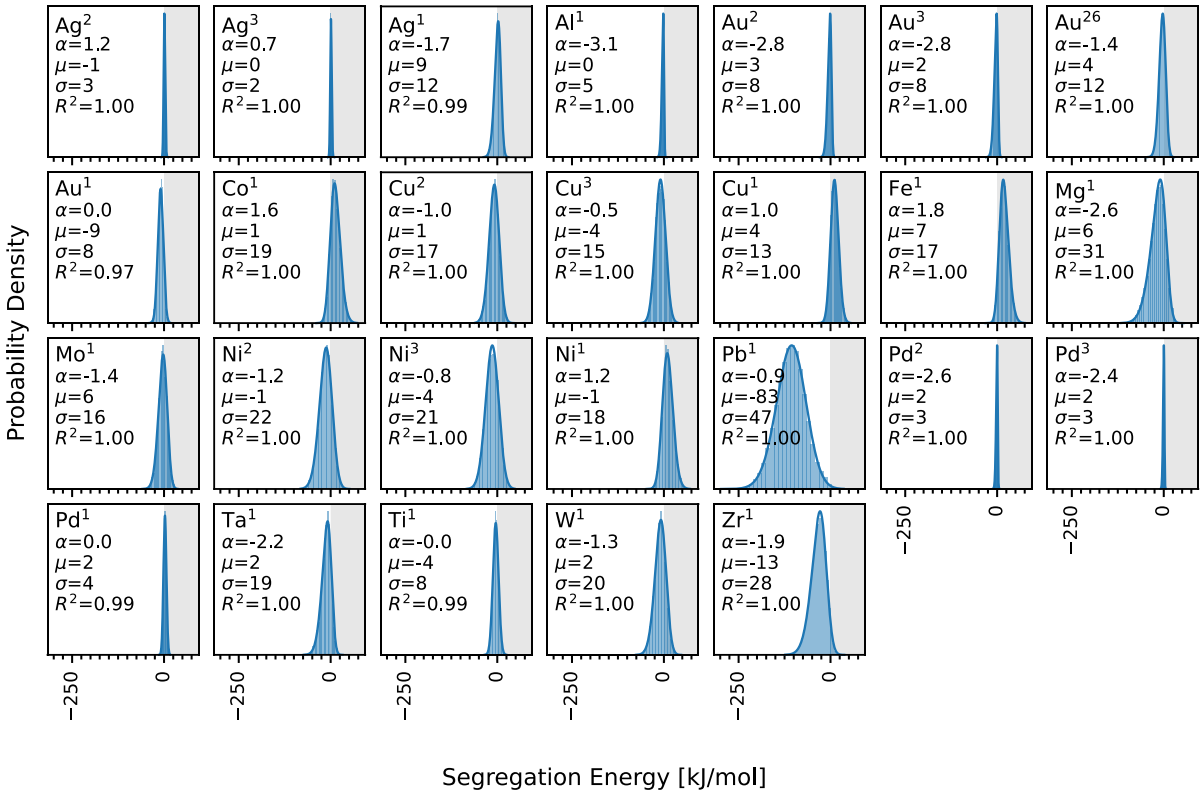

Supplementary Fig. 14: Solute segregation spectra at GBs in Pt-based alloys. References for potential identifiers (superscript to solute) are in Supplementary Table 1.

A.1.14. Re-based alloys

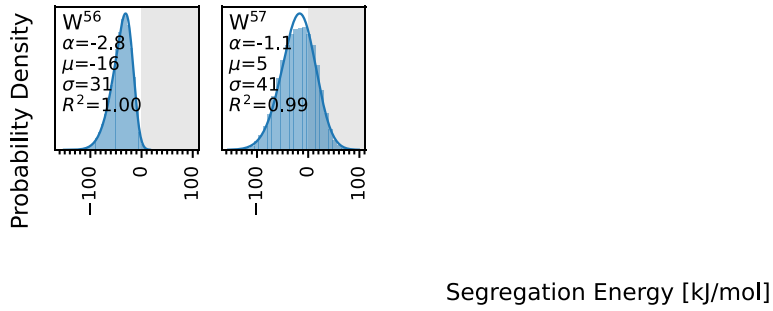

Supplementary Fig. 15: Solute segregation spectra at GBs in Re-based alloys. References for potential identifiers (superscript to solute) are in Supplementary Table 1.

A.1.15. Ta-based alloys

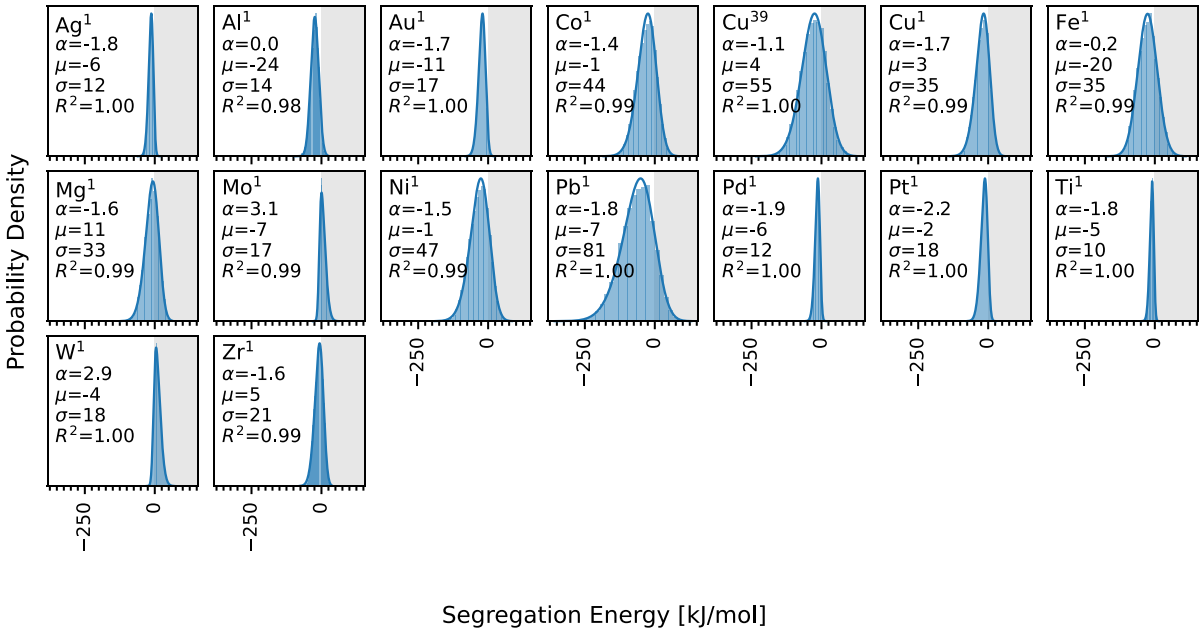

Supplementary Fig. 16: Solute segregation spectra at GBs in Ta-based alloys. References for potential identifiers (superscript to solute) are in Supplementary Table 1.

A.1.16. Ti-based alloys

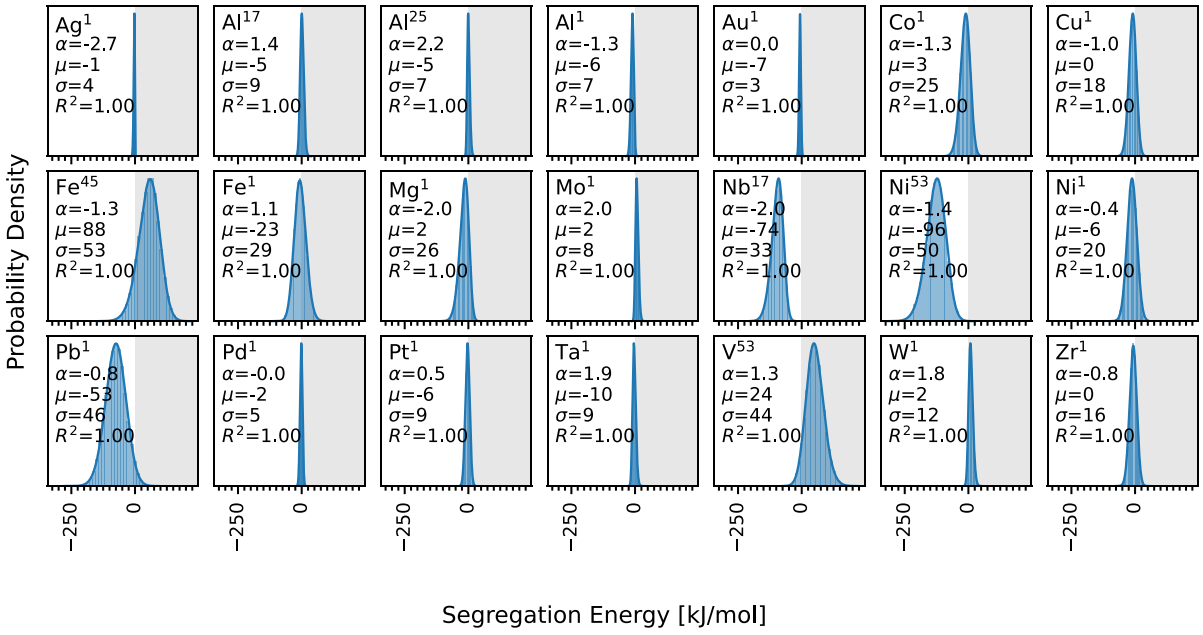

Supplementary Fig. 17: Solute segregation spectra at GBs in Ti-based alloys. References for potential identifiers (superscript to solute) are in Supplementary Table 1.

A.1.17. V-based alloys

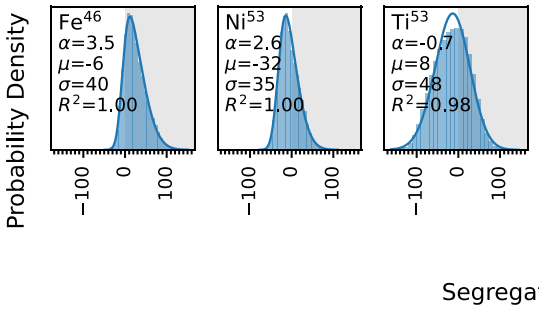

Supplementary Fig. 18: Solute segregation spectra at GBs in V-based alloys. References for potential identifiers (superscript to solute) are in Supplementary Table 1.

A.1.18. W-based alloys

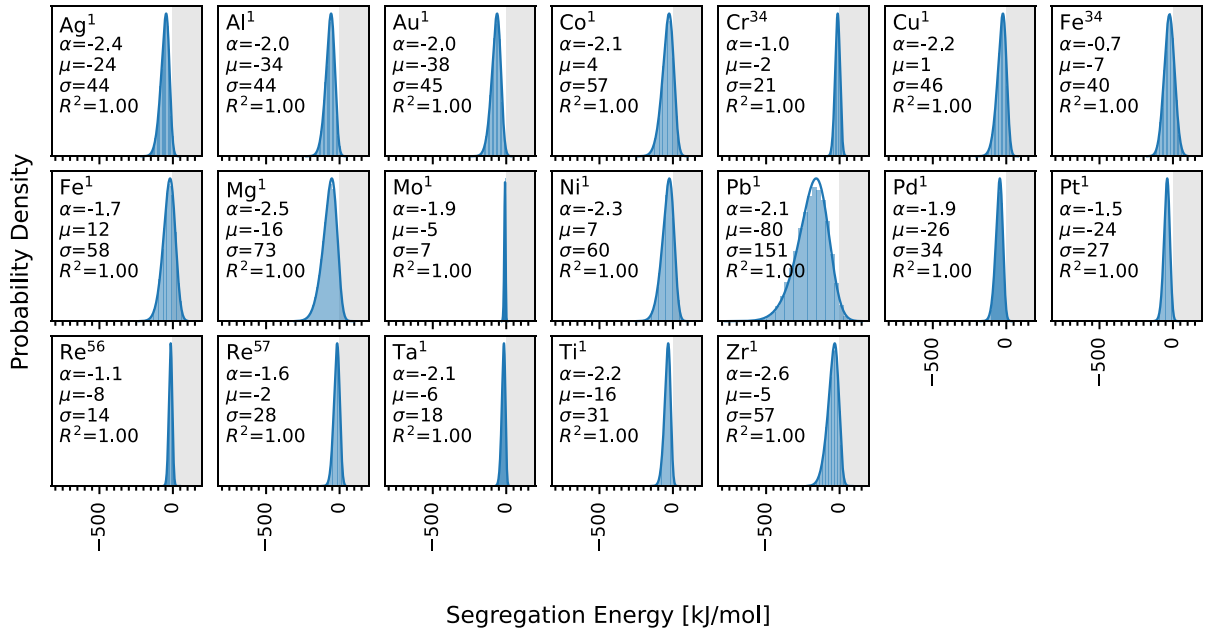

Supplementary Fig. 19: Solute segregation spectra at GBs in W-based alloys. References for potential identifiers (superscript to solute) are in Supplementary Table 1.

A.1.19. Zr-based alloys

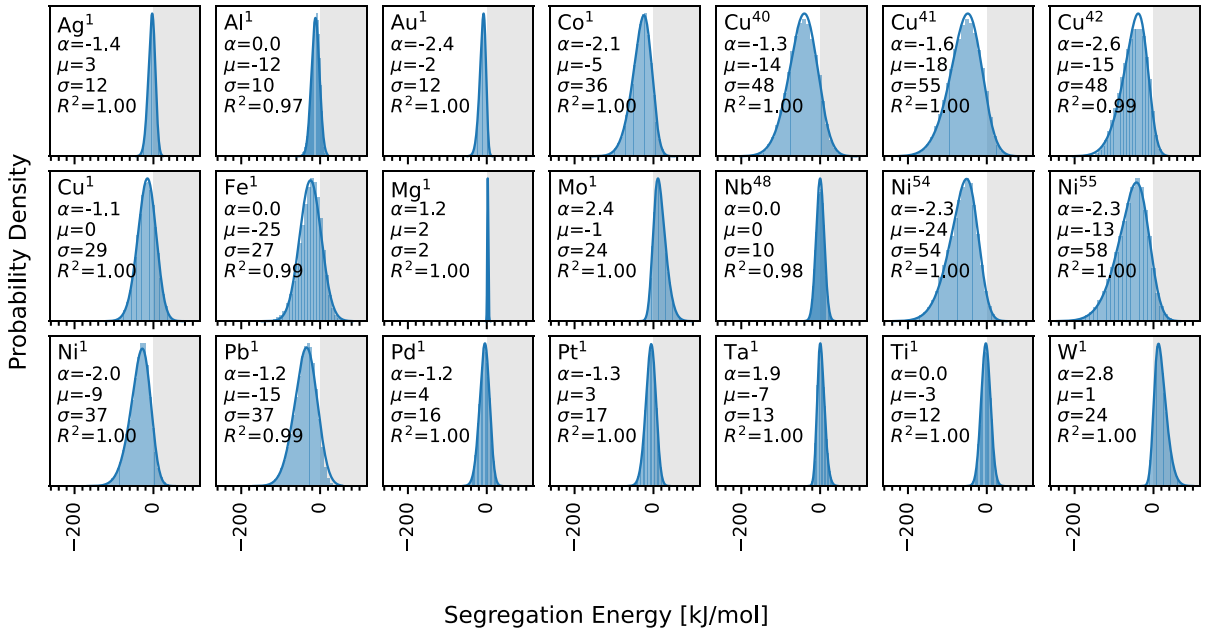

Supplementary Fig. 20: Solute segregation spectra at GBs in Zr-based alloys. References for potential identifiers (superscript to solute) are in Supplementary Table 1.

A.2. Segregation Data Analysis

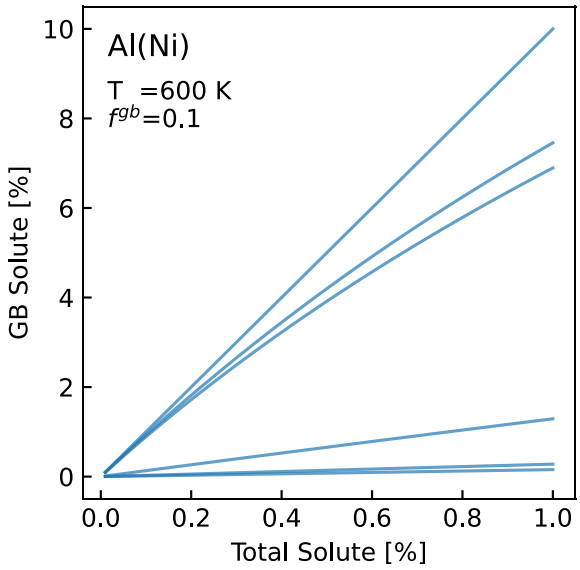

Supplementary Fig. 21: Predictions of GB solute segregation for the different Al(Ni)[111,118,122,180,181,224] Interatomic potentials in a polycrystal of average grain size 15 nm (f^{gb} ≈10%) at T = 600 K; even at a low total solute concentration of 1%, the predictions for X^{gb} can widely vary from 0.2% to 10%.

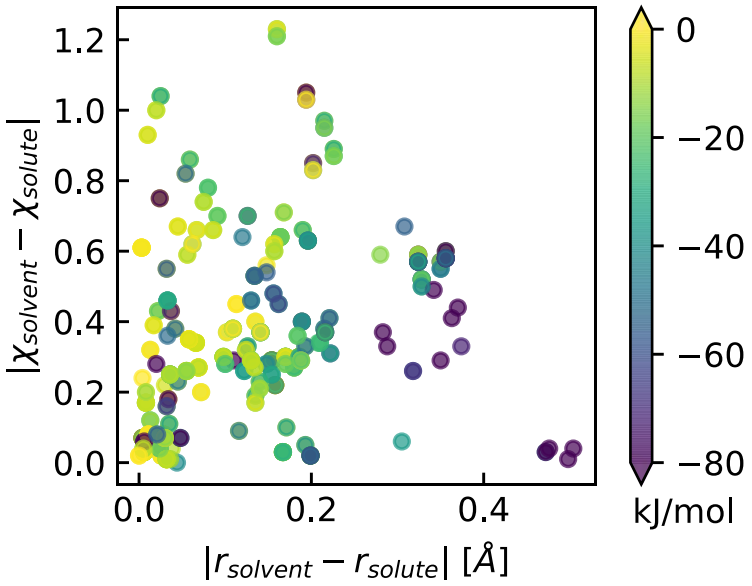

Supplementary Fig. 22: Predictions for the segregation tendency (25th percentile value) as a function of the difference in Pauling electronegativity (χ) and metallic radii (r).

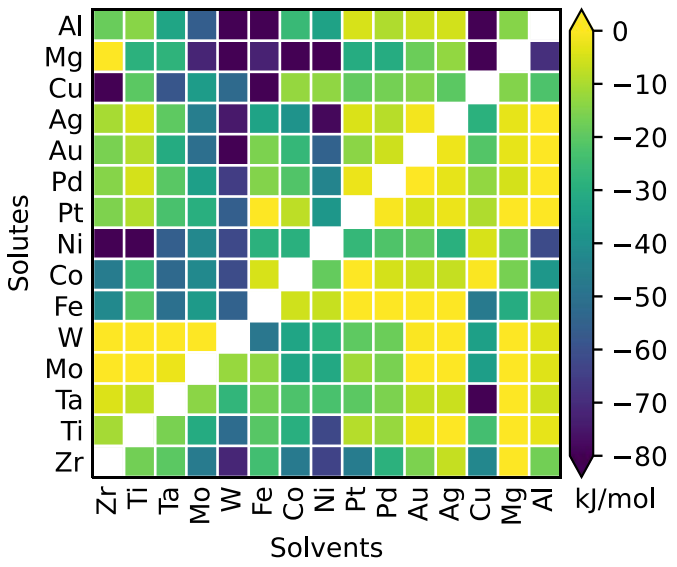

Supplementary Fig. 23: An alternate version of the Pettifor-type map in Fig.6. for the predicted segregation tendency across the alloy space, using interatomic potentials that has the most segregating spectra.

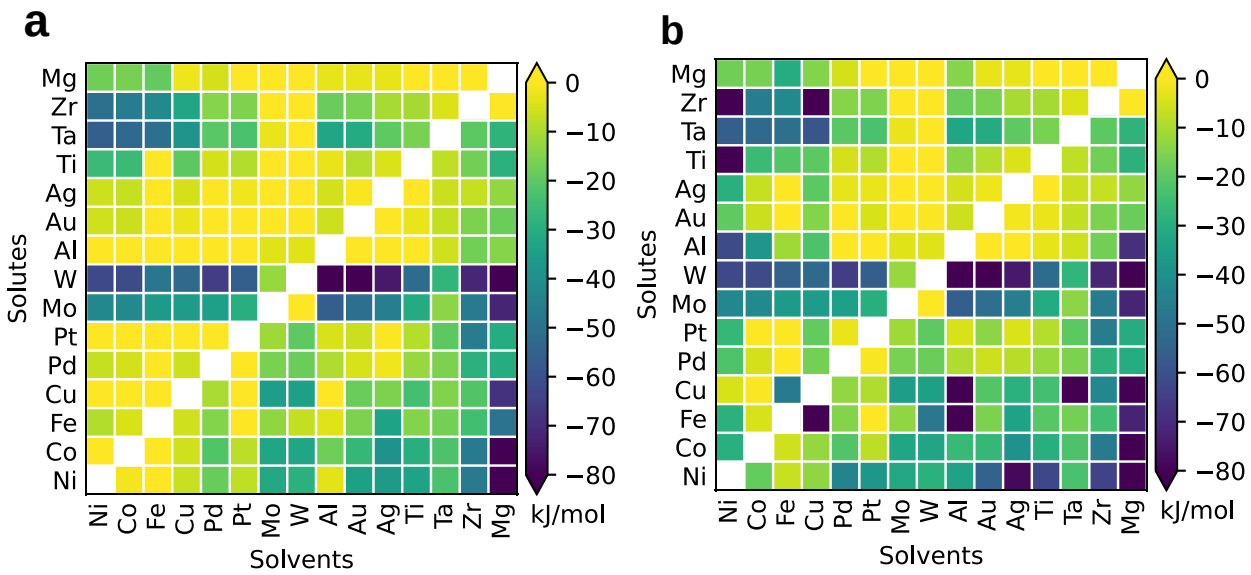

Supplementary Fig. 24: Predictions for the segregation tendency (quantified by the 25th percentile value) across the alloy space, with elements arranged by increasing metallic radii: Ni (smallest) → Mg (largest); for alloys with multiple potentials, we report (a) the least segregating spectra and (b) the most segregating spectra.

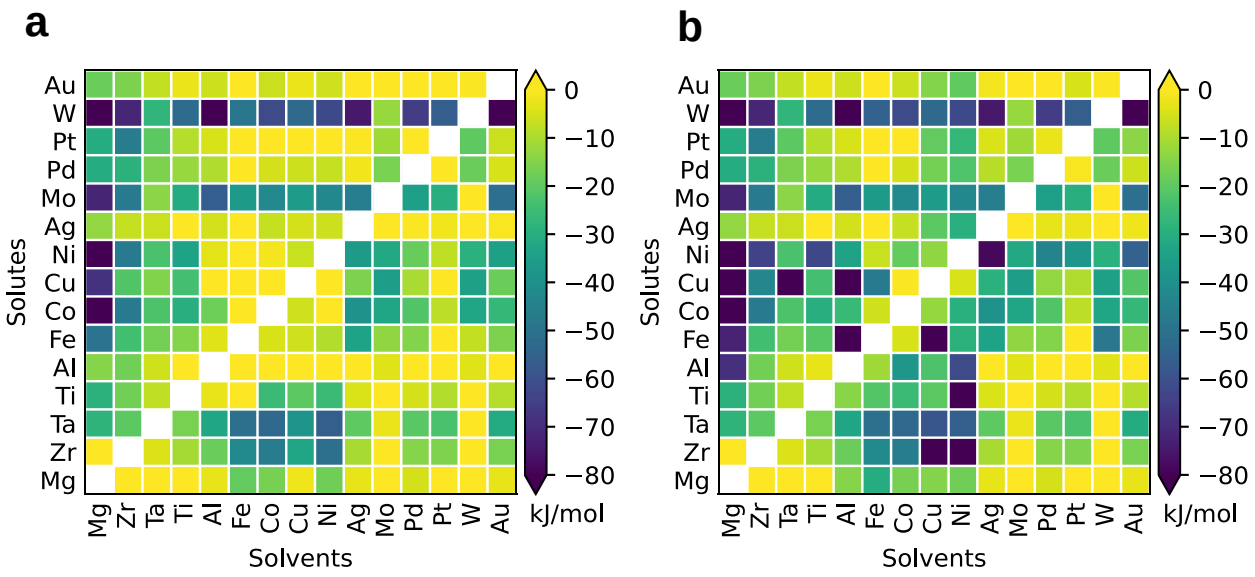

Supplementary Fig. 25: Predictions for the segregation tendency (25th percentile value) across the alloy space, with elements arranged by increasing Pauling electronegativity: Mg → Au; for alloys with multiple potentials, we report (a) the least segregating spectra and (b) the most segregating spectra.

A.3. Identifiers for Interatomic Potentials

Supplementary Table 1: References for interatomic potentials used to compute the GB segregation spectra in Supplementary Figs. 2-20. The identifier number is the superscript to the solute name in each figure.

Interatomic Potential Identifier #	Reference
1	[118]
2	[213]
3	[114]
4	[214]
5	[215]
6	[98]
7	[216]
8	[217]
9	[218]
10	[184]

11	[219]
12	[100]
13	[220]
14	[221]
15	[67]
16	[222]
17	[223]
18	[180]
19	[122]
20	[181]
21	[111]
22	[224]
23	[225]
24	[226]
25	[227]
26	[49]
27	[228]
28	[229]
29	[115]
30	[230]
31	[231]
32	[117]
33	[116]
34	[232]
35	[233]
36	[234]
37	[101]
38	[235]
39	[236]
40	[237]
41	[238]
42	[99]

43	[239]
44	[240]
45	[241]
46	[242]
47	[119]
48	[243]
49	[244]
50	[245]
51	[246]
52	[112]
53	[113]
54	[247]
55	[102]
56	[248]
57	[249]

Appendix B: Derivation of Nanocrystalline Enthalpic Stability Criteria

B.1. Enthalpies for different alloy states

A dilute A(B) metal alloy of size N atoms, and fixed number of solvent (N_A), and solute (N_B) atoms can exist in the following four different alloy states relevant to our analysis:

B.1.1. Phase-separated state

For a phase-separated state, the total energy is:

$$E_{tot}^{sep} = N_A E_A^{eq} + N_B E_B^{eq} \tag{58}$$

where:

E_A^{eq}, E_B^{eq} = the energy per atom for A, and B, respectively, in their pure crystalline equilibrium state (i.e. cohesive energy).

B.1.2. Solid solution

For a solid solution, the total energy is:

$$E_{tot}^{sln} = N_A E_A^{eq} + N_B E_B^{eq} + N \cdot \Delta E^{mix}(x) \tag{59}$$

where:

$\Delta E^{mix}(x)$ is the mixing energy at solute concentration $x = N_B/N$.

$\Delta E^{mix}(x)$ can be expressed in terms of the alloy solution energies [156] as:

$$\Delta E^{mix}(x) = \Delta E_{sol}^{A\ in\ B} \cdot x^2 \cdot (1-x) + \Delta E_{sol}^{B\ in\ A} \cdot x \cdot (1-x)^2 \tag{60}$$

where:

$\Delta E_{sol}^{B\ in\ A}$ = the energy of embedding one solute atom (B) in a large matrix of solvent (A) atoms, as defined by Eq. (12), Section 3 of the paper; similarly, $\Delta E_{sol}^{A\ in\ B}$ is a solute of (A) in a matrix of (B).

$\Delta E_{sol}^{B\ in\ A}$, and $\Delta E_{sol}^{A\ in\ B}$ are simply the derivatives of the mixing energy at the composition end-points, $x = 0$ and $x = 1$, respectively, i.e. $\Delta E_{sol}^{B\ in\ A} = [\partial \Delta E^{mix}/\partial x]_{x=0}$. And thus, at the dilute limit ($x \to 0$), we can approximate $\Delta E_{sol}^{B\ in\ A}$ [157]:

$$\Delta E_{sol}^{B\ in\ A} \approx \frac{1}{x} \cdot \Delta E^{mix}(x) = \frac{N}{N_B} \cdot \Delta E^{mix}(x) \tag{61}$$

Substituting in Eq. (59), and rearranging, we get the total energy for a solid solution in the dilute limit:

$$E_{tot}^{sln} \approx N_A E_A^{eq} + N_B \cdot \left(E_B^{eq} + \Delta E_{sol}^{B\ in\ A}\right) \tag{62}$$

B.1.3. Ordered compound

For a compound forming system, the total energy is defined by the tie-line between the pure solvent phase and the ordered compound:

$$E_{tot}^{ord} = N_A E_A^{eq} + N_B \cdot \left[E_B^{eq} + (1/x_s^c) \cdot \Delta E_{ord}^{form}\right] \tag{63}$$

where:

x_s^c = stoichiometry of the ordered compound.

ΔE_{ord}^{form}= formation energy of the ordered compound as defined by Eq. (13) Section 3 of the paper.

B.1.4. Nanocrystalline grain boundary solute-segregated state

For this state, we assume a spectrum of solute segregation energies at the grain boundary; solvent atoms N_A are divided between the crystal (intra-grain region) N_A^c and the grain boundary (GB) N_A^{GB}; all solute atoms are segregated at the GB $N_B^{GB} = N_B$; GB sites are filled by enthalpic preference of the segregation energy. The total energy of the nanocrystalline structure in the dilute limit is:

$$\begin{aligned} E_{tot}^{nc} &= N_A^c E_A^{eq} + N_A^{GB} \cdot \left(E_A^{eq} + k_\gamma \gamma\right) \\ &+ \sum_i N_i^{GB} X_{i,B}^{GB} \cdot \left(E_B^{eq} + \Delta E_{sol}^{B\ in\ A} + k_\gamma \gamma + \Delta E_i^{seg}\right) \end{aligned} \tag{64}$$

where:

$k_\gamma\gamma$ = the GB energy per atom; γ is the GB energy per area, and k_γ is a conversion factor incorporating GB thickness.

N_i^{GB} = the number of GB atoms of site-type (i).

$X_{i,B}^{GB}$= the fraction of site-type(i) occupied by solute atoms, B.

ΔE_i^{seg}= the segregation energy for GB site-type (i) as defined by Eq (1), Section 2.1 of the paper.

We stress that Eq. (64), similar to Eq. (62), is valid in the dilute limit; for non-dilute concentrations, Eq. (64) should be redefined to incorporate the concentration dependent $\Delta E^{mix}(x)$, instead of $\Delta E_{sol}^{B\ in\ A}$.

B.2. Spectral Enthalpic Stability Criteria for Nanocrystalline Alloys

B.2.1. Stability against solid solutions

We compare Eqs. (64) and (62) to define the condition for $E_{tot}^{nc} < E_{tot}^{sln}$:

$$\begin{aligned} N_A^c E_A^{eq} + N_A^{GB}\cdot\left(E_A^{eq} + k_\gamma\gamma\right) + \sum_i N_i^{GB} X_{i,B}^{GB}\cdot\left(E_B^{eq} + \Delta E_{sol}^{B\ in\ A} + k_\gamma\gamma + \Delta E_i^{seg}\right) \\ < N_A E_A^{eq} + N_B\cdot\left(E_B^{eq} + \Delta E_{sol}^{B\ in\ A}\right) \end{aligned} \tag{65}$$

As $N_A^c E_A^{eq} + N_A^{GB} E_A^{eq} = N_A E_A^{eq}$, and $\sum_i N_i^{GB} X_{i,B}^{GB}\cdot\left(E_B^{eq} + \Delta E^{B\ in\ A}\right) = N_B\cdot\left(E_B^{eq} + \Delta E^{B\ in\ A}\right)$, we cancel out these terms, and rearrange to get:

$$k_\gamma\gamma\cdot(N_A^{GB} + N_B^{GB}) + \sum_i N_i^{GB} X_{i,B}^{GB}\ \Delta E_i^{seg} < 0 \tag{66}$$

As $N_A^{GB} + N_B^{GB} = N_{tot}^{GB}$, and the fraction of site-type (i) is $F_i^{GB} = N_i^{GB} / N_{tot}^{GB}$, we divide Eq. (66) by N_{tot}^{GB} to get:

$$\sum_i F_i^{GB}\ X_{i,B}^{GB}\Delta E_i^{seg} < -k_\gamma\gamma \tag{67}$$

To minimize the LHS of Eq. (7), N_B^{GB} should be limited to filling favorable GB site-types $\left(\Delta E_i^{seg} \leq 0\right)$, which sets the condition for nanocrystalline enthalpic stability against solid solutions:

$$\sum_{\Delta E_i^{seg}=-\infty}^{0} F_i^{GB} \Delta E_i^{seg} < -k_\gamma \gamma \tag{68}$$

For a continuous distribution F_i^{GB}, Eq. (68) can be expressed as:

$$\int_{\Delta E_i^{seg}=-\infty}^{0} F_i^{GB} \Delta E_i^{seg} \, \mathrm{d}\left(\Delta E_i^{seg}\right) < -k_\gamma \gamma \tag{69}$$

B.2.2. Stability against phase separation

We compare Eqs. (64) and (62) to define the condition for $E_{tot}^{nc} < E_{tot}^{sep}$:

$$\begin{aligned} N_A^c E_A^{eq} + N_A^{GB} \cdot \left(E_A^{eq} + k_\gamma \gamma\right) + \sum_i N_i^{GB} X_{i,B}^{GB} \cdot \left(E_B^{eq} + \Delta E_{sol}^{B\ in\ A} + k_\gamma \gamma + \Delta E_i^{seg}\right) \\ < N_A E_A^{eq} + N_B E_B^{eq} \end{aligned} \tag{70}$$

We cancel out $N_A^c E_A^{eq} + N_A^{GB} E_A^{eq} = N_A E_A^{eq}$, and $\sum_i N_i^{GB} X_{i,B}^{GB} E_B^{eq} = N_B E_B^{eq}$, and rearrange to get:

$$\sum_i N_i^{GB} X_{i,B}^{GB} \cdot \left(\Delta E_{sol}^{B\ in\ A} + \Delta E_i^{seg}\right) < -k_\gamma \gamma \cdot \left(N_A^{GB} + N_B^{GB}\right) \tag{71}$$

Dividing by $N_{tot}^{GB} = N_A^{GB} + N_B^{GB}$:

$$\sum_i F_i^{GB} X_{i,B}^{GB} \cdot \left(\Delta E_i^{seg} + \Delta E_{sol}^{B\ in\ A}\right) < -k_\gamma \gamma \tag{72}$$

To minimize the LHS of Eq. (72), N_B^{GB} should be limited to filling all GB site-types with $\left(\Delta E_i^{seg} + \Delta E_{sol}^{B\ in\ A}\right) \leq 0$, or alternatively, $\Delta E_i^{seg} \leq -\Delta E_{sol}^{B\ in\ A}$, which sets the condition for nanocrystalline ground state stability against phase separation:

$$\sum_{\Delta E_i^{seg}=-\infty}^{-\Delta E_{sol}^{B\ in\ A}} F_i^{GB} \cdot \left(\Delta E_i^{seg} + \Delta E_{sol}^{B\ in\ A}\right) < -k_\gamma \gamma \tag{73}$$

For a continuous distribution F_i^{GB}, Eq. (73) can be expressed as:

$$\int_{\Delta E_i^{seg}=-\infty}^{-\Delta E_{sol}^{B\ in\ A}} F_i^{GB}\cdot\left(\Delta E_i^{seg}+\Delta E_{sol}^{B\ in\ A}\right)d\left(\Delta E_i^{seg}\right)<-k_\gamma\gamma \tag{74}$$

B.2.3. Stability against compound formation

We compare Eqs. (64) and (63) to define the condition for $E_{tot}^{nc}<E_{tot}^{ord}$:

$$\begin{aligned}N_A^c E_A^{eq}+N_A^{GB}\cdot\left(E_A^{eq}+k_\gamma\gamma\right)+\sum_i N_i^{GB}X_{i,B}^{GB}\cdot\left(E_B^{eq}+\Delta E_{sol}^{B\ in\ A}+k_\gamma\gamma+\Delta E_i^{seg}\right)\\ <N_A E_A^{eq}+N_B\cdot\left[E_B^{eq}+(1/x_s^c)\cdot\Delta E_{ord}^{form}\right]\end{aligned} \tag{75}$$

We cancel out $N_A^c E_A^{eq}+N_A^{GB}E_A^{eq}=N_A E_A^{eq}$, and $\sum_i N_i^{GB}X_{i,B}^{GB}E_B^{eq}=N_B E_B^{eq}$, and rearrange to get:

$$\begin{aligned}\sum_i N_i^{GB}X_{i,B}^{GB}\cdot\left(\Delta E_i^{seg}+\Delta E_{sol}^{B\ in\ A}\right)-N_B\cdot\left[(1/x_s^c)\cdot\Delta E_{ord}^{form}\right]\\ <-k_\gamma\gamma\cdot\left(N_A^{GB}+N_B^{GB}\right)\end{aligned} \tag{76}$$

As $\sum_i N_i^{GB}X_{i,B}^{GB}=N_B$, we can express $N_B\cdot\left[(1/x_s^c)\cdot\Delta E_{ord}^{form}\right]$=$\sum_i N_i^{GB}X_{i,B}^{GB}\cdot(1/x_s^c)\cdot\Delta E_{ord}^{form}$ to get:

$$\sum_i N_i^{GB}X_{i,B}^{GB}\cdot\left(\Delta E_i^{seg}+\Delta E_{sol}^{B\ in\ A}-(1/x_s^c)\cdot\Delta E_{ord}^{form}\right)<-k_\gamma\gamma\cdot\left(N_A^{GB}+N_B^{GB}\right) \tag{77}$$

Dividing by $N_{tot}^{GB}=N_A^{GB}+N_B^{GB}$:

$$\sum_i F_i^{GB}X_{i,B}^{GB}\cdot\left(\Delta E_i^{seg}+\Delta E_{sol}^{B\ in\ A}-(1/x_s^c)\cdot\Delta E_{ord}^{form}\right)<-k_\gamma\gamma \tag{78}$$

To minimize the LHS of Eq. (78), N_B^{GB} should be limited to filling all GB site-types with $\left(\Delta E_i^{seg}+\Delta E_{sol}^{B\ in\ A}-(1/x_s^c)\cdot\Delta E_{ord}^{form}\right)\leq 0$, or alternatively, $\Delta E_i^{seg}\leq(1/x_s^c)\cdot\Delta E_{ord}^{form}-\Delta E_{sol}^{B\ in\ A}$, which sets the condition for nanocrystalline ground state stability against compound formation:

$$\sum_{\Delta E_i^{seg}=-\infty}^{(1/x_s^c)\cdot\Delta E_{ord}^{form}-\Delta E_{sol}^{B\ in\ A}} F_i^{GB}\cdot\left(\Delta E_i^{seg}+\Delta E_{sol}^{B\ in\ A}-(1/x_s^c)\cdot\Delta E_{ord}^{form}\right)<-k_\gamma\gamma \tag{79}$$

For a continuous distribution F_i^{GB}, Eq. (79) can be expressed as:

$$\int_{\Delta E_i^{seg}=-\infty}^{(1/x_s^c)\cdot\Delta E_{ord}^{form}-\Delta E_{sol}^{B\ in\ A}} F_i^{GB}\cdot\left(\Delta E_i^{seg}+\Delta E_{sol}^{B\ in\ A}-(1/x_s^c)\cdot\Delta E_{ord}^{form}\right) < -k_\gamma\gamma \tag{80}$$

Finally, if we define $\Delta E_{ref=sln}^{solute}$ as:

$$\Delta E_{ref=sln}^{solute}=\frac{1}{x_s^c}\Delta E_{ord}^{form}-\Delta E_{sol}^{B\ in\ A} \tag{81}$$

with $\Delta E_{ord}^{form}=0$ for phase separating systems. Eqs. (74) and (80) that define the enthalpic stability criteria against phase separation, and compound formation, respectively, can be consolidated into one general equation that defines nanocrystalline stability against the alloy ground states (i.e. phases separated, or ordered compound):

$$\int_{\Delta E_i^{seg}=-\infty}^{\Delta E_{ref=sln}^{solute}} F_i^{GB}\cdot\left(\Delta E_i^{seg}-\Delta E_{ref=sln}^{solute}\right) < -k_\gamma\gamma \tag{82}$$

REFERENCES

[1] P. Lejček, S. Hofmann, Thermodynamics and structural aspects of grain boundary segregation, Crit. Rev. Solid State Mater. Sci. 20 (1995) 1–85. https://doi.org/10.1080/10408439508243544.

[2] M.P. Seah, Chemistry of solid–solid interfaces — A review of its characterization, theory, and relevance to materials science, J. Vac. Sci. Technol. 17 (1980) 16–24. https://doi.org/10.1116/1.570464.

[3] C.T. Liu, C.L. White, J.A. Horton, Effect of boron on grain-boundaries in Ni3Al†, Acta Metall. 33 (1985) 213–229. https://doi.org/10.1016/0001-6160(85)90139-7.

[4] R. Wu, A.J. Freeman, G.B. Olson, First principles determination of the effects of phosphorus and boron on iron grain boundary cohesion, Science (80-.). 265 (1994) 376–380. https://doi.org/10.1126/science.265.5170.376.

[5] T. Yang, Y.L. Zhao, W.P. Li, C.Y. Yu, J.H. Luan, D.Y. Lin, L. Fan, Z.B. Jiao, W.H. Liu, X.J. Liu, J.J. Kai, J.C. Huang, C.T. Liu, Ultrahigh-strength and ductile superlattice alloys with nanoscale disordered interfaces, Science. 369 (2020) 427–432. https://doi.org/10.1126/science.abb6830.

[6] H.C. Rogers, Hydrogen Embrittlement of Metals, Science (80-.). 159 (1968) 1057–1064. https://doi.org/10.1126/science.159.3819.1057.

[7] R. Schweinfest, A.T. Paxton, M.W. Finnis, Bismuth embrittlement of copper is an atomic size effect, Nature. 432 (2004) 1008–1011. https://doi.org/10.1038/nature03198.

[8] C.L. Briant, P.L. Andresen, Grain boundary segregation in austenitic stainless steels and its effect on intergranular corrosion and stress corrosion cracking, Metall. Trans. A. 19 (1988) 495–504. https://doi.org/10.1007/BF02649264.

[9] M.J. Duarte, J. Klemm, S.O. Klemm, K.J.J. Mayrhofer, M. Stratmann, S. Borodin, A.H. Romero, M. Madinehei, D. Crespo, J. Serrano, S.S.A. Gerstl, P.P. Choi, D. Raabe, F.U. Renner, Element-resolved corrosion analysis of stainless-type glass-forming steels, Science (80-.). 341 (2013) 372–376. https://doi.org/10.1126/science.1230081.

[10] M.P. Harmer, The phase behavior of interfaces, Science (80-.). 332 (2011) 182–183. https://doi.org/10.1126/science.1204204.

[11] T. Frolov, D.L. Olmsted, M. Asta, Y. Mishin, Structural phase transformations in metallic grain boundaries, Nat. Commun. 4 (2013) 1899. https://doi.org/10.1038/ncomms2919.

[12] D. Raabe, M. Herbig, S. Sandlöbes, Y. Li, D. Tytko, M. Kuzmina, D. Ponge, P.-P. Choi, Grain boundary segregation engineering in metallic alloys: A pathway to the design of interfaces, Curr. Opin. Solid State Mater. Sci. 18 (2014) 253–261. https://doi.org/10.1016/J.COSSMS.2014.06.002.

[13] K. Lücke, K. Detert, A quantitative theory of grain-boundary motion and recrystallization in metals in the presence of impurities, Acta Metall. 5 (1957) 628–637. https://doi.org/10.1016/0001-6160(57)90109-8.

[14] J.W. Cahn, The impurity-drag effect in grain boundary motion, Acta Metall. 10 (1962) 789–798. https://doi.org/10.1016/0001-6160(62)90092-5.

[15] A. Michels, C.E. Krill, H. Ehrhardt, R. Birringer, D.T. Wu, Modelling the influence of grain-size-dependent solute drag on the kinetics of grain growth in nanocrystalline materials, Acta Mater. 47 (1999) 2143–2152. https://doi.org/10.1016/S1359-6454(99)00079-8.

[16] M. Hillert, Inhibition of grain growth by second-phase particles, Acta Metall. 36 (1988) 3177–3181. https://doi.org/10.1016/0001-6160(88)90053-3.

[17] K. Boylan, D. Ostrander, U. Erb, G. Palumbo, K.T. Aust, An in-situ tem study of the thermal stability of nanocrystalline NiP, Scr. Metall. Mater. 25 (1991) 2711–2716. https://doi.org/10.1016/0956-716X(91)90144-P.

[18] J. Weissmüller, Alloy effects in nanostructures, Nanostructured Mater. 3 (1993) 261–272. https://doi.org/10.1016/0965-9773(93)90088-S.

[19] T. Chookajorn, H.A. Murdoch, C.A. Schuh, Design of stable nanocrystalline alloys., Science. 337 (2012) 951–4. https://doi.org/10.1126/science.1224737.

[20] C.E. Krill, H. Ehrhardt, R. Birringer, Thermodynamic stabilization of nanocrystallinity, Zeitschrift Fuer Met. Res. Adv. Tech. 96 (2005) 1134–1141.

https://doi.org/10.3139/146.101152.

[21] M.A. Tschopp, H.A. Murdoch, L.J. Kecskes, K.A. Darling, “Bulk” Nanocrystalline Metals: Review of the Current State of the Art and Future Opportunities for Copper and Copper Alloys, JOM. 66 (2014) 1000–1019. https://doi.org/10.1007/s11837-014-0978-z.

[22] K.A. Darling, B.K. VanLeeuwen, J.E. Semones, C.C. Koch, R.O. Scattergood, L.J. Kecskes, S.N. Mathaudhu, Stabilized nanocrystalline iron-based alloys: Guiding efforts in alloy selection, Mater. Sci. Eng. A. 528 (2011) 4365–4371. https://doi.org/10.1016/J.MSEA.2011.02.080.

[23] P. Choi, M. da Silva, U. Klement, T. Al-Kassab, R. Kirchheim, Thermal stability of electrodeposited nanocrystalline Co-1.1at.%P, Acta Mater. 53 (2005) 4473–4481. https://doi.org/10.1016/J.ACTAMAT.2005.06.006.

[24] A.J. Detor, C.A. Schuh, Microstructural evolution during the heat treatment of nanocrystalline alloys, J. Mater. Res. 22 (2007) 3233–3248. https://doi.org/10.1557/JMR.2007.0403.

[25] A.J. Detor, C.A. Schuh, Grain boundary segregation, chemical ordering and stability of nanocrystalline alloys: Atomistic computer simulations in the Ni-W system, Acta Mater. 55 (2007) 4221–4232. https://doi.org/10.1016/j.actamat.2007.03.024.

[26] A.R. Kalidindi, C.A. Schuh, Stability criteria for nanocrystalline alloys, Acta Mater. 132 (2017) 128–137. https://doi.org/10.1016/J.ACTAMAT.2017.03.029.

[27] C.C. Koch, R.O. Scattergood, K.A. Darling, J.E. Semones, Stabilization of nanocrystalline grain sizes by solute additions, J. Mater. Sci. 43 (2008) 7264–7272. https://doi.org/10.1007/s10853-008-2870-0.

[28] R. Kirchheim, Reducing grain boundary, dislocation line and vacancy formation energies by solute segregation. II. Experimental evidence and consequences, Acta Mater. 55 (2007) 5139–5148. https://doi.org/10.1016/j.actamat.2007.05.033.

[29] R. Kirchheim, Reducing grain boundary, dislocation line and vacancy formation energies by solute segregation. I. Theoretical background, Acta Mater. 55 (2007) 5129–5138. https://doi.org/10.1016/j.actamat.2007.05.047.

[30] D. McLean, Grain boundaries in metals., Clarendon Press, Oxford, 1957.

[31] R.H. Fowler, E.A. Guggenheim, Statistical thermodynamics : a version of statistical mechanics for students of physics and chemistry, Cambridge University Press, Cambridge, 1939.

[32] M. Guttmann, Equilibrium segregation in a ternary solution: A model for temper embrittlement, Surf. Sci. 53 (1975) 213–227. https://doi.org/10.1016/0039-6028(75)90125-9.

[33] P. Wynblatt, D. Chatain, Anisotropy of segregation at grain boundaries and surfaces, Metall. Mater. Trans. A. 37 (2006) 2595–2620. https://doi.org/10.1007/BF02586096.

[34] D.N. Seidman, Subnanoscale Studies of Segregation at Grain Boundaries: Simulations and Experiments, Annu. Rev. Mater. Res. 32 (2002) 235–269. https://doi.org/10.1146/annurev.matsci.32.011602.095455.

[35] C.L. Brunt, Sources of variability in grain boundary segregation, Acta Metall. 31 (1983) 257–266. https://doi.org/10.1016/0001-6160(83)90102-5.

[36] P. Lejcek, Grain Boundary Segregation in Metals, Springer Berlin Heidelberg, Berlin, Heidelberg, 2010. https://doi.org/10.1007/978-3-642-12505-8.

[37] C.L. White, D.F. Stein, Sulfur segregation to grain boundaries in Ni3Al and Ni3(AI,Ti) alloys, Metall. Trans. A. 9 (1978) 13–22. https://doi.org/10.1007/BF02647165.

[38] T. Mütschele, R. Kirchheim, Segregation and diffusion of hydrogen in grain boundaries of palladium, Scr. Metall. 21 (1987) 135–140. https://doi.org/10.1016/0036-9748(87)90423-6.

[39] R. Kirchheim, Hydrogen solubility and diffusivity in defective and amorphous metals, Prog. Mater. Sci. 32 (1988) 261–325. https://doi.org/10.1016/0079-6425(88)90010-2.

[40] S. Suzuki, Influence of a variety of grain boundary structures in grain boundary segregation, ISIJ Int. 30 (1990) 1000–1002. https://doi.org/10.2355/isijinternational.30.1000.

[41] M.F. Ashby, F. Spaepen, S. Williams, The structure of grain boundaries described as a packing of polyhedra, Acta Metall. 26 (1978) 1647–1663. https://doi.org/10.1016/0001-6160(78)90075-5.

[42] C.L. White, W.A. Coghlan, The spectrum of binding energies approach to grain boundary segregation, Metall. Trans. A. 8 (1977) 1403–1412. https://doi.org/10.1007/BF02642853.

[43] D. Udler, D.N. Seidman, Solute segregation at [001] tilt boundaries in dilute f.c.c. alloys, Acta Mater. 46 (1998) 1221–1233. https://doi.org/10.1016/S1359-6454(97)00297-8.

[44] P. Lejček, M. Šob, V. Paidar, Interfacial segregation and grain boundary embrittlement: An overview and critical assessment of experimental data and calculated results, Prog. Mater. Sci. 87 (2017) 83–139. https://doi.org/10.1016/J.PMATSCI.2016.11.001.

[45] P. Lu, F. Abdeljawad, M. Rodriguez, M. Chandross, D.P. Adams, B.L. Boyce, B.G. Clark, N. Argibay, On the thermal stability and grain boundary segregation in nanocrystalline PtAu alloys, Materialia. 6 (2019) 100298. https://doi.org/10.1016/j.mtla.2019.100298.

[46] D.A. Steigerwald, P. Wynblatt, Calculation of the anisotropy of equilibrium surface composition in metallic solid solutions using the embedded atom method, Surf. Sci. 193 (1988) 287–303. https://doi.org/10.1016/0039-6028(88)90337-8.

[47] L. Huber, R. Hadian, B. Grabowski, J. Neugebauer, A machine learning approach to model solute grain boundary segregation, Npj Comput. Mater. 4 (2018) 64. https://doi.org/10.1038/s41524-018-0122-7.

[48] G.S. Rohrer, The distribution of grain boundary planes in polycrystals, JOM. 59 (2007) 38–42. https://doi.org/10.1007/s11837-007-0114-4.

[49] C.J. O'Brien, C.M. Barr, P.M. Price, K. Hattar, S.M. Foiles, Grain boundary phase transformations in PtAu and relevance to thermal stabilization of bulk nanocrystalline metals, J. Mater. Sci. 53 (2018) 2911–2927. https://doi.org/10.1007/s10853-017-1706-1.

[50] N.M. Heckman, S.M. Foiles, C.J. O'Brien, M. Chandross, C.M. Barr, N. Argibay, K. Hattar, P. Lu, D.P. Adams, B.L. Boyce, New nanoscale toughening mechanisms mitigate embrittlement in binary nanocrystalline alloys, Nanoscale. 10 (2018) 21231–21243. https://doi.org/10.1039/C8NR06419A.

[51] P.C. Millett, R.P. Selvam, A. Saxena, Stabilizing nanocrystalline materials with dopants, Acta Mater. 55 (2007) 2329–2336. https://doi.org/10.1016/J.ACTAMAT.2006.11.028.

[52] P.C. Millett, R.P. Selvam, A. Saxena, Molecular dynamics simulations of grain size

stabilization in nanocrystalline materials by addition of dopants, Acta Mater. 54 (2006) 297–303. https://doi.org/10.1016/J.ACTAMAT.2005.07.024.

[53] B. Sadigh, P. Erhart, A. Stukowski, A. Caro, E. Martinez, L. Zepeda-Ruiz, Scalable parallel Monte Carlo algorithm for atomistic simulations of precipitation in alloys, Phys. Rev. B. 85 (2012) 184203. https://doi.org/10.1103/PhysRevB.85.184203.

[54] X. Zhou, X. Yu, T. Kaub, R.L. Martens, G.B. Thompson, Grain Boundary Specific Segregation in Nanocrystalline Fe(Cr), Sci. Rep. 6 (2016) 34642. https://doi.org/10.1038/srep34642.

[55] A.J. Detor, C.A. Schuh, Grain boundary segregation, chemical ordering and stability of nanocrystalline alloys: Atomistic computer simulations in the Ni–W system, Acta Mater. 55 (2007) 4221–4232. https://doi.org/10.1016/J.ACTAMAT.2007.03.024.

[56] S.J. Dillon, M. Tang, W.C. Carter, M.P. Harmer, Complexion: A new concept for kinetic engineering in materials science, Acta Mater. 55 (2007) 6208–6218. https://doi.org/10.1016/J.ACTAMAT.2007.07.029.

[57] M. Herbig, D. Raabe, Y.J. Li, P. Choi, S. Zaefferer, S. Goto, Atomic-scale quantification of grain boundary segregation in nanocrystalline material, Phys. Rev. Lett. 112 (2013) 126103. https://doi.org/10.1103/PhysRevLett.112.126103.

[58] D.. Beshers, On the distribution of impurity atoms in the stress field of a dislocation, Acta Metall. 6 (1958) 521–523. https://doi.org/10.1016/0001-6160(58)90166-4.

[59] N. Louat, The Effect of Temperature on Cottrell Atmospheres, Proc. Phys. Soc. Sect. B. 69 (1956) 459–467. https://doi.org/10.1088/0370-1301/69/4/305.

[60] R.A. Johnson, Use of Fermi-Dirac statistics for defects in solids, Phys. Rev. B. 24 (1981) 7383–7384. https://doi.org/10.1103/PhysRevB.24.7383.

[61] D. Gupta, Influence of solute Segregation on grain-boundary energy and self-diffusion, Metall. Trans. A. 8 (1977) 1431–1438. https://doi.org/10.1007/BF02642856.

[62] F. Liu, R. Kirchheim, Nano-scale grain growth inhibited by reducing grain boundary energy through solute segregation, J. Cryst. Growth. 264 (2004) 385–391. https://doi.org/10.1016/J.JCRYSGRO.2003.12.021.

[63] P.A. Dowben, A. Miller, Surface segregation phenomena, CRC Press, 1990.

[64] J.M. Blakely, Segregation to surfaces: Dilute alloys of the transition metals, Crit. Rev. Solid State Mater. Sci. 7 (1978) 333–355. https://doi.org/10.1080/10408437808243444.

[65] W. Xiao, C.S. Liu, Z.X. Tian, W.T. Geng, Effect of applied stress on vacancy segregation near the grain boundary in nickel, J. Appl. Phys. 104 (2008) 053519. https://doi.org/10.1063/1.2975939.

[66] S. Plimpton, Fast Parallel Algorithms for Short-Range Molecular Dynamics, J. Comput. Phys. 117 (1995) 1–19. https://doi.org/10.1006/JCPH.1995.1039.

[67] M.I. Mendelev, M. Asta, M.J. Rahman, J.J. Hoyt, Development of interatomic potentials appropriate for simulation of solid–liquid interface properties in Al–Mg alloys, Philos. Mag. 89 (2009) 3269–3285. https://doi.org/10.1080/14786430903260727.

[68] L. Huber, B. Grabowski, M. Militzer, J. Neugebauer, J. Rottler, Ab initio modelling of solute segregation energies to a general grain boundary, Acta Mater. 132 (2017) 138–148. https://doi.org/10.1016/J.ACTAMAT.2017.04.024.

[69] P. Hirel, Atomsk: A tool for manipulating and converting atomic data files, Comput. Phys. Commun. 197 (2015) 212–219. https://doi.org/10.1016/J.CPC.2015.07.012.

[70] P.W. Hoffrogge, L.A. Barrales-Mora, Grain-resolved kinetics and rotation during grain growth of nanocrystalline Aluminium by molecular dynamics, Comput. Mater. Sci. 128 (2017) 207–222. https://doi.org/10.1016/J.COMMATSCI.2016.11.027.

[71] J.F. Panzarino, T.J. Rupert, Tracking Microstructure of Crystalline Materials: A Post-Processing Algorithm for Atomistic Simulations, JOM. 66 (2014) 417–428. https://doi.org/10.1007/s11837-013-0831-9.

[72] P.M. Larsen, S. Schmidt, J. Schiøtz, Robust structural identification via polyhedral template matching, Model. Simul. Mater. Sci. Eng. 24 (2016) 055007. https://doi.org/10.1088/0965-0393/24/5/055007.

[73] A. Stukowski, Visualization and analysis of atomistic simulation data with OVITO–the Open Visualization Tool, Model. Simul. Mater. Sci. Eng. 18 (2010) 015012. https://doi.org/10.1088/0965-0393/18/1/015012.

[74] A. Stukowski, Structure identification methods for atomistic simulations of crystalline materials, Model. Simul. Mater. Sci. Eng. 20 (2012) 045021. https://doi.org/10.1088/0965-0393/20/4/045021.

[75] F. Bachmann, R. Hielscher, H. Schaeben, Texture Analysis with MTEX – Free and Open Source Software Toolbox, Solid State Phenom. 160 (2010) 63–68. https://doi.org/10.4028/www.scientific.net/SSP.160.63.

[76] S. Patala, J.K. Mason, C.A. Schuh, Improved representations of misorientation information for grain boundary science and engineering, Prog. Mater. Sci. 57 (2012) 1383–1425. https://doi.org/10.1016/J.PMATSCI.2012.04.002.

[77] P. Lejček, L. Zheng, S. Hofmann, M. Šob, P. Lejček, L. Zheng, S. Hofmann, M. Šob, Applied Thermodynamics: Grain Boundary Segregation, Entropy. 16 (2014) 1462–1483. https://doi.org/10.3390/e16031462.

[78] L. Huber, R. Hadian, B. Grabowski, J. Neugebauer, A machine learning approach to model solute grain boundary segregation, Npj Comput. Mater. 4 (2018) 64. https://doi.org/10.1038/s41524-018-0122-7.

[79] S.D. Landy, A.S. Szalay, Bias and variance of angular correlation functions, Astrophys. J. 412 (1993) 64. https://doi.org/10.1086/172900.

[80] T. Chookajorn, C.A. Schuh, Thermodynamics of stable nanocrystalline alloys: A Monte Carlo analysis, Phys. Rev. B. 89 (2014) 064102. https://doi.org/10.1103/PhysRevB.89.064102.

[81] A.J. Detor, M.K. Miller, C.A. Schuh, Solute distribution in nanocrystalline Ni–W alloys examined through atom probe tomography, Philos. Mag. 86 (2006) 4459–4475. https://doi.org/10.1080/14786430600726749.

[82] M. Wagih, C.A. Schuh, Spectrum of grain boundary segregation energies in a polycrystal, Acta Mater. 181 (2019) 228–237. https://doi.org/10.1016/J.ACTAMAT.2019.09.034.

[83] C.A. Becker, F. Tavazza, Z.T. Trautt, R.A. Buarque De Macedo, Considerations for choosing and using force fields and interatomic potentials in materials science and engineering, Curr. Opin. Solid State Mater. Sci. 17 (2013) 277–283. https://doi.org/10.1016/j.cossms.2013.10.001.

[84] L.M. Hale, Z.T. Trautt, C.A. Becker, Evaluating variability with atomistic simulations: the effect of potential and calculation methodology on the modeling of lattice and elastic constants, Model. Simul. Mater. Sci. Eng. 26 (2018) 055003. https://doi.org/10.1088/1361-651X/AABC05.

[85] L. Huber, B. Grabowski, M. Militzer, J. Neugebauer, J. Rottler, Ab initio modelling of solute segregation energies to a general grain boundary, Acta Mater. 132 (2017) 138–148. https://doi.org/10.1016/j.actamat.2017.04.024.

[86] T. Mueller, A. Hernandez, C. Wang, Machine learning for interatomic potential models, J. Chem. Phys. 152 (2020) 241722. https://doi.org/10.1063/1.5126336.

[87] J. Behler, Perspective: Machine learning potentials for atomistic simulations, J. Chem. Phys. 145 (2016) 170901. https://doi.org/10.1063/1.4966192.

[88] J. Behler, M. Parrinello, Generalized neural-network representation of high-dimensional potential-energy surfaces, Phys. Rev. Lett. 98 (2007) 146401. https://doi.org/10.1103/PhysRevLett.98.146401.

[89] A.P. Bartók, M.C. Payne, R. Kondor, G. Csányi, Gaussian Approximation Potentials: The Accuracy of Quantum Mechanics, without the Electrons, Phys. Rev. Lett. 104 (2010) 136403. https://doi.org/10.1103/PhysRevLett.104.136403.

[90] A.P. Thompson, L.P. Swiler, C.R. Trott, S.M. Foiles, G.J. Tucker, Spectral neighbor analysis method for automated generation of quantum-accurate interatomic potentials, J. Comput. Phys. 285 (2015) 316–330. https://doi.org/10.1016/J.JCP.2014.12.018.

[91] A.P. Bartók, R. Kondor, G. Csányi, On representing chemical environments, Phys. Rev. B. 87 (2013) 184115. https://doi.org/10.1103/PhysRevB.87.184115.

[92] C.L. Kelchner, S. Plimpton, Dislocation nucleation and defect structure during surface indentation, Phys. Rev. B - Condens. Matter Mater. Phys. 58 (1998) 11085–11088. https://doi.org/10.1103/PhysRevB.58.11085.

[93] C.W. Rosenbrock, E.R. Homer, G. Csányi, G.L.W. Hart, Discovering the building blocks of atomic systems using machine learning: application to grain boundaries, Npj Comput. Mater. 3 (2017) 29. https://doi.org/10.1038/s41524-017-0027-x.

[94] V.L. Deringer, M.A. Caro, G. Csányi, Machine Learning Interatomic Potentials as Emerging Tools for Materials Science, Adv. Mater. 31 (2019) 1902765. https://doi.org/10.1002/adma.201902765.

[95] F.E. Harrell Jr, Regression modeling strategies: with applications to linear models, logistic and ordinal regression, and survival analysis, Springer, 2015.

[96] W. Cochran, Sampling techniques, J. Wiley, New York, 2006.

[97] N.R. Rhodes, M.A. Tschopp, K.N. Solanki, Quantifying the energetics and length scales of carbon segregation to α -Fe symmetric tilt grain boundaries using atomistic simulations, Model. Simul. Mater. Sci. Eng. 21 (2013) 035009. https://doi.org/10.1088/0965-0393/21/3/035009.

[98] Z. Pan, V. Borovikov, M.I. Mendelev, F. Sansoz, Development of a semi-empirical potential for simulation of Ni solute segregation into grain boundaries in Ag, Model. Simul. Mater. Sci. Eng. 26 (2018) 075004. https://doi.org/10.1088/1361-651X/AADEA3.

[99] V. Borovikov, M.I. Mendelev, A.H. King, Effects of stable and unstable stacking fault energy on dislocation nucleation in nano-crystalline metals, Model. Simul. Mater. Sci. Eng. 24 (2016) 085017. https://doi.org/10.1088/0965-0393/24/8/085017.

[100] M.I. Mendelev, D.J. Srolovitz, G.J. Ackland, S. Han, Effect of Fe segregation on the migration of a non-symmetric $\sum 5$ tilt grain boundary in Al, J. Mater. Res. 20 (2005) 208–218. https://doi.org/10.1557/JMR.2005.0024.

[101] B. Onat, S. Durukanoğlu, An optimized interatomic potential for Cu-Ni alloys with the embedded-atom method, J. Phys. Condens. Matter. 26 (2014). https://doi.org/10.1088/0953-8984/26/3/035404.

[102] S.R. Wilson, M.I. Mendelev, Anisotropy of the solid-liquid interface properties of the Ni-Zr B33 phase from molecular dynamics simulation, Philos. Mag. 95 (2015) 224–241. https://doi.org/10.1080/14786435.2014.995742.

[103] J.D. Schuler, T.J. Rupert, Materials selection rules for amorphous complexion formation in binary metallic alloys, Acta Mater. 140 (2017) 196–205. https://doi.org/10.1016/j.actamat.2017.08.042.

[104] M.A. Gibson, C.A. Schuh, Segregation-induced changes in grain boundary cohesion and embrittlement in binary alloys, Acta Mater. 95 (2015) 145–155. https://doi.org/10.1016/j.actamat.2015.05.004.

[105] M.A. Gibson, C.A. Schuh, A compilation of ab-initio calculations of embrittling potencies in binary metallic alloys, Data Br. 6 (2016) 143–148. https://doi.org/10.1016/J.DIB.2015.11.024.

[106] M.E. Tipping ME, C.M. Bishop CMBishop, Probabilistic Principal Component Analysis, 1997. http://www.ncrg.aston.ac.uk/ (accessed August 5, 2020).

[107] I.T. Jolliffe, A Note on the Use of Principal Components in Regression, Appl. Stat. 31 (1982) 300. https://doi.org/10.2307/2348005.

[108] B.A. Helfrecht, R. Semino, G. Pireddu, S.M. Auerbach, M. Ceriotti, A new kind of atlas of zeolite building blocks, J. Chem. Phys. 151 (2019) 154112. https://doi.org/10.1063/1.5119751.

[109] S.P. Lloyd, Least Squares Quantization in PCM, 1982.

[110] C. Elkan, Using the Triangle Inequality to Accelerate-Means, n.d.

[111] G.P. Purja Pun, Y. Mishin, Development of an interatomic potential for the Ni-Al system, Philos. Mag. 89 (2009) 3245–3267. https://doi.org/10.1080/14786430903258184.

[112] G.D. Samolyuk, L.K. Béland, G.M. Stocks, R.E. Stoller, Electron-phonon coupling in Ni-based binary alloys with application to displacement cascade modeling, J. Phys. Condens. Matter. 28 (2016). https://doi.org/10.1088/0953-8984/28/17/175501.

[113] S.B. Maisel, W.S. Ko, J.L. Zhang, B. Grabowski, J. Neugebauer, Thermomechanical response of NiTi shape-memory nanoprecipitates in TiV alloys, Phys. Rev. Mater. 1 (2017) 33610. https://doi.org/10.1103/PhysRevMaterials.1.033610.

[114] J.B. Adams, S.M. Foiles, W.G. Wolfer, Self-diffusion and impurity diffusion of fcc metals using the five-frequency model and the Embedded Atom Method, J. Mater. Res. 4 (1989) 102–112. https://doi.org/10.1557/JMR.1989.0102.

[115] L.K. Béland, C. Lu, Y.N. Osetskiy, G.D. Samolyuk, A. Caro, L. Wang, R.E. Stoller, Features of primary damage by high energy displacement cascades in concentrated Ni-based

alloys, J. Appl. Phys. 119 (2016) 085901. https://doi.org/10.1063/1.4942533.

[116] C.A. Howells, Y. Mishin, Angular-dependent interatomic potential for the binary Ni–Cr system, Model. Simul. Mater. Sci. Eng. 26 (2018) 085008. https://doi.org/10.1088/1361-651X/AAE400.

[117] X.W. Zhou, M.E. Foster, R.B. Sills, An Fe-Ni-Cr embedded atom method potential for austenitic and ferritic systems, J. Comput. Chem. 39 (2018) 2420–2431. https://doi.org/10.1002/jcc.25573.

[118] X.W. Zhou, R.A. Johnson, H.N.G. Wadley, Misfit-energy-increasing dislocations in vapor-deposited CoFe/NiFe multilayers, Phys. Rev. B - Condens. Matter Mater. Phys. 69 (2004) 144113. https://doi.org/10.1103/PhysRevB.69.144113.

[119] Y. Zhang, R. Ashcraft, M.I. Mendelev, C.Z. Wang, K.F. Kelton, Experimental and molecular dynamics simulation study of structure of liquid and amorphous Ni62Nb38 alloy, J. Chem. Phys. 145 (2016) 204505. https://doi.org/10.1063/1.4968212.

[120] H.A. Murdoch, C.A. Schuh, Estimation of grain boundary segregation enthalpy and its role in stable nanocrystalline alloy design, J. Mater. Res. 28 (2013) 2154–2163. https://doi.org/10.1557/jmr.2013.211.

[121] T. Watanabe, S. Tsurekawa, Control of brittleness and development of desirable mechanical properties in polycrystalline systems by grain boundary engineering, Acta Mater. 47 (1999) 4171–4185. https://doi.org/10.1016/S1359-6454(99)00275-X.

[122] Y. Mishin, M.J. Mehl, D.A. Papaconstantopoulos, Embedded-atom potential for B2-NiAl, Phys. Rev. B - Condens. Matter Mater. Phys. 65 (2002) 1–14. https://doi.org/10.1103/PhysRevB.65.224114.

[123] Y. Hu, J.D. Schuler, T.J. Rupert, Identifying interatomic potentials for the accurate modeling of interfacial segregation and structural transitions, Comput. Mater. Sci. 148 (2018) 10–20. https://doi.org/10.1016/J.COMMATSCI.2018.02.020.

[124] D.G. Pettifor, The structures of binary compounds: I. phenomenological structure maps, J. Phys. C Solid State Phys. 19 (1986) 285–313. https://doi.org/10.1088/0022-3719/19/3/002.

[125] R.F. Zhang, X.F. Kong, H.T. Wang, S.H. Zhang, D. Legut, S.H. Sheng, S. Srinivasan, K.

Rajan, T.C. Germann, An informatics guided classification of miscible and immiscible binary alloy systems, Sci. Rep. 7 (2017) 1–12. https://doi.org/10.1038/s41598-017-09704-1.

[126] G.L.W. Hart, S. Curtarolo, T.B. Massalski, O. Levy, Comprehensive search for new phases and compounds in binary alloy systems based on platinum-group metals, using a computational first-principles approach, Phys. Rev. X. 3 (2014) 041035. https://doi.org/10.1103/PhysRevX.3.041035.

[127] S. Curtarolo, G.L.W. Hart, M.B. Nardelli, N. Mingo, S. Sanvito, O. Levy, The high-throughput highway to computational materials design, Nat. Mater. 12 (2013) 191–201. https://doi.org/10.1038/nmat3568.

[128] A.L. Allred, Electronegativity values from thermochemical data, J. Inorg. Nucl. Chem. 17 (1961) 215–221. https://doi.org/10.1016/0022-1902(61)80142-5.

[129] E.T. Teatum, K.A. Gschneidner Jr., J.T. Waber, Compilation of Calculated Data Useful in Predicting Metallurgical Behavior of the Elements in Binary Alloy Systems., (n.d.). https://doi.org/10.2172/4789465.

[130] A.R. Miedema, Simple model for alloys, Philips Tech. Rev. 33 (1973) 149–160.

[131] W.M. Brown, A. Kohlmeyer, S.J. Plimpton, A.N. Tharrington, Implementing molecular dynamics on hybrid high performance computers - Particle-particle particle-mesh, Comput. Phys. Commun. 183 (2012) 449–459. https://doi.org/10.1016/j.cpc.2011.10.012.

[132] F. Pedregosa, G. Varoquaux, A. Gramfort, V. Michel, B. Thirion, O. Grisel, M. Blondel, P. Prettenhofer, R. Weiss, V. Dubourg, J. Vanderplas, A. Passos, D. Cournapeau, M. Brucher, M. Perrot, É. Duchesnay, Scikit-learn: Machine Learning in Python, J. Mach. Learn. Res. 12 (2011) 2825–2830. http://jmlr.org/papers/v12/pedregosa11a.html (accessed August 5, 2020).

[133] H. Gleiter, Nanocrystalline materials, Prog. Mater. Sci. 33 (1989) 223–315. https://doi.org/10.1016/0079-6425(89)90001-7.

[134] K.. Kumar, H. Van Swygenhoven, S. Suresh, Mechanical behavior of nanocrystalline metals and alloys, Acta Mater. 51 (2003) 5743–5774. https://doi.org/10.1016/J.ACTAMAT.2003.08.032.

[135] L. Lu, Y. Shen, X. Chen, L. Qian, K. Lu, Ultrahigh Strength and High Electrical Conductivity in Copper, Science (80-.). 304 (2004) 422–426. https://doi.org/10.1126/science.1092905.

[136] J.S. Juan, M.L. Nó, C.A. Schuh, Nanoscale shape-memory alloys for ultrahigh mechanical damping, Nat. Nanotechnol. 4 (2009) 415–419. https://doi.org/10.1038/nnano.2009.142.

[137] K.A. Darling, M. Rajagopalan, M. Komarasamy, M.A. Bhatia, B.C. Hornbuckle, R.S. Mishra, K.N. Solanki, Extreme creep resistance in a microstructurally stable nanocrystalline alloy, Nature. 537 (2016) 378–381. https://doi.org/10.1038/nature19313.

[138] V.Y. Gertsman, R. Birringer, On the room-temperature grain growth in nanocrystalline copper, Scr. Metall. Mater. 30 (1994) 577–581. https://doi.org/10.1016/0956-716X(94)90432-4.

[139] M. Ames, J. Markmann, R. Karos, A. Michels, A. Tschöpe, R. Birringer, Unraveling the nature of room temperature grain growth in nanocrystalline materials, Acta Mater. 56 (2008) 4255–4266. https://doi.org/10.1016/J.ACTAMAT.2008.04.051.

[140] R. Kirchheim, Grain coarsening inhibited by solute segregation, Acta Mater. 50 (2002) 413–419. https://doi.org/10.1016/S1359-6454(01)00338-X.

[141] J.R. Trelewicz, C.A. Schuh, Grain boundary segregation and thermodynamically stable binary nanocrystalline alloys, Phys. Rev. B. 79 (2009) 094112. https://doi.org/10.1103/PhysRevB.79.094112.

[142] H.A. Murdoch, C.A. Schuh, Stability of binary nanocrystalline alloys against grain growth and phase separation, Acta Mater. 61 (2013) 2121–2132. https://doi.org/10.1016/J.ACTAMAT.2012.12.033.

[143] K.A. Darling, M.A. Tschopp, B.K. VanLeeuwen, M.A. Atwater, Z.K. Liu, Mitigating grain growth in binary nanocrystalline alloys through solute selection based on thermodynamic stability maps, Comput. Mater. Sci. 84 (2014) 255–266. https://doi.org/10.1016/J.COMMATSCI.2013.10.018.

[144] M. Saber, H. Kotan, C.C. Koch, R.O. Scattergood, Thermodynamic stabilization of nanocrystalline binary alloys, J. Appl. Phys. 113 (2013) 063515. https://doi.org/10.1063/1.4791704.

[145] G.S. Rohrer, Grain boundary energy anisotropy: a review, J. Mater. Sci. 46 (2011) 5881–5895. https://doi.org/10.1007/s10853-011-5677-3.

[146] M. Wagih, C.A. Schuh, Grain boundary segregation beyond the dilute limit: Separating the two contributions of site spectrality and solute interactions, Acta Mater. 199 (2020) 63–72. https://doi.org/10.1016/j.actamat.2020.08.022.

[147] M. Wagih, C.A. Schuh, Thermodynamics and design of nanocrystalline alloys using grain boundary segregation spectra, Acta Mater. 217 (2021) 117177. https://doi.org/10.1016/J.ACTAMAT.2021.117177.

[148] M. Wagih, P.M. Larsen, C.A. Schuh, Learning grain boundary segregation energy spectra in polycrystals, Nat. Commun. 11 (2020) 1–9. https://doi.org/10.1038/s41467-020-20083-6.

[149] J.E. Saal, S. Kirklin, M. Aykol, B. Meredig, C. Wolverton, Materials design and discovery with high-throughput density functional theory: The open quantum materials database (OQMD), JOM. 65 (2013) 1501–1509. https://doi.org/10.1007/s11837-013-0755-4.

[150] S. Kirklin, J.E. Saal, B. Meredig, A. Thompson, J.W. Doak, M. Aykol, S. Rühl, C. Wolverton, The Open Quantum Materials Database (OQMD): assessing the accuracy of DFT formation energies, Npj Comput. Mater. 1 (2015) 15010. https://doi.org/10.1038/npjcompumats.2015.10.

[151] A. Jain, G. Hautier, C.J. Moore, S. Ping Ong, C.C. Fischer, T. Mueller, K.A. Persson, G. Ceder, A high-throughput infrastructure for density functional theory calculations, Comput. Mater. Sci. 50 (2011) 2295–2310. https://doi.org/10.1016/j.commatsci.2011.02.023.

[152] S. Curtarolo, W. Setyawan, S. Wang, J. Xue, K. Yang, R.H. Taylor, L.J. Nelson, G.L.W. Hart, S. Sanvito, M. Buongiorno-Nardelli, N. Mingo, O. Levy, AFLOWLIB.ORG: A distributed materials properties repository from high-throughput ab initio calculations, Comput. Mater. Sci. 58 (2012) 227–235. https://doi.org/10.1016/j.commatsci.2012.02.002.

[153] P. Lejček, S. Hofmann, M. Všianská, M. Šob, Entropy matters in grain boundary segregation, Acta Mater. 206 (2021) 116597. https://doi.org/10.1016/j.actamat.2020.116597.

[154] M.S. Daw, M.I. Baskes, Embedded-atom method: Derivation and application to impurities,

surfaces, and other defects in metals, Phys. Rev. B. 29 (1984) 6443–6453. https://doi.org/10.1103/PhysRevB.29.6443.

[155] A. Hjorth Larsen, J. JØrgen Mortensen, J. Blomqvist, I.E. Castelli, R. Christensen, M. Dułak, J. Friis, M.N. Groves, B. Hammer, C. Hargus, E.D. Hermes, P.C. Jennings, P. Bjerre Jensen, J. Kermode, J.R. Kitchin, E. Leonhard Kolsbjerg, J. Kubal, K. Kaasbjerg, S. Lysgaard, J. Bergmann Maronsson, T. Maxson, T. Olsen, L. Pastewka, A. Peterson, C. Rostgaard, J. SchiØtz, O. Schütt, M. Strange, K.S. Thygesen, T. Vegge, L. Vilhelmsen, M. Walter, Z. Zeng, K.W. Jacobsen, The atomic simulation environment - A Python library for working with atoms, J. Phys. Condens. Matter. 29 (2017) 273002. https://doi.org/10.1088/1361-648X/aa680e.

[156] M.H.F. Sluiter, Y. Kawazoe, Prediction of the mixing enthalpy of alloys, Europhys. Lett. 57 (2002) 526–532. https://doi.org/10.1209/epl/i2002-00493-3.

[157] C. Wolverton, V. Ozoliņš, First-principles aluminum database: Energetics of binary Al alloys and compounds, Phys. Rev. B - Condens. Matter Mater. Phys. 73 (2006) 144104. https://doi.org/10.1103/PhysRevB.73.144104.

[158] D.E. Laughlin, W.A. Soffa, The Third Law of Thermodynamics: Phase equilibria and phase diagrams at low temperatures, Acta Mater. 145 (2018) 49–61. https://doi.org/10.1016/j.actamat.2017.11.037.

[159] P.P. Fedorov, Third law of thermodynamics as applied to phase diagrams, Russ. J. Inorg. Chem. 55 (2010) 1722–1739. https://doi.org/10.1134/S0036023610110100.

[160] T. Chookajorn, M. Park, C.A. Schuh, Duplex nanocrystalline alloys: Entropic nanostructure stabilization and a case study on W–Cr, J. Mater. Res. 30 (2015) 151–163. https://doi.org/10.1557/jmr.2014.385.

[161] A.R. Kalidindi, C.A. Schuh, Phase transitions in stable nanocrystalline alloys, J. Mater. Res. 32 (2017) 1993–2002. https://doi.org/10.1557/jmr.2017.188.

[162] M. Tang, W.C. Carter, R.M. Cannon, Diffuse interface model for structural transitions of grain boundaries, Phys. Rev. B - Condens. Matter Mater. Phys. 73 (2006) 024102. https://doi.org/10.1103/PhysRevB.73.024102.

[163] P.R. Cantwell, M. Tang, S.J. Dillon, J. Luo, G.S. Rohrer, M.P. Harmer, Grain boundary

complexions, Acta Mater. 62 (2014) 1–48. https://doi.org/10.1016/J.ACTAMAT.2013.07.037.

[164] T. Frolov, S. V. Divinski, M. Asta, Y. Mishin, Effect of Interface Phase Transformations on Diffusion and Segregation in High-Angle Grain Boundaries, Phys. Rev. Lett. 110 (2013) 255502. https://doi.org/10.1103/PhysRevLett.110.255502.

[165] T. Frolov, M. Asta, Y. Mishin, Segregation-induced phase transformations in grain boundaries, Phys. Rev. B. 92 (2015) 020103. https://doi.org/10.1103/PhysRevB.92.020103.

[166] K. Santhi, E. Thirumal, S.N. Karthick, H.J. Kim, M. Nidhin, V. Narayanan, A. Stephen, Synthesis, structure stability and magnetic properties of nanocrystalline Ag-Ni alloy, J. Nanoparticle Res. 14 (2012) 1–12. https://doi.org/10.1007/s11051-012-0868-7.

[167] Z.B. Jiao, C.A. Schuh, Nanocrystalline Ag-W alloys lose stability upon solute desegregation from grain boundaries, Acta Mater. 161 (2018) 194–206. https://doi.org/10.1016/J.ACTAMAT.2018.09.014.

[168] D.P. Weston, S.P.A. Gill, M. Fay, S.J. Harris, G.N. Yap, D. Zhang, K. Dinsdale, Nano-structure of Co-W alloy electrodeposited from gluconate bath, Surf. Coatings Technol. 236 (2013) 75–83. https://doi.org/10.1016/j.surfcoat.2013.09.031.

[169] T. Spassov, L. Lyubenova, Y. Liu, S. Bliznakov, M. Spassova, N. Dimitrov, Mechanochemical synthesis, thermal stability and selective electrochemical dissolution of Cu-Ag solid solutions, J. Alloys Compd. 478 (2009) 232–236. https://doi.org/10.1016/j.jallcom.2008.12.005.

[170] T. Frolov, K.A. Darling, L.J. Kecskes, Y. Mishin, Stabilization and strengthening of nanocrystalline copper by alloying with tantalum, Acta Mater. 60 (2012) 2158–2168. https://doi.org/10.1016/J.ACTAMAT.2012.01.011.

[171] G. Csiszár, S.J.B. Kurz, E.J. Mittemeijer, Stability of nanosized alloy thin films: Faulting and phase separation in metastable Ni/Cu/Ag-W films, Acta Mater. 110 (2016) 324–340. https://doi.org/10.1016/j.actamat.2016.02.068.

[172] A. Khalajhedayati, T.J. Rupert, High-Temperature Stability and Grain Boundary Complexion Formation in a Nanocrystalline Cu-Zr Alloy, JOM. 67 (2015) 2788–2801. https://doi.org/10.1007/s11837-015-1644-9.

[173] F. Liu, Grain growth in nanocrystalline Fe-Ag thin film, Mater. Lett. 59 (2005) 1458–1462. https://doi.org/10.1016/j.matlet.2005.01.003.

[174] J. Eckert, J.C. Holzer, W.L. Johnson, Thermal stability and grain growth behavior of mechanically alloyed nanocrystalline Fe-Cu alloys, J. Appl. Phys. 73 (1993) 131–141. https://doi.org/10.1063/1.353890.

[175] B.G. Clark, K. Hattar, M.T. Marshall, T. Chookajorn, B.L. Boyce, C.A. Schuh, Thermal Stability Comparison of Nanocrystalline Fe-Based Binary Alloy Pairs, JOM. 68 (2016) 1625–1633. https://doi.org/10.1007/s11837-016-1868-3.

[176] K.A. Darling, B.K. VanLeeuwen, C.C. Koch, R.O. Scattergood, Thermal stability of nanocrystalline Fe–Zr alloys, Mater. Sci. Eng. A. 527 (2010) 3572–3580. https://doi.org/10.1016/J.MSEA.2010.02.043.

[177] E. Pellicer, A. Varea, K.M. Sivaraman, S. Pané, S. Surinach, M.D. Baró, J. Nogués, B.J. Nelson, J. Sort, Grain boundary segregation and interdiffusion effects in nickel-copper alloys: An effective means to improve the thermal stability of nanocrystalline nickel, ACS Appl. Mater. Interfaces. 3 (2011) 2265–2274. https://doi.org/10.1021/am2004587.

[178] B.K. VanLeeuwen, K.A. Darling, C.C. Koch, R.O. Scattergood, B.G. Butler, Thermal stability of nanocrystalline Pd81Zr19, Acta Mater. 58 (2010) 4292–4297. https://doi.org/10.1016/j.actamat.2010.04.023.

[179] Y.R. Abe, W.L. Johnson, Stability of Nanocrystalline Structures in the Ti-Cu System, Mater. Sci. Forum. 88–90 (1992) 513–520. https://doi.org/10.4028/www.scientific.net/msf.88-90.513.

[180] J.E. Angelo, N.R. Moody, M.I. Baskes, Trapping of hydrogen to lattice defects in nickel, Model. Simul. Mater. Sci. Eng. 3 (1995) 289–307. https://doi.org/10.1088/0965-0393/3/3/001.

[181] Y. Mishin, Atomistic modeling of the γ and γ′-phases of the Ni-Al system, Acta Mater. 52 (2004) 1451–1467. https://doi.org/10.1016/j.actamat.2003.11.026.

[182] F.R. Boer, R. Boom, W.C.M. Mattens, A.R. Miedema, A.K. Niessen, Cohesion in metals : transition metal alloys, North-Holland, Amsterdam, 1988.

[183] D. Amram, C.A. Schuh, Interplay between thermodynamic and kinetic stabilization mechanisms in nanocrystalline Fe-Mg alloys, Acta Mater. 144 (2018) 447–458. https://doi.org/10.1016/j.actamat.2017.11.014.

[184] B. Jelinek, S. Groh, M.F. Horstemeyer, J. Houze, S.G. Kim, G.J. Wagner, A. Moitra, M.I. Baskes, Modified embedded atom method potential for Al, Si, Mg, Cu, and Fe alloys, Phys. Rev. B - Condens. Matter Mater. Phys. 85 (2012) 245102. https://doi.org/10.1103/PhysRevB.85.245102.

[185] M.P. Seah, Grain boundary segregation, J. Phys. F Met. Phys. 10 (1980) 1043–1064. https://doi.org/10.1088/0305-4608/10/6/006.

[186] P. Lejček, Effect of solute interaction on interfacial segregation and grain boundary embrittlement in binary alloys, J. Mater. Sci. 48 (2013) 2574–2580. https://doi.org/10.1007/s10853-012-7048-0.

[187] D. Udler, D.N. Seidman, Monte carlo simulation of the concentration dependence of segregation at vicinal grain boundaries, Interface Sci. 6 (1998) 259–265. https://doi.org/10.1023/A:1008697503079.

[188] D. Scheiber, L. Romaner, R. Pippan, P. Puschnig, Impact of solute-solute interactions on grain boundary segregation and cohesion in molybdenum, Phys. Rev. Mater. 2 (2018) 093609. https://doi.org/10.1103/PhysRevMaterials.2.093609.

[189] T. Krauß, S.M. Eich, Development of a segregation model beyond McLean based on atomistic simulations, Acta Mater. 187 (2020) 73–83. https://doi.org/10.1016/j.actamat.2020.01.031.

[190] J.D. Rittner, D.N. Seidman, Solute-atom segregation to 〈110〉 symmetric tilt grain boundaries, Acta Mater. 45 (1997) 3191–3202. https://doi.org/10.1016/S1359-6454(97)00002-5.

[191] D. Udler, D.N. Seidman, Solute segregation at [001] tilt boundaries in dilute f.c.c. alloys, Acta Mater. 46 (1998) 1221–1233. https://doi.org/10.1016/S1359-6454(97)00297-8.

[192] L. Huber, J. Rottler, M. Militzer, Atomistic simulations of the interaction of alloying elements with grain boundaries in Mg, Acta Mater. 80 (2014) 194–204.

https://doi.org/10.1016/j.actamat.2014.07.047.

[193] M. Rajagopalan, M.A. Tschopp, K.N. Solanki, Grain Boundary Segregation of Interstitial and Substitutional Impurity Atoms in Alpha-Iron, JOM. 66 (2014) 129–138. https://doi.org/10.1007/s11837-013-0807-9.

[194] A. Gupta, X. Zhou, G.B. Thompson, G.J. Tucker, Role of grain boundary character and its evolution on interfacial solute segregation behavior in nanocrystalline Ni-P, Acta Mater. 190 (2020) 113–123. https://doi.org/10.1016/j.actamat.2020.03.012.

[195] A.P. Sutton, V. Vitek, An atomistic study of tilt grain boundaries with substitutional impurities, Acta Metall. 30 (1982) 2011–2033. https://doi.org/10.1016/0001-6160(82)90105-5.

[196] V. Vitek, Gui Jin Wang, Segregation and grain boundary structure, Surf. Sci. 144 (1984) 110–123. https://doi.org/10.1016/0039-6028(84)90710-6.

[197] H.Y. Wang, R. Najafabadi, D.J. Srolovitz, R. Lesar, Interfacial segregation in Ag-Au, Au-Pd, and Cu-Ni alloys: I. (100) surfaces, Interface Sci. 1 (1993) 7–30. https://doi.org/10.1007/BF00203263.

[198] H.Y. Wang, R. Najafabadi, D.J. Srolovitz, R. Lesar, Interfacial segregation in Ag-Au, Au-Pd, and Cu-Ni alloys: II. [001]?5 twist grain boundaries, Interface Sci. 1 (1993) 31–47. https://doi.org/10.1007/BF00203264.

[199] K. Ishida, Effect of grain size on grain boundary segregation, J. Alloys Compd. 235 (1996) 244–249. https://doi.org/10.1016/0925-8388(95)02094-2.

[200] J. Creuze, F. Berthier, R. Tétot, B. Legrand, Intergranular segregation and ordering effect: A mixed Monte Carlo mean-field approach, Phys. Rev. B - Condens. Matter Mater. Phys. 62 (2000) 2813–2824. https://doi.org/10.1103/PhysRevB.62.2813.

[201] B. Sadigh, P. Erhart, A. Stukowski, A. Caro, E. Martinez, L. Zepeda-Ruiz, Scalable parallel Monte Carlo algorithm for atomistic simulations of precipitation in alloys, Phys. Rev. B. 85 (2012) 184203. https://doi.org/10.1103/PhysRevB.85.184203.

[202] P. Lejček, S. Hofmann, Segregation enthalpies of phosphorus, carbon and silicon at {013} and {012} symmetrical tilt grain boundaries in an Fe-3.5 at.% Si alloy, Acta Metall. Mater.

39 (1991) 2469–2476. https://doi.org/10.1016/0956-7151(91)90026-W.

[203] N. Metropolis, A.W. Rosenbluth, M.N. Rosenbluth, A.H. Teller, E. Teller, Equation of state calculations by fast computing machines, J. Chem. Phys. 21 (1953) 1087–1092. https://doi.org/10.1063/1.1699114.

[204] A. Seki, D.N. Seidman, Y. Oh, S.M. Foiles, Monte Carlo simulations of segregation at [001] twist boundaries in a Pt(Au) alloy-I. Results, Acta Metall. Mater. 39 (1991) 3167–3177. https://doi.org/10.1016/0956-7151(91)90051-2.

[205] A. Seki, D.N. Seidman, Y. Oh, S.M. Foiles, Monte Carlo simulations of segregation at [001] twist boundaries in a Pt(Au) alloy-II. Discussion, Acta Metall. Mater. 39 (1991) 3179–3185. https://doi.org/10.1016/0956-7151(91)90052-3.

[206] M. Menyhard, M. Yan, V. Vitek, Atomistic vs phenomenological approaches to grain boundary segregation: Computer modeling of Cu□Ag alloys, Acta Metall. Mater. 42 (1994) 2783–2796. https://doi.org/10.1016/0956-7151(94)90219-4.

[207] S.M. Foiles, Calculation of grain-boundary segregation in Ni-Cu alloys, Phys. Rev. B. 40 (1989) 11502–11506. https://doi.org/10.1103/PhysRevB.40.11502.

[208] X.-Y. Liu, J.B. Adams, Grain-boundary segregation in Al–10%Mg alloys at hot working temperatures, Acta Mater. 46 (1998) 3467–3476. https://doi.org/10.1016/S1359-6454(98)00038-X.

[209] M. Menyhard, B. Blum, C.J. McMahon, Grain boundary segregation and transformations in Bi-doped polycrystalline copper, Acta Metall. 37 (1989) 549–557. https://doi.org/10.1016/0001-6160(89)90238-1.

[210] U. Alber, H. Müllejans, M. Rühle, Bismuth segregation at copper grain boundaries, Acta Mater. 47 (1999) 4047–4060. https://doi.org/10.1016/S1359-6454(99)00265-7.

[211] L.S. Chang, E. Rabkin, B. Straumal, P. Lejček, S. Hofmann, W. Gust, Temperature dependence of the grain boundary segregation of Bi in Cu polycrystals, Scr. Mater. 37 (1997) 729–735. https://doi.org/10.1016/S1359-6462(97)00171-1.

[212] A. Fraczkiewicz, A.S. Gay, M. Biscondi, On the boron effect in FeAl (B2) intermetallic alloys, Mater. Sci. Eng. A. 258 (1998) 108–114. https://doi.org/10.1016/s0921-

5093(98)00923-x.

[213] S.M. Foiles, M.I. Baskes, M.S. Daw, Embedded-atom-method functions for the fcc metals Cu, Ag, Au, Ni, Pd, Pt, and their alloys, Phys. Rev. B. 33 (1986) 7983–7991. https://doi.org/10.1103/PhysRevB.33.7983.

[214] P.L. Williams, Y. Mishin, J.C. Hamilton, An embedded-atom potential for the Cu-Ag system, Model. Simul. Mater. Sci. Eng. 14 (2006) 817–833. https://doi.org/10.1088/0965-0393/14/5/002.

[215] H.H. Wu, D.R. Trinkle, Cu/Ag EAM potential optimized for heteroepitaxial diffusion from ab initio data, Comput. Mater. Sci. 47 (2009) 577–583. https://doi.org/10.1016/j.commatsci.2009.09.026.

[216] G.P. Purja Pun, V. Yamakov, Y. Mishin, Interatomic potential for the ternary Ni-Al-Co system and application to atomistic modeling of the B2-L10 martensitic transformation, Model. Simul. Mater. Sci. Eng. 23 (2015) 065006. https://doi.org/10.1088/0965-0393/23/6/065006.

[217] X.Y. Liu, C.L. Liu, L.J. Borucki, New investigation of copper's role in enhancing Al-Cu interconnect electromigration resistance from an atomistic view, Acta Mater. 47 (1999) 3227–3231. https://doi.org/10.1016/S1359-6454(99)00186-X.

[218] F. Apostol, Y. Mishin, Interatomic potential for the Al-Cu system, Phys. Rev. B - Condens. Matter Mater. Phys. 83 (2011) 054116. https://doi.org/10.1103/PhysRevB.83.054116.

[219] X.W. Zhou, D.K. Ward, M.E. Foster, An analytical bond-order potential for the aluminum copper binary system, J. Alloys Compd. 680 (2016) 752–767. https://doi.org/10.1016/j.jallcom.2016.04.055.

[220] X.Y. Liu, P.P. Ohotnicky, J.B. Adams, C. Lane Rohrer, R.W. Hyland, Anisotropic surface segregation in Al-Mg alloys, Surf. Sci. 373 (1997) 357–370. https://doi.org/10.1016/S0039-6028(96)01154-5.

[221] X.Y. Liu, J.B. Adams, Grain-boundary segregation in Al-10%Mg alloys at hot working temperatures, Acta Mater. 46 (1998) 3467–3476. https://doi.org/10.1016/S1359-6454(98)00038-X.

[222] D.E. Dickel, M.I. Baskes, I. Aslam, C.D. Barrett, New interatomic potential for Mg-Al-Zn alloys with specific application to dilute Mg-based alloys, Model. Simul. Mater. Sci. Eng. 26 (2018) 045010. https://doi.org/10.1088/1361-651X/aabaad.

[223] D. Farkas, C. Jones, Interatomic potentials for ternary Nb-Ti-Al alloys, Model. Simul. Mater. Sci. Eng. 4 (1996) 23–32. https://doi.org/10.1088/0965-0393/4/1/004.

[224] A. Kumar, A. Chernatynskiy, T. Liang, K. Choudhary, M.J. Noordhoek, Y.T. Cheng, S.R. Phillpot, S.B. Sinnott, Charge optimized many-body (COMB) potential for dynamical simulation of Ni-Al phases, J. Phys. Condens. Matter. 27 (2015) 336302. https://doi.org/10.1088/0953-8984/27/33/336302.

[225] A. Landa, P. Wynblatt, D.J. Siegel, J.B. Adams, O.N. Mryasov, X.Y. Liu, Development of glue-type potentials for the Al-Pb system: phase diagram calculation, Acta Mater. 48 (2000) 1753–1761. https://doi.org/10.1016/S1359-6454(00)00002-1.

[226] M.I. Mendelev, F. Zhang, Z. Ye, Y. Sun, M.C. Nguyen, S.R. Wilson, C.Z. Wang, K.M. Ho, Development of interatomic potentials appropriate for simulation of devitrification of Al90Sm10 alloy, Model. Simul. Mater. Sci. Eng. 23 (2015) 045013. https://doi.org/10.1088/0965-0393/23/4/045013.

[227] R.R. Zope, Y. Mishin, Interatomic potentials for atomistic simulations of the Ti-Al system, Phys. Rev. B - Condens. Matter Mater. Phys. 68 (2003) 024102. https://doi.org/10.1103/PhysRevB.68.024102.

[228] S. V. Starikov, N.Y. Lopanitsyna, D.E. Smirnova, S. V. Makarov, Atomistic simulation of Si-Au melt crystallization with novel interatomic potential, Comput. Mater. Sci. 142 (2018) 303–311. https://doi.org/10.1016/j.commatsci.2017.09.054.

[229] D. Farkas, A. Caro, Model interatomic potentials and lattice strain in a high-entropy alloy, J. Mater. Res. 33 (2018) 3218–3225. https://doi.org/10.1557/jmr.2018.245.

[230] A. Stukowski, B. Sadigh, P. Erhart, A. Caro, Efficient implementation of the concentration-dependent embedded atom method for molecular-dynamics and Monte-Carlo simulations, Model. Simul. Mater. Sci. Eng. 17 (2009) 075005. https://doi.org/10.1088/0965-0393/17/7/075005.

[231] G. Bonny, R.C. Pasianot, D. Terentyev, L. Malerba, Iron chromium potential to model high-

chromium ferritic alloys, Philos. Mag. 91 (2011) 1724–1746. https://doi.org/10.1080/14786435.2010.545780.

[232] G. Bonny, N. Castin, J. Bullens, A. Bakaev, T.C.P. Klaver, D. Terentyev, On the mobility of vacancy clusters in reduced activation steels: An atomistic study in the Fe-Cr-W model alloy, J. Phys. Condens. Matter. 25 (2013) 315401. https://doi.org/10.1088/0953-8984/25/31/315401.

[233] G. Bonny, R.C. Pasianot, N. Castin, L. Malerba, Ternary Fe-Cu-Ni many-body potential to model reactor pressure vessel steels: First validation by simulated thermal annealing, Philos. Mag. 89 (2009) 3531–3546. https://doi.org/10.1080/14786430903299824.

[234] S.M. Foiles, Calculation of the surface segregation of Ni-Cu alloys with the use of the embedded-atom method, Phys. Rev. B. 32 (1985) 7685–7693. https://doi.org/10.1103/PhysRevB.32.7685.

[235] J.J. Hoyt, J.W. Garvin, E.B. Webb, M. Asta, An embedded atom method interatomic potential for the Cu-Pb system, Model. Simul. Mater. Sci. Eng. 11 (2003) 287–299. https://doi.org/10.1088/0965-0393/11/3/302.

[236] G.P. Purja Pun, K.A. Darling, L.J. Kecskes, Y. Mishin, Angular-dependent interatomic potential for the Cu-Ta system and its application to structural stability of nano-crystalline alloys, Acta Mater. 100 (2015) 377–391. https://doi.org/10.1016/j.actamat.2015.08.052.

[237] M.I. Mendelev, D.J. Sordelet, M.J. Kramer, Using atomistic computer simulations to analyze x-ray diffraction data from metallic glasses, J. Appl. Phys. 102 (2007) 043501. https://doi.org/10.1063/1.2769157.

[238] M.I. Mendelev, M.J. Kramer, R.T. Ott, D.J. Sordelet, D. Yagodin, P. Popel, Development of suitable interatomic potentials for simulation of liquid and amorphous Cu-Zr alloys, Philos. Mag. 89 (2009) 967–987. https://doi.org/10.1080/14786430902832773.

[239] I. Aslam, M.I. Baskes, D.E. Dickel, S. Adibi, B. Li, H. Rhee, M. Asle Zaeem, M.F. Horstemeyer, Thermodynamic and kinetic behavior of low-alloy steels: An atomic level study using an Fe-Mn-Si-C modified embedded atom method (MEAM) potential, Materialia. 8 (2019) 100473. https://doi.org/10.1016/j.mtla.2019.100473.

[240] G.J. Ackland, M.I. Mendelev, D.J. Srolovitz, S. Han, A. V. Barashev, Development of an

interatomic potential for phosphorus impurities in α-iron, J. Phys. Condens. Matter. 16 (2004) S2629. https://doi.org/10.1088/0953-8984/16/27/003.

[241] H.K. Kim, W.S. Jung, B.J. Lee, Modified embedded-atom method interatomic potentials for the Fe-Ti-C and Fe-Ti-N ternary systems, Acta Mater. 57 (2009) 3140–3147. https://doi.org/10.1016/j.actamat.2009.03.019.

[242] M.I. Mendelev, S. Han, W.J. Son, G.J. Ackland, D.J. Srolovitz, Simulation of the interaction between Fe impurities and point defects in V, Phys. Rev. B - Condens. Matter Mater. Phys. 76 (2007) 214105. https://doi.org/10.1103/PhysRevB.76.214105.

[243] D.E. Smirnova, S. V. Starikov, An interatomic potential for simulation of Zr-Nb system, Comput. Mater. Sci. 129 (2017) 259–272. https://doi.org/10.1016/j.commatsci.2016.12.016.

[244] G. Bonny, D. Terentyev, R.C. Pasianot, S. Poncé, A. Bakaev, Interatomic potential to study plasticity in stainless steels: The FeNiCr model alloy, Model. Simul. Mater. Sci. Eng. 19 (2011) 085008. https://doi.org/10.1088/0965-0393/19/8/085008.

[245] G. Bonny, N. Castin, D. Terentyev, Interatomic potential for studying ageing under irradiation in stainless steels: The FeNiCr model alloy, Model. Simul. Mater. Sci. Eng. 21 (2013) 085004. https://doi.org/10.1088/0965-0393/21/8/085004.

[246] L.K. Béland, A. Tamm, S. Mu, G.D.D. Samolyuk, Y.N.N. Osetsky, A. Aabloo, M. Klintenberg, A. Caro, R.E.E. Stoller, Accurate classical short-range forces for the study of collision cascades in Fe–Ni–Cr, Comput. Phys. Commun. 219 (2017) 11–19. https://doi.org/10.1016/j.cpc.2017.05.001.

[247] M.I. Mendelev, M.J. Kramer, S.G. Hao, K.M. Ho, C.Z. Wang, Development of interatomic potentials appropriate for simulation of liquid and glass properties of nizr2 alloy, Philos. Mag. 92 (2012) 4454–4469. https://doi.org/10.1080/14786435.2012.712220.

[248] G. Bonny, A. Bakaev, D. Terentyev, Y.A. Mastrikov, Interatomic potential to study plastic deformation in tungsten-rhenium alloys, J. Appl. Phys. 121 (2017) 165107. https://doi.org/10.1063/1.4982361.

[249] W. Setyawan, N. Gao, R.J. Kurtz, A tungsten-rhenium interatomic potential for point defect studies, J. Appl. Phys. 123 (2018) 205102. https://doi.org/10.1063/1.5030113.